IN LIGHT AND DARK: LABORATORY AND ASTROPHYSICAL PROBES OF THE LATE UNIVERSE

Dissertation zur Erlangung des Doktorgrades
an der Fakultät für Mathematik, Informatik und Naturwissenschaften
der Universität Hamburg

vorgelegt von
Oindrila Ghosh

Hamburg, 2022

Gutachter der Dissertation:
Prof. Dr. Günter Sigl
Prof. Dr. Dieter Horns
Gutachter der Disputation:
Prof. Dr. Günter Sigl
Prof. Dr. Dieter Horns
Prof. Dr. Caren Hagner
Prof. Dr. Gudrid Moortgat-Pick
Dr. Kai Schmidt-Hoberg
Datum der Disputation: 15.12.2022
Vorsitzender der Prüfungsausschusses:
Prof. Dr. Caren Hagner
Vorsitzender der Promotionsausschusses:
Prof. Dr. Wolfgang J. Parak
Leiter des Fachbereich PHYSIK:
Prof. Dr. Günter Sigl
Dekan der Fakultät für Mathematik,
Informatik und Naturwissenschaften:
Prof. Dr.-Ing. Norbert Ritter

EIDESSTATTLICHE VERSICHERUNG
DECLARATION OF OATH

Hiermit erklaere ich an Eides statt, dass ich die vorliegende Dissertationsschrift selbst verfasst und keine anderen als die angegebenen Quellen und Hilfsmittel benutzt habe.

I hereby declare upon oath that I have written the present dissertation independently and have not used further resources and aids than those stated.

Hamburg
November 1, 2022

Oindrila Ghosh

ABSTRACT

In this thesis, I explore two broad interconnected themes. First, I seek a solution to the so-called GeV-TeV tension in the gamma-ray sky, through tracing the generation and evolution of plasma instabilities and energetic broadening in pair beams from TeV blazars, both in a proposed laboratory setup and then for astrophysical pair beams. Next, I chart the consequences of the energy losses from blazar beams in the thermal history of the universe at late times, subsequently its impact on structure formation, and what one can infer about dark matter halos in the subgalactic scale, in particular for light dark matter candidates such as axions. I then proceed to describe an axion haloscope based on the concept of detecting an amplified magnetic field generated by axion-induced current when embedded in the galactic dark matter halo.

ZUSAMMENFASSUNG

In dieser Arbeit untersuche ich zwei weitreichende, miteinander verbundene Themen. Zunächst suche ich nach einer Lösung für die sogenannte GeV-TeV-Spannung am Gammastrahlenhimmel, indem ich die Entstehung und Entwicklung von Plasmainstabilitäten und energetischer Verbreiterung in Paarstrahlen von TeV-Blazaren verfolge, sowohl in einem vorgeschlagenen Laboraufbau als auch für astrophysikalische Paarstrahlen. Als Nächstes gehe ich auf die Folgen der Energieverluste von Blazar-Strahlen in der thermischen Geschichte des Universums zu späten Zeiten ein, anschließend auf ihre Auswirkungen auf die Strukturbildung und darauf, was wir über Halos aus dunkler Materie im subgalaktischen Bereich ableiten können, insbesondere für leichte Kandidaten für dunkle Materie wie Axionen. Anschließend beschreibe ich ein Axion-Haloskop, das auf dem Konzept des Nachweises eines verstärkten Magnetfeldes basiert, das durch Axion-induzierten Strom erzeugt wird, wenn er in den galaktischen Halo aus dunkler Materie eingebettet ist.

FOREWORD

This thesis, titled, "In Light and Dark: Laboratory and Astrophysical Probes of the Late Universe", subtitled "From TeV Blazars to Table-top Experiments", is divided into Part I, Plasma Astrophysics: Fate of Relativistic Pair Beams in the Laboratory and Cosmos, and Part II, The Dark Universe: Dark Halos in a Blazar-heated Universe and Laboratory Probes of Dark Matter.

In Part I, I outline the observational discrepancy in the gamma ray spectra from TeV blazars and formulate the fate of the astrophysical neutral pair beams launched from the host active galactic nuclei (AGNs) of these blazars. In Chapter 1, I outline the conundrum in the GeV gamma-ray spectra of these objects, the role of cosmic magnetic field, and how plasma astrophysics comes to play an important role in explaining the discrepancy. In Chapter 2, I introduce how the growth rates for electrostatic instabilities scale with various parameters related to the beam and the environment, and show the computed growth rates for a number of distribution functions, applicable to laboratory and astrophysical plasmas. In Chapter 3, I explore the setting of a laboratory astrophysics experiment and show the relevant growth rates for a 2D Gaussian distribution as injected neutral pair beam and introduce the Fokker-Planck equation for pair beam evolution, which contains in a compact form the energy loss via instabilities that leads to the heating of the intergalactic medium and momentum diffusion leading to self-heating and relaxation of the beam, and compare the results with state-of-the-art particle-in-cell simulations. In Chapter 4, I discuss the fate of astrophysical beams, in terms of the modification of the resulting GeV secondary cascade spectra, for instability-induced energy loss and momentum broadening of the pair beam.

In Part II, I delve into how to harness the power of electromagnetic phenomena into exploring the dark component of our universe, starting from TeV blazar beams to uncover the size of the underlying dark structures, to tabletop experiment that can detect a current induced by the galactic dark matter. I introduce axions and axion-like-particles as dark matter in Chapter 5. Then in Chapter 6, I present the impact of heating of the intergalactic medium with the energy dumped into it from the blazar beams in terms of a modified temperature-density relation and elevated entropy floor. In Chapter 7, I show how the elevated entropy floor increases the Jeans and filtering mass of halos thus suppressing structure at small scales, and compare it directly with the predictions of ultralight axions, also known as wave dark matter. In Chapter 8, I return to a laboratory search for axion-like particles in our galaxy using an LC-circuit-based haloscope, WISPLC, with projected sensitivities for light axions.

Chapter 3 is a summary of the article titled, "Evolution of Relativistic Pair Beams: Implications for Laboratory and TeV Astrophysics". The list of authors with contributions is appended below.

- Oindrila Ghosh. *Contribution:* Analytical and numerical calculation of growth rate & Fokker-Planck equation.
- Marvin Beck. *Contribution:* PIC simulation and analysis of results.
- Ryan David Stark. *Contribution:* Experimental consultant on simulation.
- Benno Zeitler. *Contribution:* Experimental consultant on design and setup.
- Carl B. Scroeder. *Contribution:* Useful discussions and consultation on laboratory plasmas.
- Florian Gruener. Supervisor.
- Martin Pohl. *Contribution:* Advisor and consultant.
- Guenter Sigl. *Contribution:* Supervisor

Chapter 8 is a summary of the article titled, "WISPLC: Search for Dark Matter with an LC-Circuit" [1], published in *Physical Review D*. The list of authors and their corresponding contributions are appended below.

- Oindrila Ghosh. *Contribution:* Theoretical framework and sensitivity calculation.
- Zhongyue Zhang. *Contribution:* Experimental design, conceptualization, simulation and preliminary studies on detector sensitivity.
- Dieter Horns. *Contribution:* Supervisor.

To *Phela, Molina, and Lolita,*

My grandmothers, who due to child marriage, did not have the opportunity to complete school education

ACKNOWLEDGMENTS

First of all, I would like to thank my supervisors, Prof. Dr. Günter Sigl and Prof. Dr. Dieter Horns, without whose guidance this thesis would not be possible. I thank the Deutsche Forschungsgemeinschaft (DFG) for support through Germany's excellence strategy, Quantum Universe (EXC 2121 – 390833306) and University of Hamburg for supporting my position as a doctoral research associate in Hamburg, Quantum Universe Research School (QURS) for various academic and technical courses and workshops during my PhD, dynaMENT for their comprehensive mentoring programme, and Deutscher Akademischer Austauschdienst (DAAD) and DFG for their support through the Research Internships in Science and Engineering (RISE) Programme which allowed me to host Carol Ballinger from the University of St. Andrews in 2021 and Sankalan Bhattacharyya from the University of Cambridge in 2022, at the II. Institute for Theoretical Physics for their summer internships. A very special thanks goes to Elizabeth Duarte for being there for helping me sail smooth while navigating bureaucracy. I also thank Martin Stieben and the PHYSNET team for their prompt IT support, and the DESY International Office for making my PhD journey smoother with their consistent help with housing and immigration in Hamburg.

Through the ups and downs of my PhD, I was fortunate to have the incessant camaradarie of Simone Rossoni, for never letting me have a dull moment in the office, Julien Manshanden for being the senior PhD that welcomed me to the group and always went out of his way to help out even when busy, Dennis Maseizik for enthusiastically ensuring both our spines and computer accounts are doing fine, and Marvin Beck for valuable scientific discussions on laboratory plasmas. I thank Zhongyue (Delia) Zhang for a very exciting and lively collaboration on the up-and-coming axion detector WISPLC.

Living in Northern oceanic climate for the first time was particularly challenging, and I cannot overstate the positive impact cholecalciferol has had in my adaptation. I thank the Tennis Hockey and Cricket Club of Hamburg for providing the space and equipment to play cricket which has brought me a lot of joy outside of work with strong bonds and teamwork. In particular my sincere gratitude goes to both the women's cricket team for letting me be a part of the team and represent it in matches and tournaments, and the Rot-Gelb men's cricket teams for instructive, goal-oriented, and fun training sessions. I thank Quantum Universe and PIER for the support on science communication, and Philine van Vliet for making the STEMme Podcast a reality together. I thank Gisa Günther for her intensive German lessons which made my time in Hamburg certainly more enjoyable.

My heartfelt gratitude to Sangita Mazumdar, Alex Vasiliu, Nita Ghosh, Gayatri Batra, and Pragya Chopra, for their reassuring affection and companionship even during the darkest of times, in particular, the pandemic, which loomed large for the majority of my PhD work. I also thank Ivan Tulli, Aida Saghatchi, Josep Maria Batllori Berenguer, Alexander (Sasha) Zaytsev, and Trishita Banerjee for their warmth and friendships, and Marianne Geertz and Alexander Chatrchyan for being the perfect neighbors one could ask for.

I am grateful to have had my beloved, Isak Stomberg, by my side through these three years, who in addition to his support, encouragement, and love, brought me closer to nature and music, and stoked my interests in adjacent scientific areas with prolific discussions and musings.

CONTENTS

LIST OF FIGURES

LIST OF TABLES

Part I

PLASMA ASTROPHYSICS: FATE OF RELATIVISTIC PAIR BEAMS IN THE LABORATORY AND COSMOS

This part involves plasma astrophysics. I introduce the motivations to seek the physics of TeV blazars in a laboratory astrophysics setup, introduce basics of plasma instabilities and then discuss the evolution of a neutral pair beam in two distinct contexts, in the laboratory and for energetic astrophysical pair beams from blazars.

1 BACKGROUND AND MOTIVATION

1.1 MOTIVATION

Among TeV sources detected with the current-generation telescopes searching the gamma-ray sky, blazars are ubiquitous. Blazars are active galactic nuclei with jets erupting from them pointing their emission towards our line of sight (LoS). In this thesis, we will primarily focus on BL Lac type blazar sources. TeV photons from blazars interact with the extragalactic background light (EBL) and produce energetic electron-positron pairs, which in turn, undergo inverse Compton scattering (ICS) upon meeting the cosmic microwave background (CMB) and produce gamma-ray emission [5–7]. Thus, in addition to the TeV emission, their reprocessed GeV emission acts as a messenger of the astrophysics of TeV blazars, which can also be used as a powerful tool to constrain the properties of the EBL.

The primary mechanism for the loss of energy of the e^+e^- pairs is thought to be ICS off the CMB. However, this scenario is problematic for two reasons. The estimated electromagnetic cascade is not found in the gamma-ray observations [2]. In addition, when ICS is the only agent of reprocessing of the emissions from the TeV band [8], it overproduces the observed extragalactic gamma-ray background (EGRB) [9] in case of a decoupling between the parent galaxy and the TeV blazars hosted in them in terms of their cosmological evolution. More recent observations weakens the strong blazar evolution scenario, thus a different means by which the cascade flux is reduced, such as magnetic deflection of the charged pairs, is sought.

In presence of cosmic magnetic field, the pairs, in addition to the ICS cooling, will undergo gyration and can be deflected, forming the so-called "pair halos". This can lead to a serious suppression of the reprocessed GeV emission along the LoS [10]. Therefore, the strength of the extragalactic magnetic field (EGMF) associated with certain correlation lengths which determine the length scale to which the field is coherent, can also be inferred from the emission and constrained using gamma-ray observation of TeV blazars [11, 12]. A schematic is shown to depict the various processes the relativistic pairs can undergo.

In gamma-ray observations of TeV blazars, a strong suppression of the cascade emission is apparent, regardless of the fact that the energy spectra of the attenuated GeV emission should closely follow that of the expected primary TeV emission of a typical power-law cutoff:

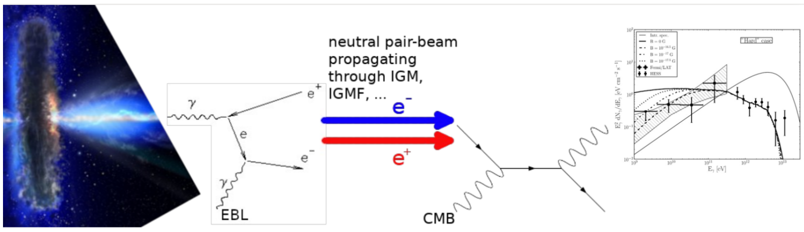

Figure 1: Schematic of the propagation of the neutral pair beam from a TeV blazar (Courtesy: Quantum Universe Day Slides, Marvin Beck)

$$dN_\gamma/dE \sim E^{-\Gamma} \exp\left(-E/E_{cut}\right), \tag{1}$$

where we note that the luminosity of the GeV cascade should be the same as the integral primary source luminosity across the multi-TeV energy bins, since nearly all of the power emitted in gamma rays above the TeV scale is absorbed. However, the prominent suppression indicates that the ICS is not as efficient as previously assumed and other mechanisms must be at play. At first glance, we revisit the scenario of magnetic pair deflection. For the deflection of the energetic pairs owing to the EGMF, the corresponding deflection angle is dependent on the correlation length of the magnetic field.

1.1.1 *Coherent magnetic field*

The impact of extragalactic magnetic field in then propagation of cosmic rays can be observed through their deflection off the cosmic magnetic field in voids, which the non-observation of GeV emission from TeV blazars can be attributed to [2]. Such deflection angle for cosmic rays with energy U_{CR} owing to the cosmic magnetic field when $r \leqslant l_c$ is estimated as

$$\Theta = -\frac{Ze}{U_{CR}}\mathbf{r} \times \mathbf{B} \tag{2}$$

with Z being the atomic number. For $r \gg l_c$ the deflection angle can be calculated as

$$\Theta_{rms} \simeq \frac{2}{\pi}\frac{ZeB}{U_{CR}}\left(rl_c\right)^{1/2} \tag{3}$$

where r is the source distance and l_c is the coherence length of the magnetic field [13].

1.1.2 *Turbulent magnetic field*

The calculation can then be further extended to turbulent magnetic fields using appropriate choice of the magnetic field power spectrum.

Since charged particles in turbulent magnetic fields perform a random walk, and $\overline{B} = 0$, it makes sense to consider the the rms strength of the stochastic magnetic field B_{rms} consistent within a certain correlation length λ_B such that

$$B_{rms}^2 = \int_0^\infty dk \mathbf{B}^2(k) \tag{4}$$

which is best described by a power spectrum of the form $B(k) \propto k^{-n}$, where n is the Kolmogorov exponent, $n = 5/3$. The minimum and maximum correlation lengths are defined as L_{min} and L_{max} respectively, and λ_B can then be expressed as:

$$\lambda_B = \frac{1}{2} L_{max} \cdot \frac{n-1}{n} \cdot \frac{1 - \left(\frac{L_{min}}{L_{max}}\right)^n}{1 - \left(\frac{L_{min}}{L_{max}}\right)^{n-1}} \tag{5}$$

The non-observation of pair halos and suppression of cascade emission can be used as an effective tool to constrain the EGMF. The first of such constraints using observational data from gamma-ray telescopes Fermi and HESS were presented in [2] as follows. In Fig. 2 the primary emission from TeV blazars shown in thin dashed curves can be compared with the cascade emission producing electron-positron pairs shown in the dotted curve. The thicker curves represent various models and the lower limit on cascade emission energies are shown in vertical lines. The data points from Fermi and HESS for three distinct TeV blazars go on to show a clear suppression at GeV energies.

The most recent constraint on the EGMF comes from the Fermi-LAT data for a number of TeV blazars [3]. This is shown in Fig. 3.

Nevertheless, magnetic deflection does not solve the problem of overproducing the EGRB. This is because the average number of pairs that are deflected out of the LoS are compensated by the average number of pairs that are deflected into it, thus keeping the contribution to EGRB unaffected by pair deflection. An effective mechanism to reconcile this problem would be to turn towards plasma physics. Blazar beams can undergo energy loss via instabilities arising from the relativistic beam pairs interacting with the background plasma of the intergalactic medium (IGM). The beam-plasma instability, also known as the pair instability [14], competes with ICS and heats the IGM. This has profound implications in the thermal history [15] at late times and thus, structure formation in the Universe. The instability-induced energy loss can be considered as a viable alternative to the magnetic deflection scenario. In the scenario driven by collective plasma effects, energy is deposited from the beam into the IGM, instead of producing reprocessed GeV spectra only via ICS [9].

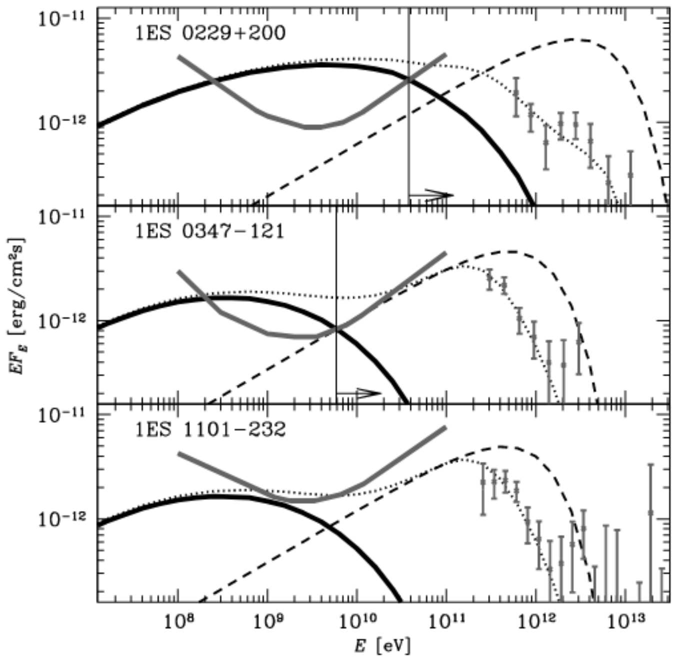

Figure 2: Comparison of cascade emission between models and observations [2]

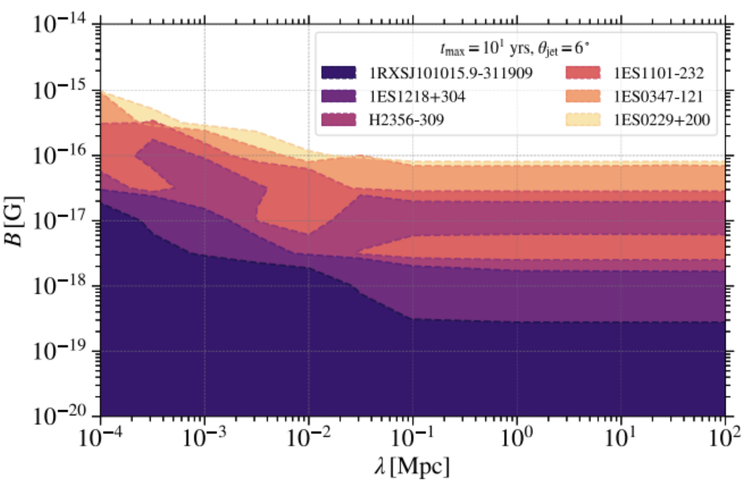

Figure 3: Exclusion curves from various sources as observed with Fermi-LAT for 10 years [3]

1.2 COLLECTIVE PLASMA EFFECTS

Plasmas are considered to be quasineutral mixtures of positively charged ions and negatively charged electrons, having bulk properties that can be expressed in terms of number densities, thermal velocities, pressures, temperatures etc. as they constitute a very large number of particles. Due to Debye screening of small electric fields of a given charge by other charged particles in the plasma of species s to a distance characterised by Debye length

$$\lambda_{D_s} = \left(\frac{\epsilon_0 k_B T_s}{n_e e^2}\right)^{1/2}, \tag{6}$$

the motion of individual particles, which is otherwise strongly affected by other particles, can be understood in terms of single particle orbits governed by Lorentz force, when the plasma is collisionless. Here, n_e represents the number density of electrons in the plasma, e is the electronic charge, T_s is the temperature of the species, and ϵ_0 and k_B are vacuum permittivity and Boltzmann's constant.

However, the overall plasma dynamics is much more complicated thanks to the interactions between the particles and fields. From the perspective of kinetic theory, we can contextualize the probability of finding a certain number of particles in a given phase space interval

$$[\mathbf{x}, \mathbf{v}; \mathbf{x} + d\mathbf{x}, \mathbf{v} + d\mathbf{v}],$$

in terms of a momentum distribution function

$$F_s(\mathbf{x}, \mathbf{v}, t)$$

where $\mathbf{x}$ and $\mathbf{v}$ denote position and velocity (momentum) coordinates.

In general, homogeneous Maxwell's equations with electric field $\mathbf{E}$, and magnetic field $\mathbf{B}$

$$\nabla \cdot \mathbf{E} = \rho/\epsilon_0 \tag{7}$$

$$\nabla \cdot \mathbf{B} = 0 \tag{8}$$

$$\nabla \times \mathbf{E} = -\frac{\partial \mathbf{B}}{\partial t} \tag{9}$$

$$\nabla \times \mathbf{B} = \mu_0 \mathbf{j} + \frac{1}{c^2}\frac{\partial \mathbf{E}}{\partial t} \tag{10}$$

and the following definitions of charge and current densities, with q_s, n_s, and $\mathbf{v}_s$ being charge, number density, and velocity of a given species s,

$$\rho = \sum_s q_s n_s \tag{11}$$

$$\mathbf{j} = \sum_s q_s n_s \mathbf{v}_s \tag{12}$$

can be used in order to construct the Vlasov equation [16],

$$\left[\frac{\partial}{\partial t} + \mathbf{v} \cdot \nabla + \frac{q_s}{m_s}(\mathbf{E} + \mathbf{v} \times \mathbf{B}) \cdot \frac{\partial}{\partial \mathbf{v}}\right] F_s(\mathbf{x}, \mathbf{v}, t) = 0 \tag{13}$$

which delineates the plasma dynamics for each species s, such that the bulk densities and velocities in Eqs. 11 and 12 are moments of the distribution function corresponding to the given species s, $f_s(\mathbf{x}, and\mathbf{v}, t)$ is the solution of Eq. 13. The plasma frequency is expressed as:

$$\omega_p = \sqrt{\frac{4\pi n_e e^2}{m_e}}, \tag{14}$$

where m_e is the electronic mass.

1.3 ELECTROSTATIC MODES OF INSTABILITIES

The energy loss mechanism associated with the fastest growing modes competes with the inverse Compton cooling, injecting energy into the intergalactic medium, also known as the blazar-heating mechanism. The most discussed simplified case of such instabilities is the two-stream instability, a more general version of which is when the interaction between the beam and the plasma occurs at an angle, rather than head-on. This is also known as the oblique mode of Langmuir oscillations in the density of the plasma [17]. The instabilities that arise can be electrostatic or electromagnetic in nature, and the associated Langmuir waves satisfy the resonance condition:

$$\omega - \mathbf{k} \cdot \mathbf{v} = 0 \tag{15}$$

where $\omega = \omega(\mathbf{k})$ is the complex frequency.

1.3.1 *Solving the Vlasov equation*

For an arbitrary homogeneous and infinite beam plasma system consisting N species of charge q_s, mass m_s, density n_s, and mean velocity $\mathbf{v}_j$, which is charge and current neutral, i.e., $\sum_s q_s n_s = 0$ and $\Sigma_j q_s n_s \mathbf{v}_j = 0$ and the equilibrium electromagnetic fields are set to zero, adopting a distribution function $F_s(\mathbf{r}, \mathbf{p}, t)$, the relativistic Vlasov equation reads in terms of a normalised distribution function $F_s(\mathbf{r}, \mathbf{p}, t) = f_s(\mathbf{p}, t)/n_p$ where n_p is the number density of particles,

$$\frac{\partial f_s}{\partial t} + \mathbf{v} \cdot \frac{\partial f_s}{\partial \mathbf{r}} + q_s \left(\mathbf{E} + \frac{\mathbf{v} \times \mathbf{B}}{c} \right) \frac{\partial f_s}{\partial \mathbf{p}} = 0 \tag{16}$$

where each species j is described by its initial distribution function $f_s^0(p)$ with $\int d\mathbf{p} f_s^0(p) = 1$. The charge $\rho = \sum_s n_s q_s \iiint d\mathbf{p} f_s$ and and current densities $\mathbf{J} = \sum_s n_s q_s \iiint d\mathbf{p}\mathbf{v} f_s$ follow Maxwell's equation.

The linearization scheme allows us to vary every relevant variable as

$$\xi = \xi_0 + \xi_1 \exp(\imath \mathbf{k} \cdot \mathbf{r} - \imath \omega t), \quad |\xi_1| \ll |\xi_0| \tag{17}$$

where ξ_0 represents the equilibrium initial value. Writing out Maxwell's equations and eliminating magnetic field $\mathbf{B}$, one obtains the tensorial form of the general dispersion relation

$$\det \mathbf{T} = 0 \tag{18}$$

where

$$\mathbf{T} = \frac{\omega^2}{c^2} \epsilon(\mathbf{k}, \omega) + \mathbf{k} \otimes \mathbf{k} - k^2 \mathbf{I} \tag{19}$$

with tensor product $\mathbf{k} \otimes \mathbf{k} = k_\alpha k_\beta$ where α and β are dummy indices, I is the identity matrix, and the dielectric tensor is defined as:

$$\begin{aligned} \epsilon_{\alpha\beta}(\mathbf{k}, \omega) =& \delta_{\alpha\beta} + \sum_s \frac{\omega_{p,s}^2}{\omega^2} \iiint d\mathbf{p} \frac{p_\alpha}{\gamma(\mathbf{p})} \frac{\partial f_s^0}{\partial p_\beta} \\ &+ \sum_s \frac{\omega_{p,s}^2}{\omega^2} \iiint d\mathbf{p} \frac{p_\alpha p_\beta}{\gamma(\mathbf{p})^2} \frac{\mathbf{k} \cdot \left(\frac{\partial f_s^0}{\partial \mathbf{p}} \right)}{m_s \omega - \mathbf{k} \cdot \mathbf{p}/\gamma(\mathbf{p})} \end{aligned} \tag{20}$$

where

$$\gamma(\mathbf{p}) = \sqrt{1 + \frac{|\,\mathbf{p}\,|^2}{m_s^2 c^2}} \tag{21}$$

1.3.2 *Dispersion relation*

Applying axisymmetry as $\mathbf{k} = (k_x, 0, k_z)$, the dispersion relation can be cast in terms of the simplified dielectric function for the electrostatic case ($\mathbf{B} = 0$) as follows:

$$\epsilon = 1 + \sum_{\bar{s}} \frac{m_e \omega_{p,s}^2}{k^2} \int \frac{\mathbf{k} \cdot \boldsymbol{\nabla}_p f_s}{\omega - \mathbf{k} \cdot \mathbf{v}} d\mathbf{p} = 0. \tag{22}$$

where number density $n_s \equiv \int F_s^0 d\mathbf{p}$ is the number density, and normalized distribution function $f_s \equiv F_s^0 / n_s$ are represented for each species s. Performing integration by parts,

$$\begin{aligned} \epsilon =& 1 - \sum_{s} \frac{m_e \omega_{p,s}^2}{k^2} \int f_s \mathbf{k} \cdot \boldsymbol{\nabla}_p \frac{1}{\omega - \mathbf{k} \cdot \mathbf{v}} d\mathbf{p} \\ =& 1 - \sum_{s} \frac{\omega_{p,s}^2}{k^2 c^2} \int f_s \frac{k^2 c^2 - (\mathbf{k} \cdot \mathbf{v})^2}{\gamma (\omega - \mathbf{k} \cdot \mathbf{v})^2} d\mathbf{p} = 0 \end{aligned} \tag{23}$$

with $\omega_{p,s} = \left(4\pi n_s e^2 / m_e\right)^{1/2}$ being the plasma frequency for species s, which can be designated as beam, background plasma electrons, or ions.

1.3.3 *Phase-space distribution functions*

The general form of the normalized phase-space distribution function can then be expressed in Cartesian coordinates as

$$f(\mathbf{p}) = f(p_x) f(p_y) f(p_z) \tag{24}$$

where

$$\int_{-\infty}^{+\infty} f(\mathbf{p}) d\mathbf{p} = \int f(p_x) dp_x \int_{-\infty}^{+\infty} f(p_y) dp_y \int_{-\infty}^{+\infty} f(p_z) dp_z = 1 \tag{25}$$

and

$$\mathbf{k} = (k_x, k_y, k_z) \tag{26}$$

At this point, we ignore any cross-terms that may be related to beam emittance and express the beam distribution function in terms of separable components in each direction.

It can be shown that axisymmetry may be assumed without any loss of generality. Thus the wave number tensor can now be represented in terms of a component parallel to the direction of propagation of the beam, $k_{||} = k_z$, and a component perpendicular to it, $k_{\perp} = \sqrt{k_x^2 + k_y^2}$.

Eq. 24 can then be cast as

$$\int_{-\infty}^{+\infty} f(\mathbf{p})d\mathbf{p} = \int_{0}^{+\infty} f(p_\perp)p_\perp dp_\perp \int_{0}^{2\pi} d\theta \int_{-\infty}^{+\infty} f(p_{||})dp_{||} = 1 \quad (27)$$

1.3.4 *Reactive and kinetic regime*

When the injected beam does not have a wide variation in momentum, the dispersion relation reduces to its hydrodynamic form, which can also be derived from the continuity and momentum equations as,

$$1 - \frac{\omega_{p,p}^2}{\omega^2} - \frac{\omega_{p,b}^2}{\gamma^3\left(\omega - k_{||}v_b\right)^2}\frac{\gamma^2 k_\perp^2 + k_{||}^2}{k_\perp^2 + k_{||}^2} = 0 \quad (28)$$

where subscript p stands for the background plasma, and b represents the beam. This is also known as the reactive regime, characterised by the condition

$$| \mathbf{k} \cdot \Delta\mathbf{v} | \ll \Gamma_r \quad (29)$$

i.e., when the velocity/momentum spread of the beam $\Delta\mathbf{v}$ is negligibly small, the growth rate of instabilities is very high. Here, Γ_r is the growth rate in the reactive case. When this condition is not fulfilled, i.e., in the more realistic scenario of an astrophysical pair beam with finite momentum spread, the relativistic dispersion equation can be solved by expanding in the limit $\omega \to \omega_r$ with ω_r being the plasma frequency at resonance, and splitting the frequency into real and imaginary parts. The growth rate in the kinetic regime is then expressed as the imaginary part of the frequency $\omega = \Im\left(\omega_r + i\omega_i\right)$

$$\Gamma_k = \omega_i, \quad (30)$$

where

$$\omega_i = -\frac{\Im\Lambda\left(\omega = \omega_r\right)}{\frac{\partial\Re\Lambda\left(\omega=\omega_r\right)}{\partial\omega_r}} \quad (31)$$

with

$$\Re\Lambda\left(\omega = \omega_r\right) \approx 1 - \frac{\omega_p^2}{\omega_r^2} \quad (32)$$

and

$$\Im\Lambda\left(\omega=\omega_{r}\right)\approx-\sum_{b}\frac{4\pi^{2}n_{b}e_{b}^{2}}{k^{2}}\times\int k\frac{\partial F(\mathbf{p})}{\partial\mathbf{p}}\delta\left(\mathbf{kv}-\omega_{r}\right)d\mathbf{p}\tag{33}$$

Setting $\omega_r = \omega_p$, the expression for growth rate in the kinetic regime is

$$\Gamma_{k}=\omega_{i}=\omega_{p}\frac{2\pi^{2}n_{b}e^{2}}{k^{2}}\int\mathbf{k}\cdot\frac{\partial f(\mathbf{p})}{\partial\mathbf{p}}\delta\left(\omega_{p}-\mathbf{k}\cdot\mathbf{v}\right)d\mathbf{p}.\tag{34}$$

Eq. 34 embodies the dynamics of the entire $\mathbf{k}$-space. In the $k_{\perp} \rightarrow 0$ limit, the two-stream mode, historically also known as the beam-plasma or Buneman instability, is recovered; $k_{\parallel} \rightarrow 0$ characterizes the filamentation mode, and all intermediate modes are considered the most general case characterise by the oblique mode of instabilities and relevant in the discussion of electrostatic instabilities, and we will explore this in our work with a particular emphasis.

2 PLASMA INSTABILITIES

In this chapter, we explore then growth rates from the solutions to the dispersion relations for various beam plasma systems for a number of beam distribution functions and background plasma conditions.

2.1 PROPAGATION THROUGH COLD BACKGROUND PLASMA

Electrostatic modes of plasma instability saturate owing to Landau damping, that is when the beam electrons have a phase velocity that falls below the thermal speed of plasma electrons, they get absorbed by the plasma. For a relativistic electron-positron pair beam, with a number density of n_b with a Lorentz factor of γ propagating through a cold monoenergetic plasma with a number density n_p, the dispersion relation, Eq. 22 for surviving electrostatic mode is,

$$1 - \frac{\omega_p^2}{\omega^2} - \sum_b \frac{4\pi n_b e^2}{k^2} \int d\mathbf{p} \frac{\mathbf{k}\frac{\partial f_b(\mathbf{p})}{\partial \mathbf{p}}}{\mathbf{k}\cdot\mathbf{v} - \omega} = 0 \tag{35}$$

where the background plasma is modelled using a cold distribution function resolved in Cartesian momentum coordinates p_x, p_y, and p_z.

$$f_p(\mathbf{p}) = \delta(p_x)\,\delta(p_y)\,\delta(p_z - P_p) \tag{36}$$

with $P_p = m_e v_p$. The remaining notations carry the same meaning as denoted in Chapter 1.

2.1.1 *Cold relativistic beam*

For a cold relativistic beam described by the following distribution function in the case of a simplified case of a monoenergetic beam characterized by momentum P_b such that $P_b = m_e \gamma v_b$,

$$f_b(\mathbf{p}) = \delta(p_\perp)\,\delta\left(p_\parallel - P_b\right)/2\pi p_\perp, \tag{37}$$

he growth rate is well-known [17]:

$$\delta_r = \frac{\sqrt{3}}{2^{4/3}} \left(\frac{2\alpha}{\gamma}\right)^{1/3} \left(\frac{k_\parallel^2}{\gamma^2 k^2} + \frac{k_\perp^2}{k^2}\right)^{1/3}, \tag{38}$$

where α denotes the number density contrast between the beam and the background plasma $\alpha = n_b/n_p$, and the Lorentz factor of the beam $\gamma = \frac{1}{\sqrt{1-\beta_b^2}}$ such that $\beta_b = \frac{P_b}{m_e c}$.

2.1.2 *Beams with finite temperature*

Beam temperature, T_b, must be taken into account while discussing the more realistic scenarios beyond a monochromatic beam. For a warm beam with beam temperature T_b, the perpendicular momentum spread is

$$\Delta p_\perp = \sqrt{2m_e T_b}, \tag{39}$$

and momentum spread parallel to the propagation direction of the beam is

$$\Delta p_\parallel = \sqrt{2m_e T_b}\gamma. \tag{40}$$

An example of such a distribution function is the waterbag distribution, is a simplified distribution function for a warm beam described as

$$f_b(\mathbf{p}) = \frac{1}{4\Delta p_\parallel \Delta p_\perp} \left(\Theta\left[p_\perp - \Delta p_\perp\right]\right) \left(\Theta\left[p_\parallel - P_b - \Delta p_\parallel\right] - \Theta\left[p_\parallel - P_b + \Delta p_\parallel\right]\right) \tag{41}$$

with Θ denoting the Heaviside step function [18].

2.2 PROPAGATION THROUGH WARM PLASMA

For a relativistic beam propagating through hot plasma, we solve the dispersion relations for a) a cold beam, and b) a warm beam and examine their dependences on the Lorentz factor of the beam γ, as well as the density contrast α. An example of such a scenario is astrophysical pair beams propagating through the warm intergalactic medium. The distribution function describing the warm plasma can be written as a Maxwellian peaking about this temperature T_p.

$$f_p(p) = \left(\frac{1}{2\pi m_e k_B T_p}\right)^{3/2} \exp\left(-\frac{p^2}{2m_e k_B T_p}\right) \tag{42}$$

2.2.1 *Cold beam*

For a cold beam monochromatic with a beam momentum P_b, the normalized beam distribution function can be expressed as:

$$f_b(\mathbf{p}) = \frac{1}{2\pi p_\perp}\delta\left(p_\perp\right)\delta\left(p_\parallel - P_b\right), \tag{43}$$

such that $f_b(\mathbf{p}) = F_b(\mathbf{p}, \mathbf{x})/n_b$.

Inserting 42 and 43 into the general expression of the dispersion relation, where s denotes species of particles, e.g., beam or plasma,

$$\epsilon = 1 + \sum_s \frac{m_e \omega_{p,s}^2}{k^2} \int \frac{\mathbf{k} \cdot \boldsymbol{\nabla}_p F_s}{\omega - \mathbf{k} \cdot \mathbf{v}} d\mathbf{p} = 0, \tag{44}$$

one can obtain

$$1 - \frac{\omega_p^2}{\omega^2}\left(1 + 3k^2\lambda_D^2\right) + i\frac{\pi n_b}{n_p} m_e v_p^2 R = 0 \tag{45}$$

where

$$R \equiv \int \frac{k \partial f_b / \partial p_{\|}}{\omega - k_{\|} v_{b,\|}} d\mathbf{p} \tag{46}$$

which can be computed by evaluating individual residues corresponding to the poles contained in the integration, characterised by $v_z = v_p$. Splitting the frequency of the Langmuir oscillation into real and imaginary parts,

$$\omega = \omega_r + i\Gamma \tag{47}$$

where the growth rate corresponds to the imaginary part Γ, we obtain from Eq. 45 using the expression for the residue in Eq. 46,

$$\Gamma \approx \frac{\pi n_b}{2 n_p} m_e v_p^2 R \tag{48}$$

The two elements contributing to the pole are:

$$\frac{\partial}{\partial p_{\|}} \left(\omega - k v_{b,\|}\right)\bigg|_{\text{pole}} = -\frac{k c^2}{\gamma_b^3 m_e} \tag{49}$$

and

$$k \frac{\partial f_b}{\partial p_{\|}}\bigg|_{\text{pole}} = k \frac{\delta(p_{\perp})}{2\pi} \frac{\partial}{\partial p_{\|}} \delta(p_{\|} - P_b) \tag{50}$$

Noting that $d^3 p = 2\pi p_{\|} dp_{\|} dp_{\perp}$, the instability growth rate for a cold relativistic beam passing through a hot nonrelativistic Maxwellian plasma can be expressed as [14]:

$$\Gamma = \frac{\pi \alpha \omega_p}{2c^2} m_e^2 v_p^2 \gamma_b^3. \tag{51}$$

$\alpha = n_b/n_p$ being the density contrast between the beam and the plasma.

2.2.2 *Warm beam*

The most realistic approximation for a warm relativistic beam is described by a shifted Maxwell-Jüttner distribution function [19]

$$f_b(\mathbf{p}) = \frac{m_e c^2}{4\pi\gamma k_B T_b K_2\left(m_e c^2/k_B T_b\right) m_e^3 c^3} \exp\left(-\frac{\gamma\left(E - v_{b,\|}p_\| - v_{b,\perp}p_\perp\right)}{k_B T_b}\right) \tag{52}$$

where T_b is the beam temperature and K_2 represents modified Bessel function of the second kind. Performing similar calculations as above, one obtains for instability growth rate in propagation through a warm Maxwellian plasma [19]:

$$\Gamma \approx -\Gamma_0 \frac{\pi\gamma_w^2\gamma_b^3\left(v_b - v_{b,\|}\right)}{4\gamma\mu^2 K_2(\mu)\mathcal{G}^3 c}\left[\left(\mathcal{G}^2\mu^2 + 2\mathcal{G}\mu + 2\right) + \frac{\gamma^2 v_{b,\perp}^2}{2\mathcal{G}^2 c^2}\left(2\mathcal{G}\mu + 2\right)\right]\exp\left(-\mathcal{G}\mu\right) \tag{53}$$

where the maximum growth rate

$$\Gamma_{max} \equiv \omega_p\gamma\left(n_b/n_p\right)\left(m_e v_b^2/k_B T_b\right) \tag{54}$$

and

$$\mathcal{G}' \equiv \gamma_b\left(1 - v_{b,\|}v_b/c^2\right)/\gamma_w \tag{55}$$

with

$$w = \gamma_b^{-1} v_{b,\perp'}/\left(1 - v_{b,\|'}v_b/c^2\right) \tag{56}$$

and

$$\gamma_w = \left(1 - w^2/c^2\right)^{-1/2} \tag{57}$$

The warm beam can also be described by a simplified waterbag distribution. In this case, the above calculation leads to a growth rate of

$$\Gamma = \frac{\pi\alpha\omega_p m_e v_p^2\gamma^3}{8\Delta p_\| c^2} \tag{58}$$

2.3 KINETIC GROWTH AND BEAM RELAXATION

As discussed in 1, the spread in velocity determines whether the instability proceeds in the reactive or kinetic regime. If the velocity spread of the beam pairs in the direction parallel and perpendicular to the direction of propagation is sufficiently large, as is the case for most realistic beams, in the laboratory as well as in astrophysical environments, the instability is kinetic. For relativistic beams $\gamma \gg 1$ with an angular spread $\Delta\theta \leqslant 1$, the growth rate can be described in spherical polar coordinates as [20] where θ represents the angle between the direction of beam propagation and the wave vector $\mathbf{k}$:

$$\Gamma_k = \operatorname{Im}\omega = \pi\omega_p \frac{n_b}{n_p}\left(\frac{\omega_p}{kc}\right)^3 \int_{\theta_1}^{\theta_2} \frac{d\theta}{\left[(\cos\theta_1 - \cos\theta)(\cos\theta - \cos\theta_2)\right]^{1/2}} \times \left[-2g\sin\theta + \left(\cos\theta - \frac{kc}{\omega_p}\cos\theta'\right)\frac{\partial g}{\partial\theta}\right]. \tag{59}$$

This is obtained by splitting the beam distribution function $f(p,\theta)$ into an angular part $g(\theta)$ and a momentum component such that [21]:

$$g = mc\int_0^\infty pf(p,\theta)dp, \tag{60}$$

and

$$\cos\theta_{1,2} = \frac{\omega_p}{kc}\left(\cos\theta' \pm \sin\theta'\sqrt{\frac{k^2c^2}{\omega_p^2} - 1}\right) \tag{61}$$

where θ is the angle between the direction of beam propagation and the wave vector.

Through instability growth, energy is lost from the pair beams into the background plasma. However, for the quasi-linear treatment of the beam evolution to be applicable, one presumes that the production of Langmuir oscillation associated with the beam instability is comparable to the drift of the pair beam speed within the plasma. The Langmuir waves can be damped or absorbed owing to various dissipative processes. Even for low to moderate levels of variation in density, the phase velocity of the waves can reduce to the level of the thermal velocity of electrons in the plasma, v_{th}. When this happens, the waves can undergo Landau damping, which is when the plasma electrons completely absorb the Langmuir excitation. The interaction between the excitation and e^+e^- pairs in the beam can cause diffusion of the pairs towards constant perpendicular momenta. The relevant equation governing the spectral energy density of the beam $W(k,\theta',z)$ can be expressed as

$$\frac{3kv_{th}^2}{w_p}\cos\theta'\frac{\partial W}{\partial z} = 2W\,\mathrm{Im}\,\omega = 2W\Gamma_k \tag{62}$$

where z is the coordinate in the parallel direction, and Γ_k designates the kinetic growth rate of the beam-plasma instabilities. The distribution function evolves in spherical coordinates $(p, \theta, \varphi;\ k, \theta'$ and $\varphi')$ along the direction of propagation z as [22]:

$$\begin{aligned}\cos\theta\frac{\partial f}{\partial z} =& \frac{1}{p^2}\frac{\partial}{\partial p}p^2\left(D_{pp}\frac{\partial f}{\partial p} + \frac{D_{p\theta}}{p}\frac{\partial f}{\partial \theta}\right)\\ &+ \frac{1}{p\sin\theta}\frac{\partial}{\partial\theta}\sin\theta\left(D_{p\theta}\frac{\partial f}{\partial p} + \frac{D_{\theta\theta}}{p}\frac{\partial f}{\partial\theta}\right),\end{aligned} \tag{63}$$

where the diffusion tensors can be written as

$$\begin{aligned}&\left.\begin{matrix} D_{pp} \\ D_{p\theta} \\ D_{\theta\theta}\end{matrix}\right\} = 2\pi\frac{m\omega_p^4}{n_p c^3}\int_{\frac{\omega_p}{c}}^{\infty}\frac{dk}{k}\\ &\times\int_{\theta_1'}^{\theta_2'}\frac{\sin\theta' W(k,\theta')\,d\theta'}{\sqrt{\left(\cos\theta_1' - \cos\theta'\right)\left(\cos\theta' - \cos\theta_2'\right)}}\left\{\begin{matrix} 1 \\ \zeta \\ \zeta^2, \end{matrix}\right\}\end{aligned} \tag{64}$$

where

$$\zeta = \left(\cos\theta - \frac{kc}{\omega_p}\sin\theta'\right)/\sin\theta, \tag{65}$$

and similarly as before,

$$\cos\theta_{1,2} = \frac{\omega_p}{kc}\left(\cos\theta \pm \sin\theta\sqrt{\frac{k^2c^2}{\omega_p^2} - 1}\right). \tag{66}$$

It can be understood as an effect of momentum broadening for the beam pairs, appearing as a self-heating of the beam, as a result of redistribution of energy in the phase space rather than energy draining out of the beam into the background plasma. More generally, the convective effect of energy loss and the diffusive process of momentum broadening can be framed in a Fokker-Planck type evolution. We delve deeper into this framework in the next chapter.

2.4 GROWING BEAM-PLASMA INSTABILITIES IN THE LABORATORY

2.4.1 *Experimental setup*

A laboratory experiment is designed where a high-power laser is converted into electron-positron pairs in a tungsten target. The outgoing jet is then run through a magnetised chamber to align the trajectories of the charged pairs in the forward direction. This way, a well-defined neutral "beam" is constructed. The beam then passes through a laboratory plasma. It is at this stage we expect to detect beam-plasma instability which is expected to mimic astrophysical pair beams undergoing plasma instabilities in the IGM. This setup is delineated in Fig. 4.

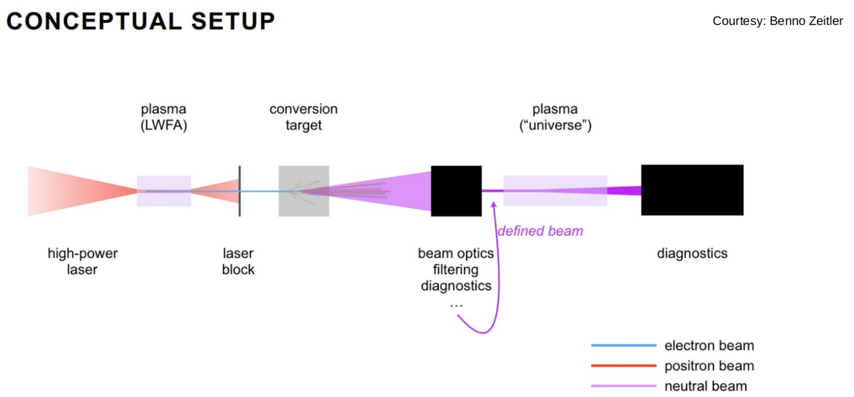

Figure 4: Experimental setup for laboratory astrophysics; Courtesy: Benno Zeitler

2.4.2 *Laboratory beam-plasma distributions*

When the injected pair beam is monochromatic, the growth rate is given by 38, using which the oblique growing modes are plotted in Figs. 5, 6, and 7, normalized with respect to the plasma frequency ω_p, as a function of $k_{||}$ and $k_\perp$ for beam Lorentz factors of 25, 50, and 100.

In a realistic laboratory setup, as shown in Fig. 4, the beam has a momentum spread, and the corresponding momentum distribution function can be expressed as:

$$f_{\text{lab}}(p_\perp, p_{||}) = \exp\left(\frac{\ln(c_1+1)}{\sqrt{(p_{||}-c_2)^2 + p_\perp^2 + 1}}\right)^{c_3} - 1 \tag{67}$$

where assuming axisymmetry, $p_\perp = \sqrt{p_x^2 + p_y^2}$ and $p_{||} = p_z$. The mean longitudinal momentum is dependent on the Lorentz factor of the beam γ, and m_e, representing the electron (positron) rest mass:

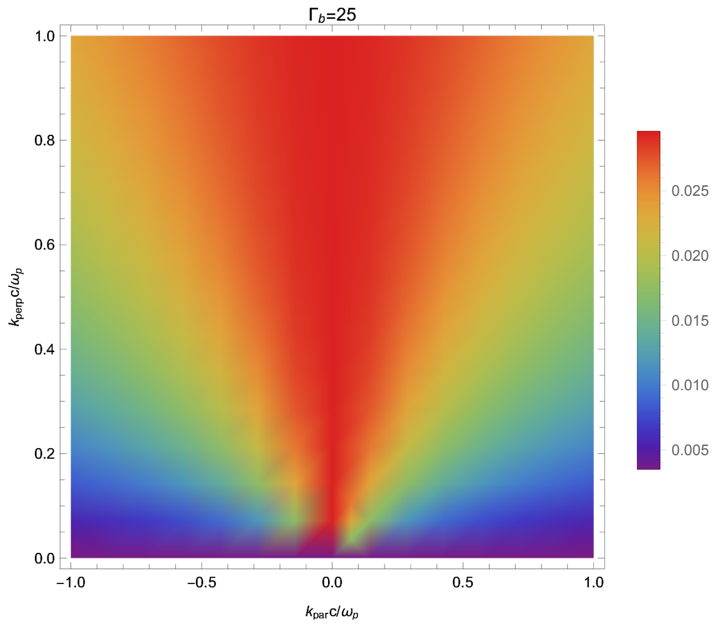

Figure 5: Reactive growth rates for a cold relativistic beam with $\gamma = 25$, and $\alpha = 10^{-3}$. Oblique growing modes are plotted, with growth rates normalized with respect to the plasma frequency ω_p, as a function of $k_{||}$ and $k_{\perp}$.

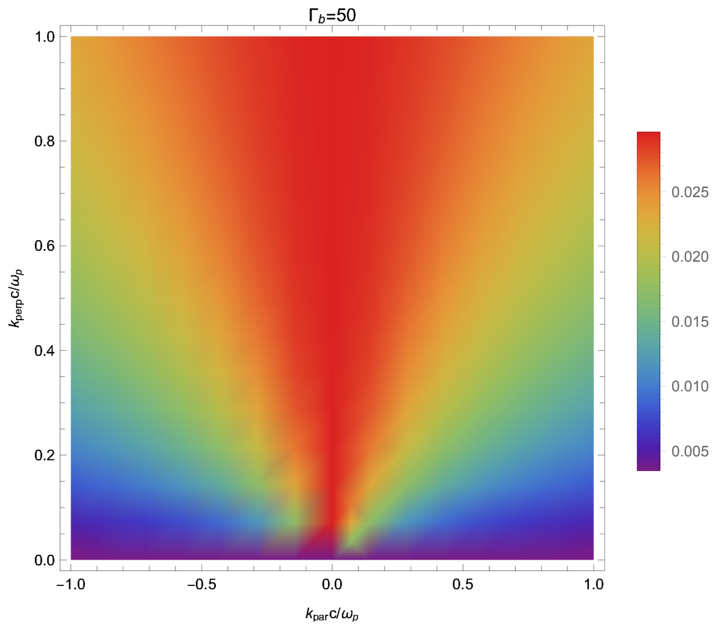

Figure 6: Reactive growth rates for a cold relativistic beam with $\gamma = 50$, and $\alpha = 10^{-3}$. Oblique growing modes are plotted, with growth rates normalized with respect to the plasma frequency ω_p, as a function of $k_{||}$ and $k_{\perp}$.

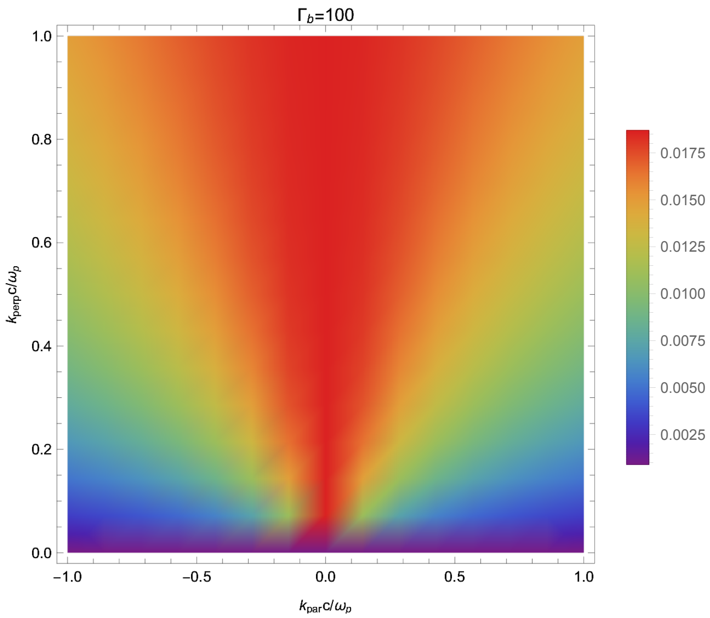

Figure 7: Reactive growth rates for a cold relativistic beam with $\gamma = 100$, and $\alpha = 10^{-3}$. Oblique growing modes are plotted, with growth rates normalized with respect to the plasma frequency ω_p, as a function of $k_{||}$ and $k_{\perp}$.

$$\mu = \sqrt{\gamma^2 - 1} m_e c \tag{68}$$

The growth rates of instabilities in the oblique mode for a beam distribution function as indicated in Eq. 67 with $c_1 = 0.11$ and $c_3 = 4$, are estimated using a numerical integration scheme of the kinetic growth rate a la Eq. 59 for a range of beam Lorentz factors which set c_2, as shown in Figs. 8, 9, 10, and 11 for a beam to background plasma density contrast of $\alpha = 10^{-4}$. The three fitting parameters are derived from a simulation of the laboratory astrophysics experiment using Geant4. Equation 67 is first coordinate-transformed into polar coordinates, and then the momentum integration is performed from $p = 0$ to $p \to \infty$. Let us make note of the poles in the denominator of Eq. 59. In order to avoid them, the angular integration is performed from θ_1 to $(\theta_1 + \theta_2)/2 - \epsilon$ and then from $(\theta_1 + \theta_2)/2 + \epsilon$ to θ_2. θ_1 to θ_2 is described in Eq. 66 where $\theta = \tan^{-1}(p_{||}/p_{\perp})$.

2.5 COMPARISON WITH ASTROPHYSICAL CASE

In this section, we compute the growth rate for a generic beam distribution function representing an astrophysical pair beam:

$$f_b(p, \theta) = \frac{1}{\pi \Delta\theta^2} \exp\left\{ -\left(\frac{\theta}{\Delta\theta}\right)^2 \right\} \tag{69}$$

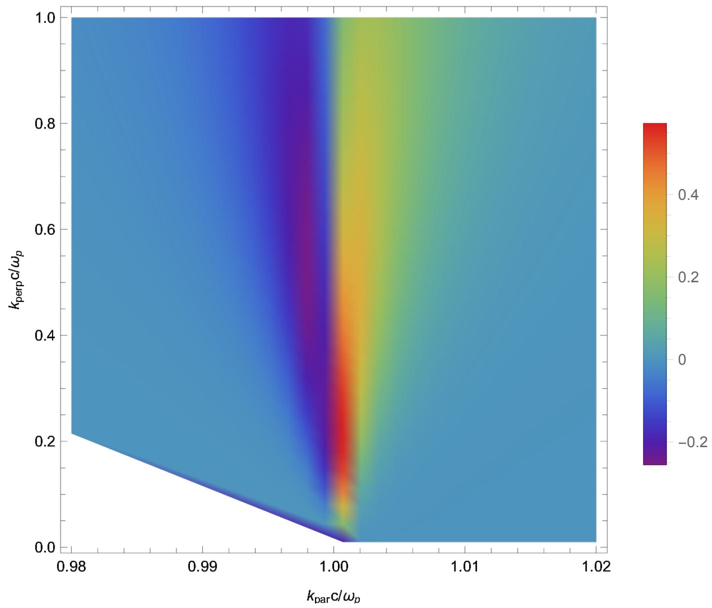

Figure 8: Growth rate maps for a laboratory distribution function with a finite momentum width at injection, as described in Eq. 67 at a Lorentz factor of $\gamma = 40$. The kinetic oblique modes are plotted, with growth rates normalized to the plasma frequency ω_p.

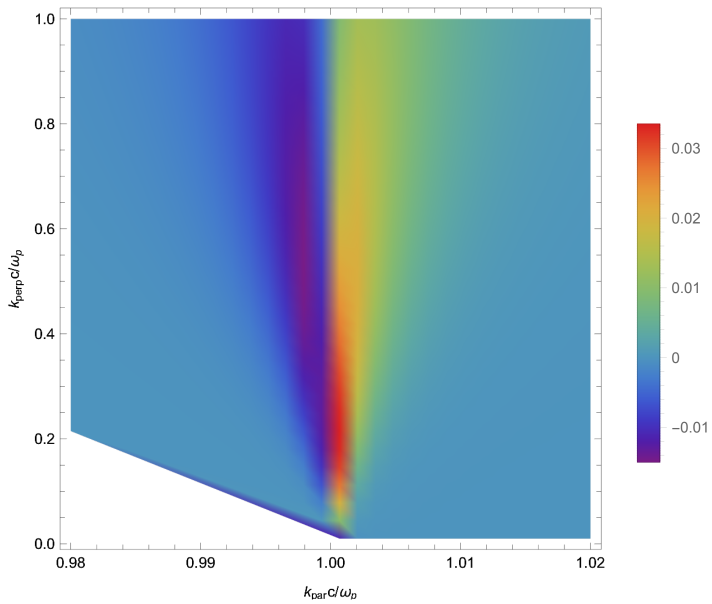

Figure 9: Growth rate maps for a laboratory distribution function with a finite momentum width at injection, as described in Eq. 67 at a Lorentz factor of $\gamma = 60$. The kinetic oblique modes are plotted, with growth rates normalized to the plasma frequency ω_p.

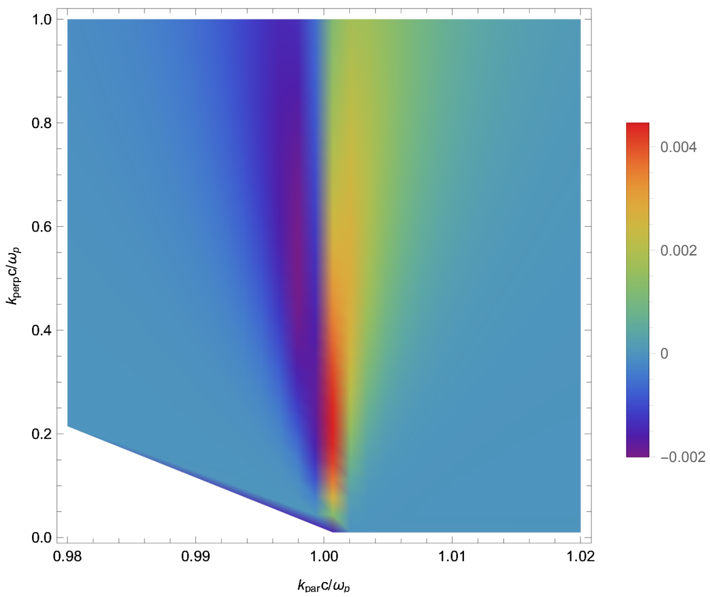

Figure 10: Growth rate maps for a laboratory distribution function with a finite momentum width at injection, as described in Eq. 67 at a Lorentz factor of $\gamma = 80$. The kinetic oblique modes are plotted, with growth rates normalized to the plasma frequency ω_p.

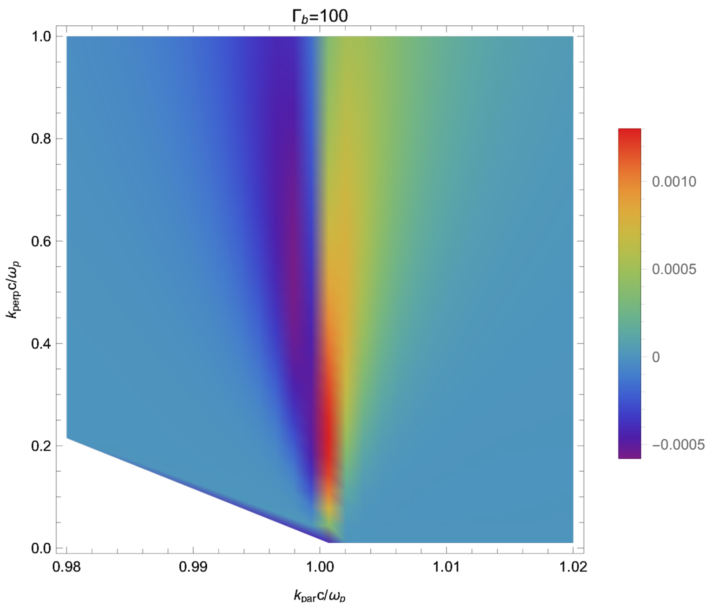

Figure 11: Growth maps for a laboratory distribution function with a finite momentum width at injection, as described in Eq. 67 at a Lorentz factor of $\gamma = 100$. The kinetic oblique modes are plotted, with growth rates normalized to the plasma frequency ω_p.

where the angular width can be expressed as $\Delta\theta = \frac{1}{\gamma} = \frac{m_e c}{p}$.

For such a beam, the angular integral in the expression for kinetic growth rate 60 has been evaluated by [21] through a Monte Carlo simulation which presents the following inverse γ scaling:

$$g(\theta) = \frac{m_e c}{n_b} \int p f(p,\theta) dp \simeq \gamma^{-1} \frac{1}{\Delta\theta^2} e^{-\frac{\theta^2}{\Delta\theta^2}}, \tag{70}$$

where we use three models for beams at a given distance D from the source blazar for comparison with [21]:

- Model 1: $D = 0.87$ Mpc, $\gamma = 1.56 \times 10^5$, $\Delta\theta = 6.43 \times 10^{-5}$
- Model 2: $D = 95.37$ Mpc, $\gamma = 1 \times 10^5$, $\Delta\theta = 9.14 \times 10^{-5}$
- Model 3: $D = 1$ Gpc, $\gamma = 3.9 \times 10^4$, $\Delta\theta = 11.8 \times 10^{-5}$

The corresponding kinetic growth rate maps for realistic blazar beams are calculated using Eq. 59, with the ansatz presented in Eq. 70 and are presented in Figs. 12-14.

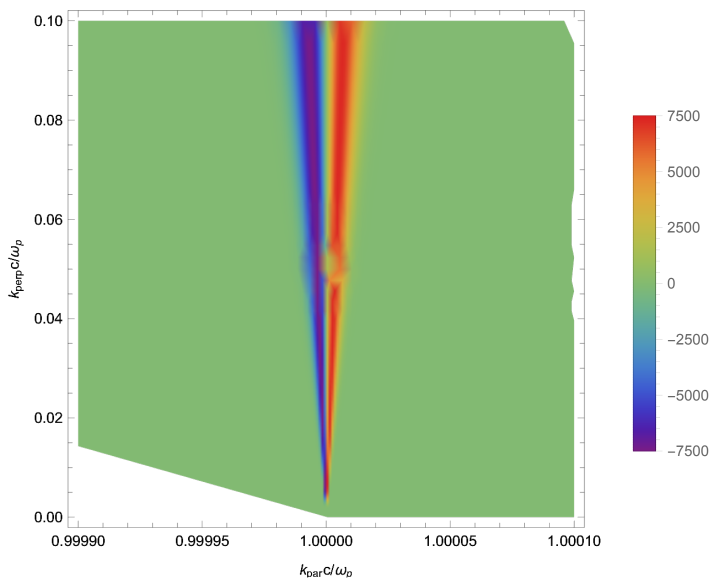

Figure 12: Growth maps for an astrophysical pair beam according to Model 1. The kinetic oblique modes are plotted, with growth rates normalized to the plasma frequency ω_p and the density contrast α..

Thus numerical integration scheme have been shown to reproduce known results from [21] successfully and then has been further applied to computation of growth rates for a realistic distribution function with finite momentum spread, as described in Eq. 67.

As a major difference between the laboratory and astrophysical scenarios, we note that the astrophysical pair beams exhibit unstable modes within a much narrower wave mode window Δk. From 61, one

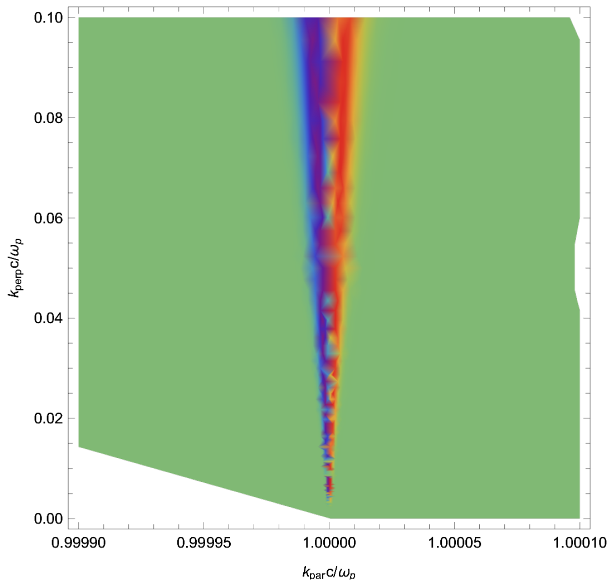

Figure 13: Growth maps for an astrophysical pair beam according to Model 2. The kinetic oblique modes are plotted, with growth rates normalized to the plasma frequency ω_p and the density contrast α.

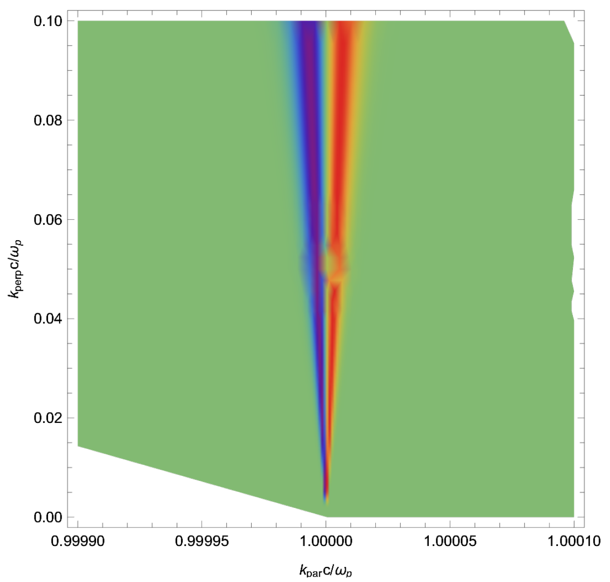

Figure 14: Growth maps for an astrophysical pair beam according to Model 3. The kinetic oblique modes are plotted, with growth rates normalized to the plasma frequency ω_p and the density contrast α.

can see that a part of the k space is excluded by $\sin^2\theta + \cos^2\theta \leqslant 1$ and thus $k_{\parallel}^2 + k_{\perp}^2 \leqslant 1$.

We note that a prominent distinction between the reactive growth rate maps applicable to cold beams as shown in Figs. 5-7, and kinetic growth rate maps, as derived for the laboratory case, in Figs. 8-11, or the astrophysical case, in Figs. 12-14, is that the reactive growth rate is always positive; however, within the resonant window, the kinetic growth rate shows both positive and negative values, i.e., growth and damping. This can be understood by looking at the denominator of the integrand in the expression for the kinetic growth rate in Eq. 59, which has a positive and a negative root for each resonant wave mode k.

2.6 OTHER MODES OF INSTABILITIES

2.6.1 *Modulation instability*

In addition to oblique modes of electrostatic instability, the oscillating case can be understood as modulation instability. The energy density of the electrostatic fluctuations can be expressed as [23], [24]

$$\mathcal{E}_e = n_b m_e c^2 (\gamma - 1). \tag{71}$$

When ions in a turbulent medium scatters as a result of Langmuir oscillation in the beam, the energy density exceeds the critical value [25]

$$\mathcal{E}_{\text{crit}} = \frac{5}{3} \frac{n_p \left(k_B T_p\right)^2}{m_e c^2}, \tag{72}$$

the wave energy shifts to larger phase speeds leading to resonance, and modulation instability is triggered. The corresponding dispersion relation can be solved for the growth rate of:

$$1 = \frac{\omega_p^2}{\omega^2} + \frac{\omega^2 \sin^2\theta \left(1 - \frac{\gamma^2 - 1}{\gamma^2} \cos^2\theta\right)}{\left(\omega - kc\cos\theta\sqrt{\frac{\gamma^2-1}{\gamma^2}}\right)^2} \tag{73}$$

2.6.2 *Weibel modes*

In a departure from the two-stream class of instabilities, Weibel modes occur when in presence of a background magnetic field, anisotropies in velocity field induce fluctuations in the magnetic field perpendicular to the direction of particle motion, which is of the form [26]:

$$\mathbf{B} = B\cos(kz)\mathbf{e}_y. \tag{74}$$

This creates opposing current sheets by virtue of the deflection of the charged pairs in the beam through the Lorentz force from B field fluctuations. A consequence of such current sheets is an overall amplification of the magnetic field. Larger magnetic field strengths induce stronger Lorentz force, and eventually a resonance is reached. The instability has a growth time that can be estimated as [27]:

$$\mathcal{T} = \sqrt{\frac{n_b e^2}{\epsilon_0 m_e \gamma}}, \tag{75}$$

and saturates when the amplification of the magnetic field leads to an increase of the Larmor radii to the level of the plasma skin depth [28]. In parallel, the instability could be short-lived as temperature anisotropies perpendicular to the beam propagation can suppress the growth of Weibel modes.

2.6.3 *Nonlinear Landau damping*

Among nonlinear effects in the beam-plasma system, scattering by thermal ions can alter the frequency and wave mode of a Langmuir wave. Such a damping of the Langmuir oscillation is known as nonlinear Landau damping. The transformation $(\mathbf{k}, \omega) \to (\mathbf{k}', \omega')$ has a timescale $\mathcal{T}_\mathbf{k}$ which is a combination of the instability growth time $\mathcal{T}_{\mathrm{inst}}$ and the growth time for linear Landau damping $\mathcal{T}_{\mathrm{LD}}$,

$$1/\mathcal{T}_\mathbf{k} = 1/\mathcal{T}_{\mathrm{inst}} + 1/\mathcal{T}_{\mathrm{LD}} \tag{76}$$

The evolution of the spectral energy density ϵ_k is governed by the kinetic equation:

$$\frac{d\epsilon_\mathbf{k}}{dt} = 2\frac{\epsilon_\mathbf{k}}{\mathcal{T}_\mathbf{k}} - \frac{\epsilon_\mathbf{k}\omega_{\mathrm{pl}}}{8(2\pi)^{5/2} n_e m_e v_e^2}\int \frac{(\mathbf{k}\cdot\mathbf{k}')}{k^2 k'^2}\phi\left(\mathbf{k}, \mathbf{k}'\right)\epsilon_{\mathbf{k}'} d\mathbf{k}' \tag{77}$$

where $\phi\left(\mathbf{k}, \mathbf{k}'\right)$ is known as the overlap integral [29].

2.7 OTHER RELAXATION MECHANISMS

Self-heating of the beam causes a diffusion in the beam momentum space, causing the beam to broaden its energy spectrum. We explore the impact of this in the evolution of the beam in further details in the following chapter. In presence of magnetic field and considering the presence of ions, the beam can undergo pitch-angle diffusion or magnetic diffusion in addition to self-heating.

2.7.1 *Pitch-angle diffusion*

Thus far, we have ignored collisional effects in the plasma. In presence of magnetic field, or in a turbulent magnetised plasma, the beam pairs can undergo pitch-angle diffusion. The diffusive transport is described by the diffusion coefficient [30]:

$$D_{\mu\mu} = \int_0^\infty dt \langle \dot{\mu}(t)\dot{\mu}(0)\rangle \tag{78}$$

where the acceleration parameter (t) can be described in terms of the stochastic magnetic field variation from a mean magnetic field B_0 as

$$\dot{\mu} = \frac{1}{r_L}\left(v_{\parallel}(t)\frac{\delta B_{\perp}[\mathbf{z}(t), t]}{B_0} - v_{\perp}(t)\frac{\delta B_{\parallel}[\mathbf{z}(t), t]}{B_0}\right) \tag{79}$$

with Larmor radius corresponding to the gyrofrequency Ω:

$$r_L = \frac{v_e}{\Omega} = \frac{v_e m_e c\gamma}{eB_0} = \frac{pc}{eB_0}. \tag{80}$$

2.7.2 *Magnetic diffusion*

In presence of weak tangled magnetic field, the pairs in the beam can undergo random walk. Such magnetic diffusion can be understood in terms of the broadening of the distribution function in terms of the correlation length λ_B associated with the magnetic field strength B_{IGM} as [31]:

$$\Delta\theta = \frac{m_e c}{p}\sqrt{1 + \frac{2}{3}\lambda_B l_{IC}\left(\frac{eB_{IGM}}{m_e c}\right)^2} \tag{81}$$

for a generic astrophysical pair beam distribution over several correlation lengths of the EGMF:

$$f_{b,\theta}(\theta, p) = \frac{1}{\pi\Delta\theta^2}\exp\left\{-\left(\frac{\theta}{\Delta\theta}\right)^2\right\}, \quad 0 \leqslant \theta \leqslant \pi. \tag{82}$$

Here, l_{IC} denotes the lengthscale of the inverse Compton scattering. Let us note that this is a consequence of weak tangled fields. For larger magnetic field strength, a magnetic deflection would take place instead. In presence of primordial strength magnetic fields in voids, such magnetic diffusion holds the potential to, in certain cases, quench the instabilities in the astrophysical pair beams if they are sufficiently broadened and the rates are no longer competitive to those of ICS [32].

3 LABORATORY AND TEV ASTROPHYSICS

This chapter contains a summary an article titled "Evolution of Relativistic Pair Beams: Implications for Laboratory and TeV Astrophysics [33]".

3.1 INTRODUCTION

Blazars, which are abundant in the gamma-ray sky, are typically active galactic nuclei with their jets pointing towards the line of sight. In this work, we focus on BL Lac type objects that peak at high energies. Prompt TeV emissions from such distant sources are reprocessed via their interaction with the extragalactic background light (EBL), leading to pair creations. Among these pairs, the most abundant are electrons and positrons that propagate in the same direction as the emitted TeV photons. Subsequent cooling of these pairs can be attributed to inverse Compton scattering (ICS) when the beam interacts with the cosmic microwave background (CMB) producing GeV gamma rays. However, a discrepancy between the expected [34] and observed flux through various gamma-ray observations of blazars have been reported [2, 11], leading to the so-called "GeV-TeV tension", which is universal among the blazar sources detected. The missing cascade could be due to collective plasma effects [15, 21, 25, 31, 32, 35–42] or deflection of the electron-positron pairs by the cosmic magnetic field. If the ICS is efficient, non-observation of the predicted gamma-ray flux is then utilized to draw a lower bound on the strength of the intergalactic magnetic field (IGMF) [2, 7, 43]. If the IGMF is sufficiently strong, an additional component is expected in the isotropic gamma-ray background (IGRB), and when weaker it can lead to the extended emission known as "pair halos", i.e., bow-tie-like structures around point sources in the gamma-ray sky [44], which are not supported by observations. Recent measurements indicate that the IGMF may be feeble since no excess owing to strong deflections have been observed [45].

In this work, we assess the role of collective plasma effects on the development of electrostatic instabilities. Cherenkov resonance arising from the interaction between the pair beam and the background plasma leads to the growth of unstable modes, which can be electrostatic or electromagnetic in nature [18]. The growth rate of such instabilities, and thus, the fate of the pair beam depends on, among other parameters, the initial distribution function of particles in the pair beam. Whether the instabilities can contribute to significant energy drain [32] has been debated. [46] and [47] respectively argued that inhomogeneities in the IGM plasma and tangled magnetic field can render the instabilities inefficient for astrophysical pair beams. Cosmological implications of such energy drain includes the injection of energy into the IGM plasma that can alter the thermal history and suppress the formation of structures at small scales [15, 48, 49]. We delve into this aspect in Chapter 6 and Chapter 7.

We explore a laboratory-based setup of a beam-plasma system and examine its evolution through analytical and numerical estimates, which can be compared to PIC simulations. In exploring the role of collective plasma processes, it is crucial to understand the temporal evolution of the beam-plasma system and how it differs when the key parameters are changed. The pair beam in question goes through a) a linear growth phase in which the Langmuir oscillations develop and energy is dissipated from the beam into the background plasma through the growing unstable modes, b) a relaxation phase when the particles within the beam, upon encountering electrostatic fluctuations introduced by the instabilities, undergo diffusion, changing the phase space distribution of the beam, and c) the nonlinear phase characterised by Landau damping of the modes, leading the beam to saturation. The extent of the energy dissipation depends on the efficiency of the plasma instabilities. Therefore, it is important to focus on identifying the oscillation modes that are important in driving the instability, sensitivity of the growth rate to the relevant parameters, and the evolution of the energy densities in the beam and the plasma according to the instability growth.

3.2 PLASMA INSTABILITIES AND GROWTH OF MODES

Several kinds of instabilities can set in through the interaction between the beam and the background plasma, based on beam parameters and distribution functions. With an arbitrary beam velocity characterized by $\mathbf{v}$, and wave vector $\mathbf{k}$, the two-stream mode ($\hat{\mathbf{k}}.\hat{\mathbf{v}} = \omega$), the Weibel mode ($\hat{\mathbf{k}}.\hat{\mathbf{v}} = 0$), and the general oblique mode ($\hat{\mathbf{k}}.\hat{v} = \omega \cos\theta$) have been explored [19, 50, 51]. In addition to (semi-)analytical estimates of growth rates, PIC simulations initialized with arbitrary electron distributions have been useful in understanding the evolution of the beam, with the following parameters of significance: the density contrast between the beam and the plasma, the Lorentz factor of the beam, and the energy or momentum spread of the beam [32, 38].

To recall, for a monoenergetic cold beam, i.e., when the momentum spread of the beam $\Delta\mathbf{v}$ is very small, the growth rate of instabilities turns reactive. The maximum reactive growth rate is then derived as $\mathrm{Im} \mid \omega(k) \mid = \delta_r \omega_p$ such that [17]:

$$
\begin{aligned}
\delta_r &= \frac{\sqrt{3}}{2^{4/3}} \left(\frac{2\alpha}{\gamma}\right)^{1/3} \left(\frac{k_\parallel^2}{\gamma^2 k^2} + \frac{k_\perp^2}{k^2}\right)^{1/3} \\
&= \frac{\sqrt{3}}{2^{4/3}} \frac{(2\alpha)^{1/3}}{\gamma} (\cos\theta_0^2 + \gamma^2 \sin{\theta_0}^2)^{1/3}.
\end{aligned}
\tag{83}
$$

Here θ_0 is the initial angle between the wave vector and beam velocity, γ is the beam Lorentz factor, $\alpha = n_b/n_p$ defines the density contrast, with n_b and n_p being the number density of particles in the pair beam and the background plasma, respectively.

For warm beams with finite momentum spreads propagating through a background warm plasma, the growth rate should be computed specifically in the kinetic regime. For ultrarelativistic beams ($v \sim c$) with arbitrary beam distribution function cast in polar coordinates, an approximation exists [22], $f(p, \theta)$, and the normalised growth rate can be written as

$$
\delta_k = -\pi \frac{n_b}{n_p} \left(\frac{\omega_p}{kc}\right)^3 \int_{\mu_-}^{\mu_+} d\mu \frac{2g + \left(\mu - \frac{k_\parallel c}{\omega_p}\right) \frac{\partial g}{\partial \mu}}{[(\mu_+ - \mu)(\mu - \mu_-)]^{\frac{1}{2}}}, \tag{84}
$$

where

$$
g(\theta) = \frac{m_e c}{n_b} \int p f(p, \theta) dp \tag{85}
$$

$$
\mu_\pm = \frac{\omega_p}{kc} \left(\frac{k_\parallel}{k} \pm \frac{k_\perp}{k} \sqrt{\frac{k^2 c^2}{\omega_p^2} - 1}\right). \tag{86}
$$

In a prospective laboratory experiment, we approximate the initially injected beam distribution function with a 2D normal distribution. As the beam undergoes diffusion in momentum space, the the beam widens in momentum space and the growth of instabilities goes from reactive to kinetic in nature. We explore the instability growth without any correlation between the components parallel and normal to the direction of beam propagation. The corresponding growth rates for a beam-plasma system with a density contrast of $\alpha \simeq 10^{-4}$ and beam Lorentz factors of, γ, of 25, 50 and 100 are shown in Fig. 15.

3.3 QUASILINEAR RELAXATION

After the development of Langmuir oscillations, the momentum spread of the injected beam distribution function increases until the beam stabilises according to Penrose's criterion, i.e., when the perpendicular momentum spread becomes comparable to the beam momentum

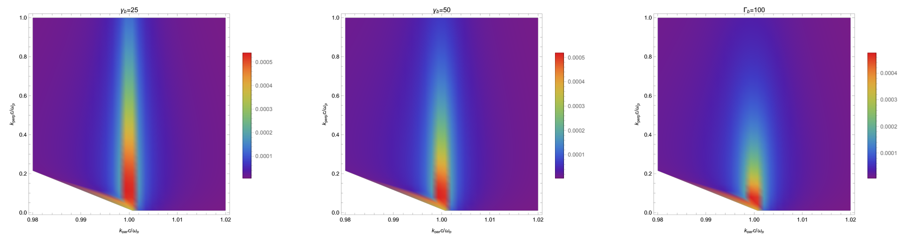

Figure 15: Kinetic growth rate δ_k/ω_p for oblique modes of instability for a density contrast of $\alpha \sim 10^{-4}$ and beam Lorentz factors of $\gamma = 25$, 50 and 100.

characterised by the Lorentz factor [52]. Therefore, even when the beam is monochromatic or narrow in spread at injection, for which the instability growth rate is reactive and occurs over a much shorter timescale, as $t_{inst} \sim 1/\delta$, the quasilinear relaxation widens the energy width of the beam, leading to the instability growing in the kinetic regime. Nonlinear effects such as damping competes with the growth until saturation is achieved.

Thus the beam evolution can be described aptly by the generalized Boltzmann equation in the collisionless regime, which reduces to a Fokker-Planck equation:

$$\frac{\partial}{\partial t} f(\mathbf{p}, t) = -\frac{\partial}{\partial p_i}[\mathbf{fl}_i(\mathbf{p}, t) f(\mathbf{p}, t)] + \frac{\partial}{\partial p_i}[D_{ij}(\mathbf{p}, k, t)\frac{\partial}{\partial p_j} f(\mathbf{p}, t)]. \quad (87)$$

Here the first (drift) term represents energy loss due to instability as $\upsilon(\mathbf{p}, t) = \dot{\mathbf{p}}$ and the second term demonstrates momentum diffusion through the diffusion coefficient D_{ij}.

3.3.1 *Energy loss due to instabilities*

Neglecting collisional energy loss, the spectral energy density of the background plasma grows through the resonant electrostatic unstable modes

$$\frac{\partial W}{\partial t} = 2(\mathrm{Im} \mid \omega \mid) W. \quad (88)$$

For a laboratory plasma, the beam Lorentz factor is not as high compared to astrophysical plasmas. This implies that the energy loss through instabilities is not suppressed. However, the diffusion term widens a cold beam into a beam with significant sporead in momentum. Even though the overall growth rate is determined by the reactive growth rate, the widening leads to the instability proceeding in kinetic regime, in which the subsequent growth rate falls below the reactive rate.

3.3.2 *Diffusion in momentum space*

The momentum-diffusion tensor can be determined by the mode-weighted spectral energy density at resonance for an initial phase-averaged ensemble [22]:

$$D_{\alpha\beta} = \pi e^2 \int W(\mathbf{k}, t) \frac{k_\alpha k_\beta}{k^2} \delta(\mathbf{k} \cdot \mathbf{v} - \omega) d^3k \tag{89}$$

The diffusion coefficients depend on beam momenta through the growth rate in the exponent in the expression for the spectral energy density by virtue of the beam distribution function used. In this treatment of the momentum diffusion in the beam-plasma system, the delta function associated with the resonance condition in Eq. 89 combs through the modes and picks up the corresponding fastest growing modes contributing to the growth of the spectral energy density, i.e.,

$$W(\mathbf{k}, t) \,|_{\mathbf{k}\mathbf{fl} = \omega_p} = W_{\text{resonant}}(t) = W_0 \int_0^t \exp[2\delta_{\max} \omega_p t]. \tag{90}$$

Here $\delta_{\max}$ is the maximum growth rate of the plasma instabilities normalised in terms of plasma frequency and W_0 is the initial energy in the plasma that can be estimated as the thermal energy of the background electrons. For astrophysical beam this corresponds to the temperature of the IGM ($\mathcal{O}(\sim 10\text{keV})$). In a laboratory set up, the corresponding temperature is of the order of electronVolts. After an initial phase of growing instabilities which can be described using the linear theory, the beam undergoes diffusion in momentum space. The quasilinear approximation applies until the nonlinear damping leads to instability saturation.

3.3.3 *Drift term*

The first term in the RHS of Eq. 87 represents a “drift”, i.e., an energy drain from the beam into the background plasma. As the pair beam cools, the background field energy increases. The drift coefficient υ is determined in the parallel direction as:

$$\upsilon_{||}(\mathbf{p}, t) = \dot{p}_{||} = \delta\omega_p \frac{W(t)}{n_b} \tag{91}$$

The spectral energy density of the waves can then grow according to

$$W(\mathbf{k}, t) = W_0(\mathbf{k}) \exp[2\delta_{\mathbf{k}} \omega_p t], \tag{92}$$

$W_0 = n_e k_B T_e$ being the initial spectral energy described by the thermal fluctuations, which serves as a noise floor.

The above follows immediately from the growth of the electrostatic field energy owing to instability with a growth rate of δ in units of plasma frequency ω_p in the direction of beam propagation. In the direction perpendicular to it, the beam momenta is relatively small. Since $p_\perp \ll p_{||}$, the drift in transverse direction can be ignored for pair beams designed for laboratory astrophysics.

3.3.4 *Diffusion term*

The second term in Eq. 87 shows diffusion in momentum space and the diffusion coefficient in its general form can be decomposed into two diagonal and two off-diagonal contributions. The Cherenkov resonance condition represented in the delta function of the integrand chooses only the fastest growing resonant mode. Thus, the diffusion coefficients in the 2D Cartesian system can be expressed as:

$$D_{\alpha\beta} \sim \pi e^2 \frac{W_0}{\omega_p} \exp[2\delta_{max}\omega_p t] J_{\alpha\beta} \,, \tag{93}$$

where

$$J_{\alpha\beta} = \omega_p \frac{\int d^3k\, W(\mathbf{k}, t) \frac{k_\alpha k_\beta}{k^2} \delta(\mathbf{k} \cdot \mathbf{v} - \omega)}{\int d^3k\, W(\mathbf{k}, t)} \,. \tag{94}$$

Here $J_{||} \sim J_\perp \sim \mathcal{O}(1 - 10)\omega_p$, and the off-diagonal terms vanish as $J_{||,\perp} = J_{\perp,||} = 0$.

3.3.5 *Comparison between the drift and diffusion term*

It is important to understand the hierarchy between the drift and the diffusion term in order to chart out the evolution of the pair beam distribution function via the Fokker-Planck equation. On the one hand, if the drift term is much larger than the diffusion term, the system is advective in momentum space, and the main impact of the Fokker-Planck evolution would then be energy loss. On the other hand, when the diffusion term leads, momentum broadening will determine the primary outcome of the pair beam evolution. The relative impact of the two terms can be evaluated as follows.

At first, we perform a comparison along the direction of propagation. The diffusion coefficient is expressed in terms of the spectral energy density of the electromagnetic fields:

$$D_{||} = \pi e^2 W(t) J_{||}. \tag{95}$$

The drift coefficient reads

$$\dot{p_{||}} = \delta\omega_p E = \delta\omega_p \frac{W(t)}{n_b}. \tag{96}$$

Thus, the dimensionless ratio of the two terms is

$$\frac{p_{||}\dot{p_{||}}}{D_{||}} = \frac{p_{||}}{\pi e^2 W(t)} \frac{\delta\omega_p^2 W(t)}{n_b} = \frac{p_{||}}{\pi e^2} \frac{\delta\omega_p^2}{n_b J_{||}}. \tag{97}$$

Using the definition of plasma frequency, $\omega_p = \sqrt{\frac{4\pi n_e e^2}{m_e}}$, and $p_{||} = \gamma m_e$,

$$\frac{p_{||}\dot{p_{||}}}{D_{||}} \approx \delta\frac{\gamma}{\alpha}. \tag{98}$$

For standard laboratory plasma conditions with $\gamma = 100$, $\alpha = 10^{-3}$ and a kinetic maximum growth rate, $\frac{p_{||}\dot{p_{||}}}{D_{||}} \sim \mathcal{O}(1-10)$.

The transverse momentum $p_\perp$ being very small, $\frac{p_\perp \dot{p_\perp}}{D_\perp} \ll 1$ and diffusion is the leading phenomenon in the direction perpendicular to beam propagation.

3.4 NUMERICAL SCHEME: AN OUTLINE

3.4.1 *The Fokker Planck Equation*

The Fokker-Planck equation is a partial differential equation describing the evolution of the beam distribution function with a drift term characterising the energy loss owing to the plasma instabilities and a diffusive term representing diffusion in momentum space.

$$\frac{\partial}{\partial t} f(\mathbf{p},t) = -\frac{\partial}{\partial p_i}\left[v_i(\mathbf{p},t) f(\mathbf{p},t)\right] + \frac{\partial}{\partial p_i}\left[D_{ij}(\mathbf{p},k,t)\frac{\partial}{\partial p_j} f(\mathbf{p},t)\right] \tag{99}$$

If we consider a 2D Cartesian system with $p_{||}$ and $p_\perp$ representing momenta in forward and transverse direction, such that $i,j = ||, \perp$, in addition to the homogeneous terms, we also obtain off-diagonal components for the diffusion term.

3.4.2 *Change of variables*

Thus, Eq. 99 has the form

$$\begin{aligned}\left(\frac{\partial f(\mathbf{p},t)}{\partial t}\right) &= -\frac{\partial}{\partial p_{||}}\left[v_{||}(\mathbf{p},t) f(\mathbf{p},t)\right] - \frac{\partial}{\partial p_\perp}\left[v_\perp(\mathbf{p},t) f(\mathbf{p},t)\right] \\ &+ \frac{\partial}{\partial p_{||}}\left[D_{||}(\mathbf{p},k,t)\frac{\partial}{\partial p_{||}} f(\mathbf{p},t)\right] + \frac{\partial}{\partial p_\perp}\left[D_\perp(\mathbf{p},k,t)\frac{\partial}{\partial p_\perp} f(\mathbf{p},t)\right]\end{aligned}$$

(100)

Such a PDE can typically be numerically solved using a finite difference solution scheme, which is unstable at late times owing to the exponential time-dependence of the drift and diffusion term. In order to tackle this problem, performing a change of variable $d\tau = \exp[2\delta\omega_p t]dt$ is necessary and Eq. 100 can be rewritten as:

$$\frac{\partial f(\mathbf{p},\tau)}{\partial \tau} = -\frac{\partial}{\partial p_{||}}\left[\Upsilon f(\mathbf{p},\tau)\right] + \left[\mathcal{D}_{||}\frac{\partial^2 f(\mathbf{p},\tau)}{\partial p_{||}} + \mathcal{D}_{\perp}\frac{\partial^2 f(\mathbf{p},\tau)}{\partial p_{\perp}}\right] \tag{101}$$

where

$$\Upsilon = \delta\omega_p \gamma m_e c \tag{102}$$

and

$$\mathcal{D}_{||} = \pi e^2 W_0 J_{||} \tag{103}$$

$$\mathcal{D}_{\perp} = \pi e^2 W_0 J_{\perp} \tag{104}$$

3.4.3 *Finite difference method*

In order to solve the PDE in Eq. 101, we use Finite Difference Method (FDM), which relies on spacetime discretization into finite-sized numerical grids. First derivative of of an arbitrary function $u(x, y)$ can be expressed as:

$$u_{i+1,j+1} = u_{i,j} + \left(\Delta x\frac{\partial}{\partial x} + \Delta y\frac{\partial}{\partial y}\right)u\bigg|_{i,j} + \frac{1}{2}\left(\Delta x\frac{\partial}{\partial x} + \Delta y\frac{\partial}{\partial y}\right)^2 u\bigg|_{i,j} + \cdots + \text{h.o.t} \tag{105}$$

for which forward difference can be propagated along the x line as:

$$\frac{\partial u}{\partial x}\bigg|_{i,j} = \frac{u_{i+1,j} - u_{i,j}}{\Delta x} + O(\Delta x) \tag{106}$$

$$\frac{\partial u}{\partial y}\bigg|_{i,j} = \frac{u_{i,j+1} - u_{i,j}}{\Delta y} + O(\Delta y) \tag{107}$$

Similarly, backward difference

$$\left.\frac{\partial u}{\partial x}\right|_{i,j} = \frac{u_{i,j} - u_{i-1,j}}{\Delta x} + O(\Delta x) \tag{108}$$

$$\left.\frac{\partial u}{\partial y}\right|_{i,j} = \frac{u_{i,j} - u_{i,j-1}}{\Delta y} + O(\Delta y) \tag{109}$$

and centered difference

$$\left.\frac{\partial u}{\partial x}\right|_{i,j} = \frac{u_{i+1,j} - u_{i-1,j}}{2\Delta x} + O\left(\Delta x^2\right) \tag{110}$$

$$\left.\frac{\partial u}{\partial y}\right|_{i,j} = \frac{u_{i,j+1} - u_{i,j-1}}{2\Delta y} + O\left(\Delta y^2\right) \tag{111}$$

can be derived.
Similarly, for a second derivative, forward difference

$$\left.\frac{\partial^2 u}{\partial x^2}\right|_{i,j} = \frac{u_{i+2,j} - u_{i,j}}{\Delta x^2} + O\left(\Delta x^2\right) \tag{112}$$

$$\left.\frac{\partial^2 u}{\partial y^2}\right|_{i,j} = \frac{u_{i,j+2} - u_{i,j}}{\Delta y^2} + O\left(\Delta y^2\right) \tag{113}$$

backward difference

$$\left.\frac{\partial^2 u}{\partial x^2}\right|_{i,j} = \frac{u_{i,j} - u_{i-2,j}}{\Delta x^2} + O\left(\Delta x^2\right) \tag{114}$$

$$\left.\frac{\partial^2 u}{\partial y^2}\right|_{i,j} = \frac{u_{i,j} - u_{i,j-2}}{\Delta y^2} + O\left(\Delta y^2\right) \tag{115}$$

and centered difference

$$\left.\frac{\partial^2 u}{\partial x^2}\right|_{i,j} = \frac{u_{i+1,j} - 2u_{i,j} + u_{i-1,j}}{\Delta x^2} + O\left(\Delta x^2\right) \tag{116}$$

$$\left.\frac{\partial^2 u}{\partial y^2}\right|_{i,j} = \frac{u_{i,j+1} - 2u_{i,j} + u_{i,j-1}}{\Delta y^2} + O\left(\Delta y^2\right) \tag{117}$$

3.4.4 *Implementation and stability*

We solve the Fokker-Planck equation in its modified form, Eq. 101 with a forward propagation in time and an upwind scheme in space for the drift term and a centered difference scheme in space for the diffusion term. The reason for this hybrid approach is due to the fact that the drift term, containing a first derivative, when treated with a forward in time and centered in space approach, unlike the diffusion term, is unconditionally unstable. Therefore, we use an upwind scheme, i.e., a backward difference in space to treat the first derivative in the drift term. It is also to be noted that an upwind scheme in an advection-like term, such as our drift term, introduces a numerical diffusion.

The hybrid approach gives us a solution that is close to the actual solution of the Fokker-Planck equation in amplitude as long as the numerical diffusion is counteracted by the physical diffusion term in Eq. 101.

For a function $f(p_{||}, p_{\perp}; \tau)$ discretized as $\Phi_{i,j}^{(n)}$, such that $p_{||} = i\Delta p_{||}$, $p_{\perp} = j\Delta p_{\perp}$, and $\tau = n\Delta\tau$, on the domain of unit square $0 \leqslant p_{||} < 1$ and $0 \leqslant p_{\perp} < 1$.

Thus,

$$\begin{aligned} \Phi_{i,j}^{(n+1)} = \Phi_{i,j}^{(n)} &+ \Delta\tau \left[\Upsilon_{||} \frac{\Phi_{i,j}^{(n)} - \Phi_{i-1,j}^{(n)}}{\Delta p_{||}} + \Upsilon_{\perp} \frac{\Phi_{i,j}^{(n)} - \Phi_{i,j-1}^{(n)}}{\Delta p_{\perp}} \right] \\ &+ \Delta\tau \left[\mathcal{D}_{||} \frac{\Phi_{i+1,j}^{(n)} - 2\Phi_{i,j}^{(n)} + \Phi_{i-1,j}^{(n)}}{(\Delta p_{||})^2} + \mathcal{D}_{\perp} \frac{\Phi_{i,j+1}^{(n)} - 2\Phi_{i,j}^{(n)} + \Phi_{i,j-1}^{(n)}}{(\Delta p_{\perp})^2} \right], \end{aligned} \tag{118}$$

where since $\Upsilon_{\perp} \ll \Upsilon_{||}$, we can ignore the second term within the first parenthesis, and set $\Upsilon_{||} = \Upsilon$.

The stability of the hybrid scheme depends both on the drift and diffusion coefficients and can be derived from the following conditions

$$-\left(\frac{\mathcal{D}_{||}\Delta p_{||}^2 + \mathcal{D}_{\perp}\Delta p_{\perp}^2}{\Delta p_{||}^2 \Delta p_{\perp}^2} \right) \Delta\tau \leqslant \left(\frac{\Upsilon_{||}\Delta p_{||} + \Upsilon_{\perp}\Delta p_{\perp}}{\Delta p_{||}\Delta p_{\perp}} \right) \Delta\tau \leqslant 1 - 2\left(\frac{\mathcal{D}_{||}\Delta p_{||}^2 + \mathcal{D}_{\perp}\Delta p_{\perp}^2}{\Delta p_{||}^2 \Delta p_{\perp}^2} \right) \Delta\tau \tag{119}$$

and

$$0 \leqslant \frac{2\left(\mathcal{D}_{||}\Delta p_{||}^2 + \mathcal{D}_{\perp}\Delta p_{\perp}^2 \right)}{\Delta p_{||}^2 \Delta p_{\perp}^2} \leqslant 1 \tag{120}$$

Thus the Courant criterion is then defined as:

$$\Delta\tau \leqslant \frac{1}{\left[\frac{(\Upsilon_{||}\Delta p_{||}+\Upsilon_{\perp}\Delta p_{\perp})}{\Delta p_{||}\Delta p_{\perp}} + \frac{2\left(\mathcal{D}_{||}\Delta p_{||}^2+\mathcal{D}_{\perp}\Delta p_{\perp}^2\right)}{\Delta p_{||}^2\Delta p_{\perp}^2}\right]} \tag{121}$$

After solving the Fokker-Planck equation with the relevant change of variables using the combined upwind and FTCS scheme, we reexpress the solution in terms of physical time t.

A realistic modelling of collective plasma effects is possible only to the extent linear theory and quasilinear approximations allow. Beyond these regimes, nonlinear effects become important, a direct consequence of which is saturation and beam stabilization.

3.5 SOLUTION TO THE FOKKER-PLANCK EQUATION

The Fokker-Planck equation is numerically solved using a finite difference scheme for a density contrast $\alpha = 10^{-3}$, background plasma temperature $T_e = 500$ eV, plasma density $n_e = 10^{26}\text{cm}^{-3}$, and the time evolution of the beam distribution function is plotted for various values of beam Lorentz factor $\gamma = 25, 50,$ and 100 in Fig. 16.

The time evolution of the beam distribution function demonstrates the impact of the energy loss and diffusive processes. The initial width of the Gaussian beam is set to the minimum grid resolution. Further details on the numerical finite-difference scheme adapted is provided below.

We also present a 1D slice of the distribution function for a beam with $\gamma = 100$ at $p_{\perp} = 0$ is shown in Fig. 17. The corresponding changes in the momentum distribution are governed by an exponentially growing drift coefficient $D_i(t)$ that transfers the energy from the beam such that the mean is shifted as

$$\Delta\mu_i \propto \exp[2\delta\omega_p t] \tag{122}$$

in each dimension i. Similarly, the diffusion coefficient $\mathcal{D}_i(\tau)$ scales as $\sqrt{\tau}$. This implies that a physical diffusion coefficient has the time-dependence:

$$D_i(t) \propto \exp[\delta\omega_p t]. \tag{123}$$

These effects Figs. 18 and 19, where the time evolution of the drift of the mean momentum and width of the momentum about the mean are shown for the parallel direction. We note that the drift coefficient represented by the change in mean momentum grows exponentially with an argument twice the growth rate while the diffusion coefficient

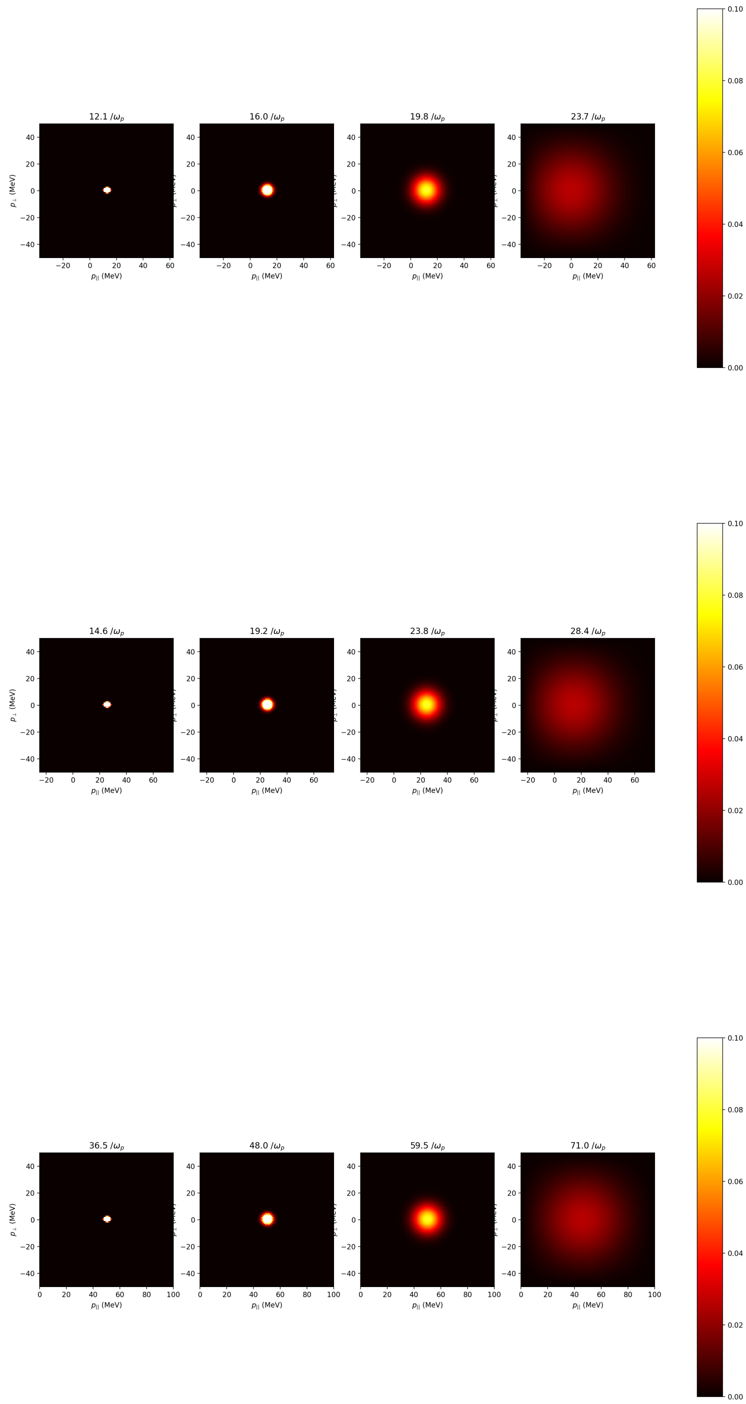

Figure 16: Beam distribution function in $p_{||} - p_{\perp}$ plane at various timesteps in the units of inverse plasma frequency. Eq. 87 is solved for a plasma with number density $n_{pl} = 10^{26}$ cm^{-3}, density contrast $\alpha \sim 10^{-3}$ and beam Lorentz factors of $\gamma = 25, 50$, and 100. The background temperature is 500 eV and the the color scale has a unit of MeV^{-2}. The above figures portray the advective and diffusive Fokker-Planck evolution of the beam through energy loss (shift of the mean energy) and a momentum broadening (diffusive behaviour). The beam evolution is shown until linear perturbation calculations are valid, i.e., before nonlinear effects become important. Time is expressed in units of plasma period.

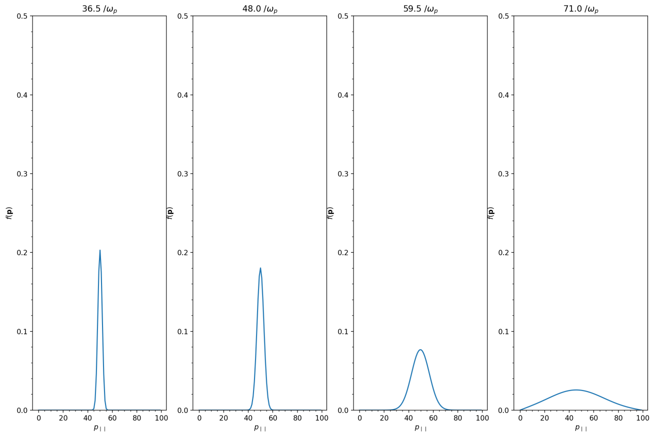

Figure 17: One-dimensional slices of the the distribution function at $p_\perp = 0$ is plotted against the parallel momentum $p_{||}$ for various timesteps tracing the evolution of the normalized distribution function. Time is expressed in units of plasma period.

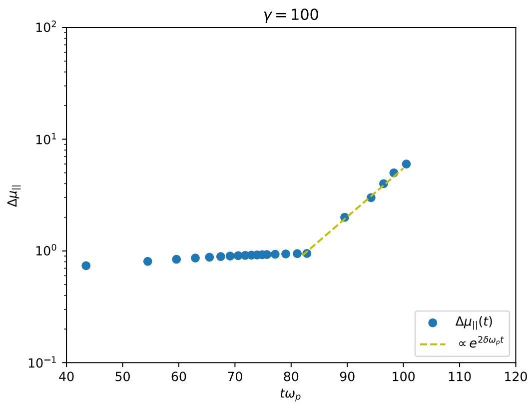

Figure 18: The time evolution of the drift of the mean momentum of the distribution, governed by the Fokker-Planck equation is shown for the parallel direction in blue points, which at late times shows exponential growth as the drift coefficient increases exponentially.

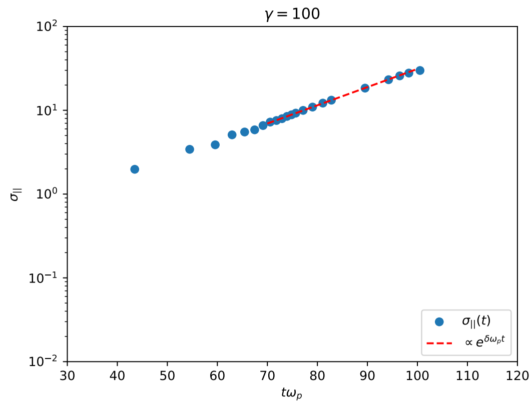

Figure 19: The time evolution of the momentum width of the pair beam, governed by the Fokker-Planck equation is shown for the parallel direction in blue points, which is dominated by exponential growth as can be expected from the exponentially growing diffusion coefficient.

represented by the standard deviation has an exponent equal to the growth rate of the instabilities. This is consistent with the analytical findings and PIC simulation results presented in the article [33].

3.6 DISCUSSIONS

From this investigation, we note that in addition to plasma heating via instability losses, a quasilinear relaxation phase occurs, the main consequence of which is then a momentum diffusion within the beam. Such diffusive processes can change the beam distribution function from its initial configuration, as well as affect the energy partition in the beam-plasma system. Since the fate of beam-plasma systems is determined by a horde of microscopic phenomena, collective plasma effects serve as an excellent tool to trace their evolution. A beam propagating through the plasma induces Langmuir oscillations that enter Cherenkov resonance associated with electrostatic instability as $\omega - \vec{k} \cdot \vec{v} = 0$. When the initial injection of the beam is energetically narrow or even monochromatic, the instability grows reactive and its growth rate is estimated hydrodynamically. When the velocity or momentum spread of the beam Δv is not insignificant, $\mid \vec{k} \cdot \Delta\vec{v} \mid > \mathrm{Im} \mid \omega(\vec{k}) \mid$, the instability grows kinetically for most k's. This is a direct consequence of the quasilinear relaxation. During this self-heating phase, the diffusion in momentum space will continue broadening the beam until the beam is completely relaxed, i.e., change in the angular width of the beam approaches the initial beam width $\Delta\theta \sim \theta_0$. The overall beam evolution can be traced using the Fokker-Planck equation, Eq. 87, where the drift term describes the energy drain owing to instabilities and relaxation is governed by the diffusion term, as seen in Fig. 16, as supported by the results from PIC simulation with similar parameters as shown in [33]. In the final stages of the beam evolution, nonlinear damping effects become important.

From the analysis we draw a few major differences between the instability growth for a cold and that of a warm beam. For a cold beam, the window of resonance in Fourier space is narrow in Δk. However, a realistic astrophysical pair beam is energetically broader. When the instability proceeds in the kinetic regime, the energy drain from the beam is not as efficient since it grows exponentially with an argument proportional to the instability growth rate. In conjunction, broadening turns out to be as important a feature of these beams. The timescale of development for each phase and how long they are sustained depend on beam parameters such as the beam Lorentz factor, beam-plasma density contrast, and the initial beam distribution function at injection.

The investigation in the idealized conditions of a narrow Guassian 2D beam propagating through a homogeneous cold plasma differs from the astrophysical scenario. In addition, inhomogeneity in the plasma can affect the growth and development of instabilities. A characteristic length scale L_{inhom} associated to instabilities can be defined in the direction parallel to beam such that

$$L_{||} \sim \left| \frac{\partial \ln n_p}{\partial z} \right|^{-1} . \tag{124}$$

In presence of inhomogeneity, the relaxation proceeds under the condition that the initial angular width of the beam is smaller than a critical value set by the inhomogeneity length scale, i.e., $\theta_0 < 1/\mu_{||}\Lambda$. The parameter $\mu_{||}$ can be defined as

$$\mu_{||} = \frac{c}{\omega_p L_{||}} \frac{\gamma}{\alpha} \tag{125}$$

however, when the broadening of the beam increases the angular width of the beam reaching $\theta \sim 1/\mu\Lambda$, the beam stops expanding [53], [46]. Limiting our calculation to the quasilinear case, we set the parameter $\Lambda \sim 1 - 10$ for laboratory plasma with a number density $n_p = 10^{16}\text{cm}^{-3}$. For a beam Lorentz factor $\gamma \sim 10$ and a density contrast $\alpha \sim 10^{-3}$, the inhomogeneity lengthscale can be estimated in the parallel direction as $L_{||} \sim 1$ cm. This implies that the instability is quenched when the inhomogeneity exceeds 0.1% for a plasma of radius 10 cm. An inhomogeneity lengthscale in the transverse direction can be defined and evaluated in the same fashion.

In order to observe the instability growth in a laboratory astrophysics experiment, it is required that the beam is kept nearly constant for the time the instability grows, equivalent to a distance of propagation. The propagation distance needed for the instability to grow is proportional to the growth rate δ and thus depends on the plasma density as well. For parameters $\alpha = 10^{-3}$, $\gamma = 100$ and $n_{bg} = 10^{16}\,\mathrm{cm}^{-3}$ this distance is roughly $3\,\mathrm{cm}$. if the beam number density is held constant and the background density is increased, the physical propagation distance decreases, since $\omega_p \propto n_{bg}^{\frac{1}{2}}$ but $\delta \propto \alpha^{\frac{1}{3}} \propto n_{bg}^{\frac{1}{3}}$. For a beam of finite length and width, as is the case for laboratory beam-plasma systems, an increase in the length and width in units of the plasma wavelength translates to the system more closely resembling the infinitely extended beam discussed in this work.

3.7 SUMMARY AND OUTLOOK

We describe the evolution of relativistic dilute neutral pair beams consisting of electrons and positrons propagating through a cold plasma through collective plasma processes. In the initial phase, the beam exhibits Langmuir oscillations with unstable modes that drives an exponential growth of the spectral energy density of the plasma. In absence of magnetic field, the most important instabilities are the oblique electrostatic instability and the growth rate derived with linear perturbation theory is valid. In the following phases, the beam goes through a relaxation phase and we describe the self-heating of the beam in terms of quasilinear approximations where initial width is also a key parameter which determines the extent of instability losses and momentum diffusion in the beam.

In a laboratory setup, in order to create and observe oblique instability, we need a positive slope in the longitudinal momentum distribution of the input pair beam. Through irradiation of a high-Z conversion target with a high energy particle beam, electron-positron pairs are produced from Bremsstrahlung photons. The resultant spectrum should then exhibit a large transverse divergence and a broad energy spectrum, which was first shown in [54] and subsequently investigated in [55]). This work demonstrates that the growth of the electric field energy via instability modifies the momentum distribution pertaining to the beam, leading to an increase in the beam opening angle. The broadening of the momentum distributions can proceed exponentially until a saturation of the instability growth. For dilute, relativistic beams, the growth rate and saturation level have power law scaling with α and γ. The rate of widening is the same as the growth rate of the electric field amplitude of the instability.

Inhomogeneities in the plasma can lead to a suppression of the instability growth and contribute as an additional source of beam relaxation. Initial correlation in beam distribution function between the parallel and perpendicular direction can modify the evolution of the beam. In similar vein, nonlinear damping effects that lead to a saturation of the unstable modes should be considered for a more complete treatment. The next step would be to trace the beam evolution in a magnetized plasma in order mimic the astrophysical case better. The above constitute future directions that will be explored in upcoming work.

4 FATE OF ASTROPHYSICAL BEAMS

In this chapter, some estimates are presented on the fate of an astrophysical pair beam, and subsequently the prospect of observing the impact of plasma instabilities and momentum diffusion in more extreme scenarios compared to the laboratory case is explored. The number density of the free electrons in the intergalactic medium at mean density and present time is $n_{IGM,0} = 2.2 \times 10^{-7} cm^{-3}$, which evolves with redshift z and overdensity Δ according to

$$n_{IGM} \equiv n_{IGM,0}(\Delta)(1+z)^3. \tag{126}$$

The pair production mean free path D_{pp} can be written as [15]

$$D_{pp}(E, z) = 35 \left(\frac{E}{1\text{TeV}}\right)^{-1} \left(\frac{1+z}{2}\right)^{-\zeta} \text{Mpc} \tag{127}$$

with $\zeta = 4.5$ for $z < 1$ and $\zeta = 0$ for $z \geqslant 1$ [56] [7], and the photon spectra

$$F_E = E\frac{dN}{dE}\,, \tag{128}$$

is of the form

$$\frac{dN}{dE} = f_0 \left(\frac{E}{E_0}\right)^{-\alpha'}\,, \tag{129}$$

where E_0 is peak spectral energy in TeV, f_0 is a factor of normalization with units of $cm^{-2}s^{-1}TeV^{-1}$ and index α' is a combination of the index of spectra for injection at the source α and the optical depth,

$$\alpha' = \alpha_{source} + \tau\left(E_0, z\right). \tag{130}$$

The optical depth for gamma rays of energy E depends on redshift z, Hubble function $H(z)$, and the pair production mean free path:

$$\tau_E(E, z) \equiv \int_0^z \frac{c dz'}{D_{pp}\left(E\left(1+z'\right)/(1+z), z'\right) H\left(z'\right)\left(1+z'\right)}. \tag{131}$$

4.1 IMPACT OF PLASMA INSTABILITY ON PAIR BEAM SPECTRA

The number density of charged particles in astrophysical pair beams is determined by the injection from the blazar source and estimated at present day to be $n_{b,0} \sim 10^{-22}\text{cm}^{-3}$ [15]. The pair beam density is determined by the duration of the TeV emission during the period of blazar activity, pair production rate, pair cooling rate and the cascading processes in consideration. Therefore, the evolution of pair density per unit Lorentz factor n_γ can be described using a Boltzmann equation, which can be written as $n_b = \gamma n_\gamma$. Through the pair production $E \simeq 2\gamma m_e c^2$. The flux of gamma-rays N is such that

$$\gamma \dot{n}_\gamma = \frac{2}{D_{pp}} \left(E \frac{dN}{dE} \right) = \frac{2F_E}{D_{pp}}. \tag{132}$$

The evolution of n_γ can be described in terms of Boltzmann equation in its general form [15]:

$$\frac{\partial n_\gamma}{\partial t} + \frac{c}{r^2} \frac{\partial r^2 n_\gamma}{\partial r} + \dot{\gamma} \frac{\partial n_\gamma}{\partial \gamma} = \dot{n}_\gamma, \tag{133}$$

where distance from the source r is measured radially in a spherical coordinate system. Since n_γ does not change appreciably over large distances comparable to the pair production mean free path D_{pp}, one can ignore the advection term $c/r^2 \partial(r^2 n_\gamma)/\partial r$ [15]. It can be assumed that the TeV blazar emission occurs over a long period of time such that a steady-state is reached, thus setting the first term on the LHS to zero $\partial n_\gamma / \partial t = 0$. Therefore, Eq. 133 reduces to:

$$\dot{\gamma} \frac{\partial n_\gamma}{\partial \gamma} = \dot{n}_\gamma. \tag{134}$$

At this point, the energy loss term can be split into the energy loss due to ICS, $\dot{\gamma}_{ICS}$, and that due to instability losses, $\dot{\gamma}_{inst}$:

$$\dot{\gamma} = \dot{\gamma}_{\text{ICS}} + \dot{\gamma}_{\text{inst}} \tag{135}$$

using which we rewrite Eq. 134 as

$$\left(\frac{\dot{\gamma}_{\text{ICS}}}{\gamma} + \frac{\dot{\gamma}_{\text{inst}}}{\gamma} \right) \frac{\partial n_\gamma}{\partial \gamma} = \frac{\dot{n}_\gamma}{\gamma}. \tag{136}$$

Using Eq. 132, we can write Eq. 136 terms of the ICS and instability rates, Γ_{ICS} and Γ_{inst}, respectively, as

$$(\Gamma_{\text{ICS}} + \Gamma_{\text{inst}}) \frac{\partial n_\gamma}{\partial \gamma} = \frac{2\kappa_0}{D_{pp}} \gamma^{-(1+\alpha')}, \tag{137}$$

where $\kappa_0 = f_0 E_0^{\alpha'}$. We note that the rate of inverse Compton scattering is given by

$$\Gamma_{ICS} = \frac{4\sigma_T u_{CMB}}{3m_e c}\gamma \simeq 1.4 \times 10^{-20}(1+z)^4 \gamma s^{-1}, \tag{138}$$

where σ_T is the Thomson cross-section, and u_{CMB} is the energy density of the cosmic microwave background (CMB). Without assuming a specific unstable mode, a generic expression for the cooling rate owing to an electrostatic instability can be written in terms of the plasma frequency ω_p corresponding to that of the IGM, density contrast $\alpha = n_b/n_{IGM}$ and the Lorentz factor γ,

$$\Gamma_{inst} \approx \frac{\alpha}{\gamma}\omega_p. \tag{139}$$

Redefining the following variables

$$b_1 = \frac{4\sigma_T}{3m_c c} u_{CMB}, \tag{140}$$

$$b_2 = \alpha\omega_p, \tag{141}$$

and

$$b_3 = \frac{2\kappa_0}{D_{pp}}, \tag{142}$$

Eq. 137 can be cast as

$$\left(b_1\gamma + \frac{b_2}{\gamma}\right)\frac{\partial n_\gamma}{\partial \gamma} = b_3\gamma^{-(1+\alpha')}, \tag{143}$$

which can further be simplified to

$$\left(b_1\gamma + \frac{b_2}{\gamma}\right)\left[\frac{1}{\gamma}\frac{\partial n_b}{\partial \gamma} - \frac{n_b}{\gamma^2}\right] = b_3\gamma^{-(1+\alpha')}, \tag{144}$$

using the definition $n_\gamma = n_b/\gamma$. Thus the final form of the Boltzmann equation takes the form

$$(b_1\gamma^2 + b_2)\frac{\partial n_b}{\partial \gamma} - \left(b_1\gamma + \frac{b_2}{\gamma}\right)n_b = b_3\gamma^{1-\alpha'}. \tag{145}$$

Here, the index α' depends on the intrinsic blazar luminosity, and the coefficient b_2 depends on both the beam and the plasma density since

$$b_2 = \alpha\omega_p = \frac{n_b}{n_p}\sqrt{\frac{4\pi n_p e^2}{m_e}} \propto n_b n_p^{1/2} \tag{146}$$

Thus it is possible to trace the evolution of the pair spectrum once the source is defined or selected, i.e., Equation 145 can then be solved for a choice of blazar intrinstic indices, $\alpha' = 2-3$, and the solution to the Boltzmann equation then determines the final spectra. Broadly, depending on the density of the IGM plasma, and the beam Lorentz factor, there is a competition between ICS and instability losses, which modifies the cooling feature of the pair spectrum depending on the blazar luminosity.

4.2 EXPLORING MOMENTUM DIFFUSION WITH TIME DELAY MEASUREMENTS

Primary photons from TeV blazars pair produce off the EBL at an $\sim$ Mpc-scale distance from the source. The charged pairs can undergo diffusion in momentum space, or beam self-heating, as well as magnetic deflections due to the EGMF, before undergoing inverse Compton upscattering off the CMB to product secondary GeV emission [57]. The secondary photons can be detected with a time delay compared to the prompt emission from the blazars [58]. This has been proposed as a probe of the weak EGMF [59]. With time delay measurements owing to EGMF deflections through the time-dependent spectra [10], properties and structure of the magnetic field could be probed [60], [61].

Similar to this, in this work, the impact of momentum diffusion and broadening of pair beams in time delay can be explored and can be compared with the consequence of the existence of weak tangled magnetic fields. The analysis is performed, taking into account geometrical effects, and derive the delayed spectra consistently with the physical scenario.

4.2.1 *Prompt and delayed gamma-ray spectra*

Keeping in line with the previous section, the prompt spectra can be described as:

$$\frac{d^2N_\gamma}{dE_\gamma dt} = \frac{(\alpha-1)L_{\gamma,\,\mathrm{iso}}(t)}{4\pi D_L^2 E_{\gamma,pk}^2}\left(\frac{E_\gamma}{E_{\gamma,pk}}\right)^{-\alpha}, \quad (E_{\gamma,pk} < E_\gamma < E_{cut}) \tag{147}$$

where $L_{\gamma,\,\mathrm{iso}}(t)$ is the isotropic gamma-ray luminosity, D_L is the corresponding luminosity distance, $E_{\gamma,pk} = E_0$ is the spectral peak energy, and E_{cut} is the maximum cutoff energy. The luminosity distance can be expressed as

$$D_L(z) = \frac{(1+z)}{H_0} \int_0^z dz' \left[\Omega_r \left(1+z'\right)^4 + \Omega_m \left(1+z'\right)^3 + \Omega_\Lambda\right]^{-1/2}, \tag{148}$$

where Ω_r, Ω_m, and Ω_Λ are energy densities of radiation, matter, and the cosmological constant. When the prompt gamma rays with energy E_γ pair produce into electrons and positrons, such that $m_e\gamma_e = E_\gamma/2$, the corresponding $e^\pm$ flux at production can be written for the activity time of TeV blazars $t = t_{\text{blazar}}$:

$$\frac{dN_{e,0}}{d\gamma_e dt_{\text{blazar}}} = \frac{L_{\gamma,\text{ iso}}\ (t_{\text{blazar}})}{2\pi D_L^2} \frac{\alpha-1}{(2m_e)^{\alpha-1}} \frac{\gamma_e^{-\alpha}}{E_{\gamma,\text{pk}}^{2-\alpha}} \left[1-\exp\left(-\tau\left(2\gamma_e m_e\right)\right)\right]. \tag{149}$$

Thus, the delayed gamma-ray flux can be expressed as

$$\frac{d^2N_{\text{delayed}}}{dt dE_\gamma} = \int d\gamma_e \frac{dN_e}{d\gamma_e} \frac{d^2N_{IC}}{dt dE_\gamma}, \tag{150}$$

where for the charged pairs undergoing ICS on CMB, inverse Compton power for a single electron is

$$\frac{d^2N_{IC}}{dt dE_\gamma} = \frac{3\sigma_T}{4\gamma_e^2} c \int d\epsilon_{\gamma,\text{CMB}} n_{\text{CMB}} \left(\epsilon_{\gamma,\text{CMB}}\right) \frac{f(x)}{\epsilon_{\gamma,\text{CMB}}} \tag{151}$$

with the function as described in [62] as

$$f(x) = 2x \ln x + x + 1 - 2x^2 \tag{152}$$

where

$$x = \frac{E_\gamma}{4\gamma_e^2 \epsilon_{\text{CMB}}}, \tag{153}$$

and the number density of CMB photons n_{CMB} depends on the CMB energy density $\epsilon_{\gamma,\text{CMB}}$. The total time-integrated electron-positron flux relevant to delayed emission can thus be written as [63]:

$$dN_e/d\gamma_e = \left(t_{IC}/\Delta t_B\right) dN_{e,0}/d\gamma_e. \tag{154}$$

However, this picture does not completely capture the geometry of the delayed emission. In order to properly model this, deflections or momentum diffusion can be considered as a random walk in angular space, such that the probability of an electron found at an angle θ' while it was emitted at an angle θ is [4]:

$$P(\theta, \theta') = \frac{1}{\sqrt{2\pi} \sin\theta'} \frac{2}{\sqrt{2\pi}\sigma(\theta)} \exp\left(-\frac{(\theta' - \langle\theta\rangle)^2}{2\sigma^2(\theta)}\right) \tag{155}$$

which is normalised to $\int P d\Omega' = 1$. A sketch of the geometry of the delayed emission is shown in Fig. 20

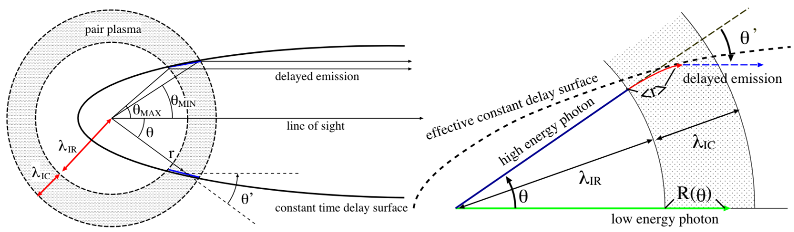

Figure 20: Geometry of delayed emission as shown in schematic from [4]

The variance $\sigma(\theta)$ and expectation value $\langle\theta\rangle$ describe the extent of broadening and are dependent on beam parameters. Thus,

$$\begin{aligned} \frac{dN_e}{d\gamma_e} &= \int dt_{blazar} \int_{\theta_{min}(t_{obs}, t_{blazar})}^{\theta_{max}(t_{obs}, t_{blazar})} d\theta \int d\Omega' \delta(\theta - \theta') P(\theta', \theta) \frac{dN_{e,0}}{d\gamma_e dt_{blazar}} \\ &= \int dt_{blazar} \int_{\theta_{min}(t_{obs}, t_{blazar})}^{\theta_{max}(t_{obs}, t_{blazar})} d\theta \frac{2}{\sqrt{2\pi}\sigma(\theta)} \exp\left(-\frac{(\theta - \langle\theta\rangle)^2}{2\sigma^2(\theta)}\right) \frac{dN_{e,0}}{d\gamma_e dt_{blazar}}. \end{aligned} \tag{156}$$

Using $c = d\langle r\rangle/dt_{obs}$, $\langle r\rangle$ being the distance between the pair production and time of observation t_{obs}, the delayed emission can be described as

$$\frac{d^2N_{delayed}}{dt_{obs} dE_\gamma} = \int d\gamma_e \frac{dN_e}{d\gamma_e} \frac{3\sigma_T}{4\gamma_e^2} \frac{d\langle r\rangle}{dt_{obs}} \int d\epsilon_{\gamma,CMB} n_{CMB}(\epsilon_{\gamma,CMB}) \frac{f(x)}{\epsilon_{\gamma,CMB}}. \tag{157}$$

4.2.2 *Impact of various processes on delayed spectra*

The rectilinear distance $d\langle r\rangle/dt_{obs}$ can be written in terms of the emission angle θ, redshift z, and an angular broadening parameter Θ,

$$\frac{d\langle r\rangle}{dt_{obs}} = \frac{2c}{(1+z)[\theta^2 + \Theta^2/3]}, \tag{158}$$

such that

$$\Theta^2 \equiv \left\langle \theta_B^2(\theta) \right\rangle + \left\langle \theta_D^2(\theta) \right\rangle + \left\langle \theta_{IC}^2(\theta) \right\rangle, \tag{159}$$

where $\left\langle \theta_B^2(\theta) \right\rangle$ represents variance in angle due to magnetic deflection, $\left\langle \theta_D^2(\theta) \right\rangle$ is the angular broadening due to momentum diffusion, while $\left\langle \theta_{ICS}^2(\theta) \right\rangle$ represents angular broadening due to ICS. If the distance the charged pairs would have otherwise travelled in absence of broadening is $R(\theta)$, we can write [64],

$$R - \langle r \rangle = \frac{\tau_B}{12} R \left\langle \phi_B^2 \right\rangle + \frac{\tau_D}{12} R \left\langle \phi_D^2 \right\rangle + \frac{\tau_{ICS}}{12} R \left\langle \phi_{ICS}^2 \right\rangle, \tag{160}$$

where ϕ_B and τ_B are respectively the deflection angle and "optical depth" associated with magnetic deflection such that

$$\phi_B \approx \frac{r_c}{r_L}, \quad \tau_B \approx \frac{R}{r_c}. \tag{161}$$

Here r_c is the coherence length of the magnetic field, and r_L is the Larmor radius. Similarly, for ICS, the corresponding quantities are:

$$\phi_{ICS} \approx \frac{1}{\gamma}, \tau_{ICS} \approx \frac{R}{\ell_{ICS}}, \tag{162}$$

where inverse Compton mean free path can be written as:

$$\ell_{ICS} = \frac{1}{\sigma_T n_{CMB}} \approx 10 \text{ kpc } (1+z)^{-3}. \tag{163}$$

4.2.3 *Comparison of ICS and momentum diffusion*

We now proceed to compute the following quantities for momentum diffusion. The "optical depth" as

$$\tau_D \approx \frac{R}{\ell_D}, \tag{164}$$

where the diffusion lengthscale ℓ_D depends upon the beam-plasma density contrast, the IGM plasma frequency and temperature and the Lorentz factor of the pairs [22]:

$$\ell_D = \Lambda \frac{c}{\omega_p} \frac{1}{\alpha} \left(\frac{k_B T}{m_c c^2} \right) \gamma \theta_0^2. \tag{165}$$

Here $\Lambda = 1 - 10$ for standard plasma conditions and $\theta_0 \approx 1/\gamma$ is the initial beam opening angle. We note that correspondingly,

$$\phi_D = \frac{\Delta p_\perp}{p_\parallel}, \tag{166}$$

where momentum in the forward direction is $p_\parallel = \gamma m_e c$ and momentum spread in the direction perpendicular to propagation can be expressed in terms of the diffusion coefficient in the perpendicular direction:

$$\Delta p_\perp = \sqrt{4D_\perp t_{\rm inst}}, \tag{167}$$

active over the instability timescale, estimated as inverse of the instability growth rate,

$$t_{\rm inst} = \frac{\Lambda}{\Gamma_{\rm inst}} \approx \frac{\Lambda\gamma}{\alpha\omega_p}. \tag{168}$$

The momentum diffusion characterised by the diffusion coefficient can be estimated as

$$D_\perp = \pi e^2 n_b \left(\frac{k_B T}{m_e c^2}\right) J_\perp, \tag{169}$$

where $J_\perp \sim 10/\omega_p$. Assembling everything, it can then be shown that,

$$\sqrt{\langle\theta_D^2\rangle} = \phi_D\sqrt{\tau_D} \approx \sqrt{R}\frac{\sqrt{n_b}}{m_e c}. \tag{170}$$

This is then compared with the angular broadening due to ICS and note that for typical astrophysical parameters, such as $n_b = 10^{-22}\text{cm}^{-3}$ and $\gamma = 10^6$,

$$\frac{\sqrt{\langle\theta_D^2\rangle}}{\sqrt{\langle\theta_{\rm ICS}^2\rangle}} \approx \mathcal{O}(10^{-5}), \tag{171}$$

which leads to the conclusion that the effect of momentum diffusion is negligible compared to ICS and does not significantly alter $d\langle r\rangle/dt_{\rm obs}$, and thus time delay observations.

4.2.4 *Comparison with deflection owing to weak tangled magnetic fields*

For weak tangled magnetic fields, one can consider a typical set of following parameters, such as the EGMF field strength $B = 10^{-16}$G and $r_c = 10^{-4}$Mpc. Thus, approximately,

$$\sqrt{\langle \theta_B^2(\theta) \rangle} = \frac{r_c}{r_L}\sqrt{\frac{R}{r_c}} = \sqrt{R}\frac{\sqrt{r_c}}{r_L}. \tag{172}$$

Consequently, we find

$$\frac{\sqrt{\langle \theta^2_{B,\text{tangled}} \rangle}}{\sqrt{\langle \theta^2_{ICS} \rangle}} \approx \mathcal{O}(10^2) \tag{173}$$

From the above analysis, we conclude that while the deflection owing to EGMF , even for weak tangled fields, could be comparable to the ICS broadening, and thus could leave an observable imprint on the delayed spectra for the secondary cascades. From eqs. 171 and 173, we get

$$\frac{\sqrt{\langle \theta^2_{D} \rangle}}{\sqrt{\langle \theta^2_{B,\text{tangled}} \rangle}} \approx \mathcal{O}(10^{-7}) \tag{174}$$

Therefore, the impact of angular broadening owing to instability-induced momentum diffusion is very small compared to magnetic and ICS scatter in an astrophysical pair beam, and thus cannot be disentangled from them through gamma-ray observations of time delay. However, energetic broadening of the astrophysical pair beam, owing to inhomogeneities in the IGM [46] or weak tangled EGMF [31], can backreact and lead to a further quenching of the instabilities.

Part II

THE DARK UNIVERSE: DARK HALOS IN A BLAZAR-HEATED UNIVERSE AND LABORATORY PROBES OF DARK MATTER

In this part, after a brief introduction to axions as dark matter and delving into the linear theory for structure formation, I show how the predictions of ultralight axions fare alongside impact of a blazar-heated late universe on structure formation. In a subsequent chapter, I return to a laboratory probe of dark matter, in particular axion-like particles in our Galaxy.

5 AXIONS AS DARK MATTER

5.1 DARK MATTER

According to the cosmological concordance model, the universe consists of four major components, of which dark energy is the takes up most of the energy budget, at $68 \pm 1\%$, followed by dark matter at $27 \pm 1\%$, and the remaining energy density can be attributed to ordinary matter and radiation [65]. While there are several particle candidates of dark matter [66], which could be warm (relativistic), or cold (nonrelativistic), there also exist non-particle dark matter candidates such as primordial black holes which could comprise dark matter in part or in its entirety [67].

5.1.1 *Cold Dark Matter*

Warm dark matter candidates such as neutrinos can suppress structure formation below their free-streaming length [68], and often are riddled with the problem that they cannot account for the energy density of dark matter completely [69], [70], [71]. In contrast, structures are not washed out by the velocity dispersion of cold dark matter, consistent with the features of structure formation across various periods in cosmic history.

5.1.2 *Axions*

Axions, which arises in quantum chromodynamics (QCD) as a pseudo-Goldstone boson Peccei-Quinn (PQ) symmetry breaking, invoked to solve the strong CP problem [72], are considered a promising dark matter candidate. They contribute to the energy density of the universe as a stable state with masses at or below the electronVolt (eV) scale. Stronger constraints on the axion mass are derived from its production mechanism in the early universe, in particular, whether inflation occurs before the phase transitions associated with the breaking of the PQ symmetry and topological defects leading to misalignment, which sets the axion mass to $m_a \sim 10^{-6}$ eV. For QCD axions, the relationship between their mass and electromagnetic coupling is defined by the following phenomenoogical relation [73] [74]:

$$m_a = 6 \times 10^{-6}\text{eV}\left(\frac{10^{12}\text{GeV}}{f_a}\right). \tag{175}$$

Axions can interact with photons as described by the interaction term

$$\mathcal{L}_{a\gamma\gamma} = -\frac{1}{4} g_{a\gamma\gamma} a F_{\mu\nu} \tilde{F}_{\mu\nu} \tag{176}$$

where $g_{a\gamma\gamma}$ stands for the coupling constant, a the axion field, and m_a the axion mass. f_a is a parameter known as the axion decay constant, which acts as a measure of the stability of QCD axions. $F_{\mu\nu}$ and $\tilde{F}_{\mu\nu}$ respectively represent the electromagnetic field tensor and its dual. Equation 176 can be written in terms of the electric and magnetic fields, $\vec{E}(x)$ and $\vec{B}(x)$, respectively.

$$\mathcal{L}_{a\gamma\gamma} = -g_{a\gamma\gamma} \frac{\alpha}{\pi} \frac{1}{f_a} a(x) \vec{E}(x) \cdot \vec{B}(x), \tag{177}$$

Axion-like particles (ALPs) have been proposed within many extensions beyond the Standard Model (BSM) in particle physics and string compactification scenarios. There have been several prescriptions for QCD axions, of which the three most commonly used formalisms include the Peccei-Quinn-Wilczek-Weinberg (PQWW) [75] [76] [77], Kim-Shifman-Vainshtein-Zakharov (KSVZ) [78] [79], and Dine-Fischler-Srednicki-Zhitnitsky (DFSZ) framework [80] [81]. From a phenomenological perspective, ALPs are not limited by the phenomenological relationship between their mass and decay constant within the mass range similar to that of QCD axions.

$$m_{a,\mathrm{QCD}} \approx 6 \times 10^{-6} \mathrm{eV} \left(\frac{10^{12} \mathrm{GeV}}{f_a / \mathcal{C}} \right). \tag{178}$$

For large decay constant f_a, the axion is light and stable, which makes it a dark matter candidate of interest.

In addition, there are ultralight species ($\sim 10^{-22}$ eV) that are motivated by certain extensions of heterotic String theoretical frameworks, also known as wave dark matter (WDM) [82], which modifies structure formation in the small-scale.

5.1.3 *Production mechanisms in the early universe*

Axions can be produced in the early universe through a variety of mechanisms. Some of the well-known mechanisms include the misalignment mechanism, which is associated with coherent displacement of the axion field [83] [84]. For axion masses specifically of the order of $m_a \sim 10^{-22}$eV [82], the axion field behaves as a classical wave on scales comparable to their de Broglie wavelength and acts as cold collisionless dark matter at scales larger than their coherence length. Topological defects related to the PQ field can lead to the production of axions via decay [85]. Decay of heavy particles (e.g., moduli) can result in relativistic axion species, in particular, when the axion field is considerably lighter than the parent species. Axions can be thermally produced when the coupling of the axion to the SM is large. Such thermally produced relativistic axions behave as a hot dark matter candidate and are subject to constraints ($m_a < 0.53 - 0.62$ eV) similar to those applicable to other standard hot dark matter candidates, e.g., massive neutrinos [86] [87] [88]. Relativistic axions can comprise the cosmic axion background (CAB) on which standard cosmic microwave background (CMB) and Big Bang nucleosynthesis (BBN) constraints are applicable to the effective number of neutrinos derived considering a CAB [89], [90].

5.1.4 *Cosmological implications*

The periodic nature of the axion potential, the local maxima of which are protected by shift symmetry from perturbative effects, can contribute to the cosmological constant thus serving as candidate models for dark energy [91], and with a sufficient number of e-foldings obtained by placing the axion field at the top of the potential, natural inflationary models [92], e.g., $V(\phi) \propto \cos(\phi/f_a)$, could be realized.

Since the axion equation of state has a pressure term associated with an oscillation frequency of $2m_a$, metric potentials also experience oscillations. This leads to a scalar strain detectable as gravitational wave events and in pulsar timing arrays [93].

A separate set of constraints on axion mass and decay constant can be drawn from the context of formation of a gravitational atom composed of bosons arising out of vacuum fluctuations around black holes, leading to a scenario with black hole spin-down, known as black hole superradiance, in which spin is extracted from the black hole and the boson mass (axion mass) creates a barrier. This, in turn, rules out parts of the mass-spin plane. Based on the black hole mass and spin distribution estimates, the gravitational wave signatures of superradiance detectable at LISA and LIGO-Virgo can be used to probe different classes of axions [94] [95] [96].

5.2 DETECTION PROSPECTS

Axions could be indirectly probed using a plethora of constraints from astrophysical observations as well as dedicated experiments [97]. These detection techniques usually rely on one or more of the following processes: axion production, axion decay, and conversion of axions into SM states. Further constraints can be derived from spin-dependent axion-mediated forces in experiments such as the proposed ARIADNE that employs nuclear magnetic resonance, probes of the coupling of axions with nucleons through spin precession in an electric field, and measurement of neutron electric dipole moment arising in presence of electric and magnetic field. A number of constraints derived to date on the axion parameter space are demonstrated in Fig. 21.

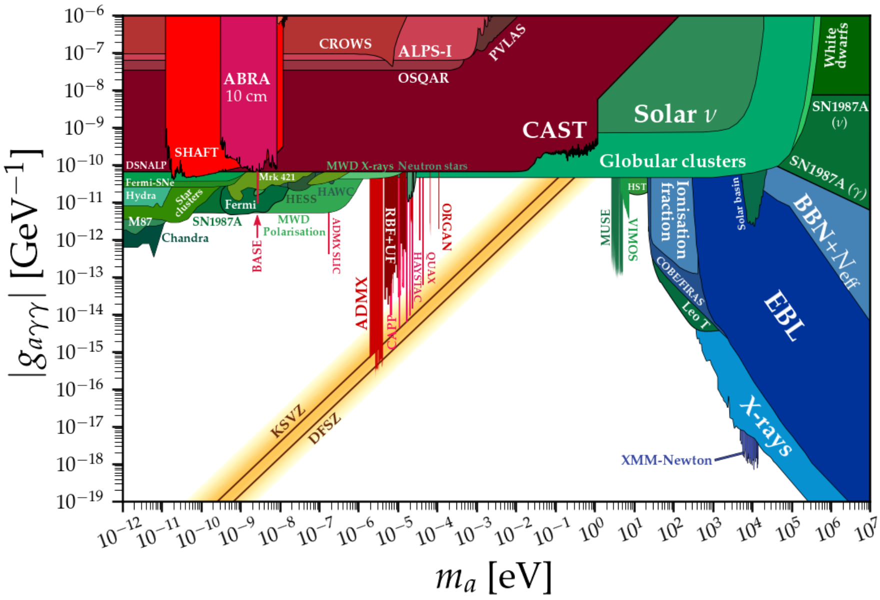

Figure 21: Current limits on the axion parameter space obtained using various publicly available datasets and constraints, where axion-photon coupling is plotted against axion mass. Courtesy: GitHub repository, Ciaran O' Hare

5.2.1 *Axion production*

Stellar astrophysics: Stellar cooling from the emission of axions produced from SM states inside stars impacts stellar evolution, resulting in constraints on the axion-photon coupling $g_{a\gamma\gamma} < 6.6 \times 10^{-11}\text{GeV}^{-1}$ from horizontal branch stars and red giant stars [98] [99] [100]. Axion-electron coupling can be also be constrained from the observed additional cooling in white dwarfs.

Light shining through a wall: In a laboratory setting, a laser beam is shot into a barrier, where photons in the beam are expected to convert to axions in the presence of strong magnetic field. The barrier is ordinarily opaque to photons; however, after crossing of the barrier, axions are converted back to photons by the application of magnetic field, thus virtually allowing photons to cross the so-called "wall,". This is the principle behind the ALPS experiment which has a target constraint of $g_{a\gamma\gamma} \sim 2 \times 10^{-11}\text{GeV}^{-1}$ [101], [102], currently upgraded to ALPS-II.

X-ray observations: Photons may convert to axion in galactic clusters owing to cluster magnetic field. This modifies the spectrum of the observed X-ray photons [103],. A limit on the axion-photon coupling is obtained as $g_{a\gamma\gamma} \leqslant 10^{-12}\text{GeV}^{-1}$ from the non-observation of such effect in X-ray probes, e.g., Chandra [104].

CMB spectral distortions: Photon can convert to axions in the presence of EGMF, leading to spectral distortions in the CMB. This places a strong constraint on the product of the axion-photon coupling and the cosmic magnetic field strength [105], [106].

5.2.2 *Axion decay*

Astrophysical probes: CMB anisotropies, spectral distortions, and BBN bounds can probe decay of axions into photons. Constraints exist from deuterium abundance [107] [108] in the regime 1 keV $\leqslant m_a \leqslant 1$ GeV and $10^{-4}\text{s} \leqslant \tau_a \leqslant 10^6\text{s}$ for axions and ALPs. For axions decaying to photons, the axion lifetime τ_a can be expressed as:

$$\tau_a = \frac{64\pi}{m_a^3 g_{a\gamma\gamma}^2} \approx 130\text{s} \left(\frac{\text{GeV}}{m_a}\right)^3 \left(\frac{10^{-12}\text{GeV}^{-1}}{g_{a\gamma\gamma}}\right)^2 \tag{179}$$

In addition, future-generation radio telescopes, e.g., SKA and HIRAX, can place limits on the axion-photon coupling through the detection of GHz photons from axion-photon conversion in the Milky Way occuring via the Primakoff process [109].

5.2.3 *Axion-photon conversion*

Haloscopes: In the presence of strong magnetic field, axions constituting halo dark matter can be converted into photons in laboratory microwave cavities [110]. This approach is adopted in a number of cavity search endeavors across the globe, the most well-known of which is ADMX [111]. In addition, a number of haloscope experiments employing other search strategies such as resonant circuits [112], dielectric antenna such as in MADMAX [113], [114], nuclear magnetic resonance in CASPEr [115], are proposed to probe this interaction. The magnetic field induced by axion-sourced current can also be detected using an LC circuit or other amplification devices, such as WISPLC [1], SHAFT [116], and ABRACADABRA [117]

Helioscopes: Solar axions can convert to axions when a strong magnetic field is applied within a telescope [**sikivie83**]. A well-known helioscope, CAST, constrains the axion-photon coupling to $g_{a\gamma\gamma} <$ 10^{-10}GeV^{-1} [118]. This limits are expected to further improve with the upcoming IAXO [119] and baby-IAXO [120] experiments.

5.3 ULTRALIGHT AXIONS

Ultralight axion-like particles or wave dark matter (WDM), owing to their small masses, have very large de Broglie wavelengths extending to galactic scale, therefore, they essentially behave like a classical field, evolving in a gravitational potential of the dark matter environment. Ultralight axions as dark matter leads to a suppression of structure in the small scale $\leqslant 10$ kpc. This can be understood from two different perspectives. The WDM condensate behaves as a fluid susceptible to the quantum pressure that prevents the formation of a sharp density peaks in the dark matter distribution. It can be thought of as, dark substructures of high density are teased out by the galactic-scale de Broglie wavelength of WDM. However, its predictions are similar to those of the ΛCDM framework in the large-scale, consistent with the observational constraints. Owing to this behaviour, WDM as dark matter can be useful reconcile with small-scale anomalies in cosmology. The dynamics of WDM is governed by the full Klein-Gordon equation [83]:

$$\phi - m_a^2 \phi = 0 \tag{180}$$

which at zeroth order of perturbation reduces to

$$\ddot{\phi}_0 + 3H\dot{\phi}_0 + m_a^2 \phi_0 = 0 \tag{181}$$

In linear perturbation theory, for overdensities $\Delta \ll 1$, the perturbed equation can be expressed as [121]:

$$\delta\phi'' + 2H\delta\phi' + \left(k^2 + m_a^2 a^2\right)\delta\phi = \left(\Psi' + 3\Phi\right)\phi' - 2m_a^2 a^2 \phi\Psi \tag{182}$$

In the following chapter, we discuss how small-scale power is suppressed for ultralight axions, how it scales with the axion mass in question, and how they compare with astrophysical solutions driven by mechanisms such as blazar heating as mentioned in Part I of this thesis.

6 IGM HEATING OWING TO INSTABILITY LOSSES

Plasma instabilities resulting from the interaction between highly energetic TeV-scale blazar-induced pair beams and the background plasma contribute to the heating of the intergalactic medium (IGM), and can be considered as a competing mechanism over inverse Compton cooling of the beam. Energy from the beam is transported into the IGM plasma via unstable electrostatic Langmuir oscillation modes. The increase in the electric field energy is then transferred to the IGM plasma leading to an elevated entropy floor and subsequently a modified temperature-density relation in the late universe. In this chapter, one can assume the simplified picture of uniform global blazar heating in the post-reionization era as the comoving number of TeV blazar sources is conserved close to present day $z \sim 0$ [15], and compute the impact of such heating in the thermal history at late times.

6.1 ENERGY LOSS FROM PAIR BEAMS THROUGH INSTABILITIES

For maximally growing modes, the electrostatic growth rate in the reactive case can be expressed as shown in 2:

$$\delta_{r,max} = \delta_r \gamma^{2/3} \tag{183}$$

As the electrostatic modes grow, the mode-dependent spectral energy density of the electric field $W(\mathbf{k})$ increases as

$$W(\mathbf{k}) = \int_0^{\tau} e^{2\delta_i(\mathbf{k})\omega_p t} dt \tag{184}$$

over one e-folding time, i.e, growth time $\mathcal{T} \sim 1/(\delta_i(\mathbf{k})\omega_p)$ with generic dimensionless mode-dependent growth rate $\delta_i(\mathbf{k})$ and plasma frequency ω_p such that in absence of nonlinear Landau damping

$$\frac{dW(\mathbf{k})}{dt} = 2\delta_i(\mathbf{k})\omega_p W(\mathbf{k}). \tag{185}$$

The above expression is applicable during the period when plasma instabilities are active or "turned on", i.e., the modes are still growing and saturation via various damping mechanisms has not set in. Summing over modes, one obtains

$$\int_{\mathbf{k}} \left[\frac{dW(\mathbf{k})}{dt}\right] d\mathbf{k} = 2\omega_p \int_{\mathbf{k}} W(\mathbf{k})\delta_i(\mathbf{k}) d\mathbf{k} \tag{186}$$

The electric field energy described in terms of the electric field E and vacuum permittivity ϵ_0 as

$$\mathcal{E} = \frac{1}{2}\epsilon_0 E^2 = \int_{\mathbf{k}} W(\mathbf{k}) d\mathbf{k}, \tag{187}$$

depends on the energy loss or cooling rate of the beam, and thus the maximum heating rate of the IGM plasma owing to plasma instabilities can be written as

$$\Gamma_{\text{plasma}} = \frac{\dot{\mathcal{E}}}{\mathcal{E}} = 2\delta_{max}\omega_p, \tag{188}$$

where δ_{max} is the dimensionless maximum growth rate. In contrast, the IGM heating rate owing to inverse Compton scattering can be written as [15]

$$\Gamma_{\text{IC}} = \frac{4\sigma_T u_{\text{CMB}}}{3m_e c}\gamma \simeq 1.4 \times 10^{-20}(1+z)^4 \gamma_b s^{-1}, \tag{189}$$

where σ_T is the Thomson cross-section, γ is the Lorentz factor of the pairs, and z is the redshift. The energy density in the CMB scales as radiation $u_{\text{CMB}} \propto (1+z)^4$. Here m_e is the electron mass.

6.2 TEMPERATURE-DENSITY RELATION

The intergalactic medium is heated by H and He photoionization, as it continues to cool adiabatically, where the adiabatic cooling depends on the local density. Overdense regions exhibit higher temperatures, as photoheating from recombination is more efficient and adiabatic cooling is slower [48]. Thus, after reionization, the temperature of the IGM is determined by the competing heating and cooling processes which act differently in the underdense and overdense regions. The thermal evolution of the IGM is best described as the phenomenological relation [122]:

$$T = T_0(\rho/\overline{\rho})^{\gamma'(z)-1}, \tag{190}$$

where T is the temperature of the IGM at a given redshift z, the temperature at present day $T_0 = 1.5 \times 10^4$K, ρ is the density at a given location, and $\overline{\rho}$ is the cosmic mean density.

If one defines the matter overdensity as $\delta = (\rho - \overline{\rho})/\overline{\rho}$, the temperature-density relation stated above can be cast as:

$$T = T_0(1+\delta)^{\gamma'(z)-1} \tag{191}$$

where γ' denotes the index of the tight power law, often characterised as the equation of state for the IGM.

6.2.1 *Blazar heating*

As delineated in [15], the estimate for IGM heating due to a single blazar can be expressed as

$$\dot{q} = \int dE \frac{\Theta(E)}{D_{pp}(E,z)} f\left(F_E, E, z\right) F_E \tag{192}$$

Here $\Theta(E)$ serves as a Heaviside step function that allows the integral to be evaluated above a certain threshold energy, e.g., 100 GeV [123].

Here the contribution of the plasma instabilities is quantified as

$$f\left(F_E, E, z\right) = 1 - f_{IC} = \frac{\Gamma_{\text{plasma}}}{\Gamma_{IC} + \Gamma_{\text{plasma}}}, \tag{193}$$

the mean free path of a TeV photon before pair production off the EBL is [15]

$$D_{pp}(E,z) = 35 \left(\frac{E}{1\text{TeV}}\right)^{-1} \left(\frac{1+z}{2}\right)^{-\zeta} \text{Mpc}, \tag{194}$$

where $\zeta = 4.5$ for $z < 1$ and $\zeta = 0$ for $z \geqslant 1$. The mean free path can be understood in terms of the crossing time for one Hubble radius as

$$\tau_H(z) = \frac{c}{D_{pp}(E,z)H(z)}, \tag{195}$$

i.e., this is the optical depth of a gamma ray of energy E associated with pair production propagating across a Hubble distance at a given redshift of z. Once again the energy spectra from blazar sources, similar to that used in 4 is assumed:

$$F_E = E\frac{dN}{dE} \propto E^{1-\alpha'} \tag{196}$$

with the gamma ray number flux defined as a simple power law with a cutoff:

$$\frac{dN}{dE} = f_0 \left(\frac{E}{E_0}\right)^{-\alpha'}. \tag{197}$$

where the parameters have their usual meanings as defined before. For a number of observed blazars, a total heating rate at present time $z = 0$ can then be constructed as

$$\dot{Q}_{\rm obs} \simeq \sum_{\rm AGN} \frac{E_0^2 f_0}{D_{pp}(E_0,0)} \int_{E_{\rm min}}^{E_{\rm max}} \frac{dE}{E_0} \left(\frac{E}{E_0}\right)^{2-\alpha} \tag{198}$$

More generally, taking into account the evolution of blazars, an average heating rate at earlier times is usually constructed from the single blazar heating rate $\dot{q}$ using the number density of blazars at a redshift z per unit logarithmic isotropic-equivalent luminosity $\log_{10} L$, spectral index α', and blazar jet opening angle Ω, $\tilde{\phi}_B(z; L, \alpha', \Omega)$ as described in [48],

$$\dot{Q} = \int dV d\log_{10} L d\alpha' d\Omega \tilde{\phi}_B(z; L, \alpha', \Omega) \frac{\Omega}{2\pi} \dot{q}. \tag{199}$$

This provides an estimate for the energy deposition rate from the beam into the IGM plasma.

6.2.2 *Thermal evolution*

The thermal evolution of the IGM at late times is governed by four components: a) cooling due to Hubble expansion, b) increase in entropy due to structure formation, c) photoionization, photoheating and various other processes dependent on redshift of evolution, and d) heating of the IGM through other mechanisms [124]. Typically the rates for photoionization can be expressed as:

$$\Gamma_{\rm photo}(z) = \int_{\nu_0}^{\infty} \frac{4\pi J(\nu, z)}{h\nu} \sigma(\nu) d\nu. \tag{200}$$

Similarly, for photoheating the following rate is applicable [125]:

$$\mathcal{H}(z) = \int_{\nu_0}^{\infty} \frac{4\pi J(\nu, z)}{h\nu} (h\nu - h\nu_0)\, \sigma(\nu) d\nu. \tag{201}$$

Here, ν_0 is the threshold frequency and $\sigma(\nu)$ is the photoionization cross-section, respectively. The redshift- and frequency-dependent UV background $J(\nu, z)$ has index α_{bk}:

$$J(\nu) = (\nu/\nu_0)^{\alpha_{\rm bk}}. \tag{202}$$

For normalization in the rates for gas (H and He), the rates are typically computed for a background index $\alpha_{bk} = 0$ until the cutoff in the spectrum at 4 Ry [125]. The photoheating rates are based on photoionization equilibrium reached after reionization.

Picking up the various pieces of the thermal history, one can express the IGM temperature as a function of redshift and therefore time as [124]:

$$\frac{dT}{dt} = -2HT + \frac{2T}{3\Delta}\frac{d\Delta}{dt} + \frac{2}{3k_B n_{bary}}\frac{dQ}{dt} \tag{203}$$

where the first term on the RHS denotes Hubble cooling due to the expansion of the universe. Overdensity is represented by Δ and n_{bary} is the baryon number density. The blazar heating term is expressed as $\dot{Q}_B$, and all other standard heating and cooling processes are expressed in units of 3860 K per free particle per Gyr, which add to the third term in the RHS as Σ_{std} in the following manner [126]:

$$\dot{Q} = \dot{Q}_B + \frac{3k_B n_b}{2}\Sigma_{std}\dot{\mathcal{Q}} \tag{204}$$

$$\begin{aligned}\Sigma_{std}\dot{\mathcal{Q}} = {} & \dot{\mathcal{Q}}_{H-I,photo} + \dot{\mathcal{Q}}_{He-I,photo} \\ & + \dot{\mathcal{Q}}_{He-II,photo} + \dot{\mathcal{Q}}_{H-II,rec} + \dot{\mathcal{Q}}_{He-III,rec} \\ & + \dot{\mathcal{Q}}_{Compton} + \dot{\mathcal{Q}}_{free-free}\end{aligned} \tag{205}$$

where

$$\dot{\mathcal{Q}}_{H-I,photo} = \frac{T_4^{-0.7} Z_3^3 \Delta}{1 + \alpha_{bk}/2}, \tag{206}$$

$$\dot{\mathcal{Q}}_{He-I,photo} = 0.13\frac{T_4^{-0.7} Z_3^3 \Delta}{1 + f(\alpha_{bk})}, \tag{207}$$

$$\dot{\mathcal{Q}}_{He-II,photo} = 2.0\frac{T_4^{-0.7} Z_3^3 \Delta}{1 + \alpha_{bk}/2}, \tag{208}$$

$$\dot{\mathcal{Q}}_{H-II,rec} = -0.11 T_4^{0.2} Z_3^3 \Delta, \tag{209}$$

$$\dot{\mathcal{Q}}_{He-III,rec} = -0.20 T_4^{0.3} Z_3^3 \Delta, \tag{210}$$

$$\dot{\mathcal{Q}}_{Compton} = -0.28 T_4 Z_3^4, \tag{211}$$

and

$$\dot{\mathcal{Q}}_{free-free} = -0.05\sqrt{T_4} Z_3^3 \Delta \tag{212}$$

where $Z_3 \equiv (1+z)/4$ and $T_4 = T/10^4$ K. The only thermal processes that are not considered are collisional processes relevant at dense regions, i.e., $\Delta \gg 10$. The Zeldovich approximation [127] can be applied such that the density of fluid elements, $\Delta = 1 + \delta_b$, traces the dark matter overdensity δ_X.

For a heating rate contribution of $\dot{Q}_B$ from blazars, a convenient parameterisation based on fit to data from [128] within 1-σ uncertainty can be expressed as [129]:

$$\begin{aligned} \log_{10}\left(\frac{\dot{Q}_B/n_{\mathrm{bary}}}{1\mathrm{eVGyr}^{-1}}\right) =& 0.0315(1+z)^3 - 0.512(1+z)^2 \\ &+ 2.27(1+z) - \log_{10}\dot{Q}_{\mathrm{mod}}. \end{aligned} \tag{213}$$

In this work, the following parameter p describes the contribution of blazar heating as $\log_{10}\dot{Q}_{\mathrm{mod}} = p = \{3-7\}$ for strong to weak blazar heating cases. For comparison, is also shown the temperature-density relation of the IGM without any blazar heating in Fig. 22. Here $\gamma \sim 1.6$ and slope of the temperature-density relation is consistent with canonical heating mechanisms described above [124] without shocks or additional heating components such as plasma instabilities.

Equation 203 is then numerically solved and the redshift dependence of γ' as of Eq. 191, the temperature-density relations for $z = 2-3$ and temperature-redshift relations for $\Delta = 10^{-2}$ to 1 (mean density) are plotted in Fig. 22 without blazar heating and in Figs. 23-26 for various degrees of heating characterised by the indices p corresponding to different modes of plasma instabilities leading to energy loss.

Fig. 22 shows good agreement with the predictions for the temperature-density relation in absence of any additional heating source past reionization [126].

In contrast, Fig. 23 shows a clear inversion of the redshift evolution of the index as well as an inverted temperature-density relation for various heating scenarios. We observe that the inversion begins to unfold from $p = 5$ onward as seen in Fig. 25. Smaller values of p indicates stronger heating. This is in good agreement with high-resolution cosmological simulation results for global blazar heating obtained using smooth particle hydrodynamic code GADGET [130], [131]. In the next section, we will observe how this alters the entropy floor which is linked to galaxy formation histories and gas cooling in clusters [132]. The numerical estimates are in agreement with Lyman-α observations evolution of the IGM temperature as presented in [133].

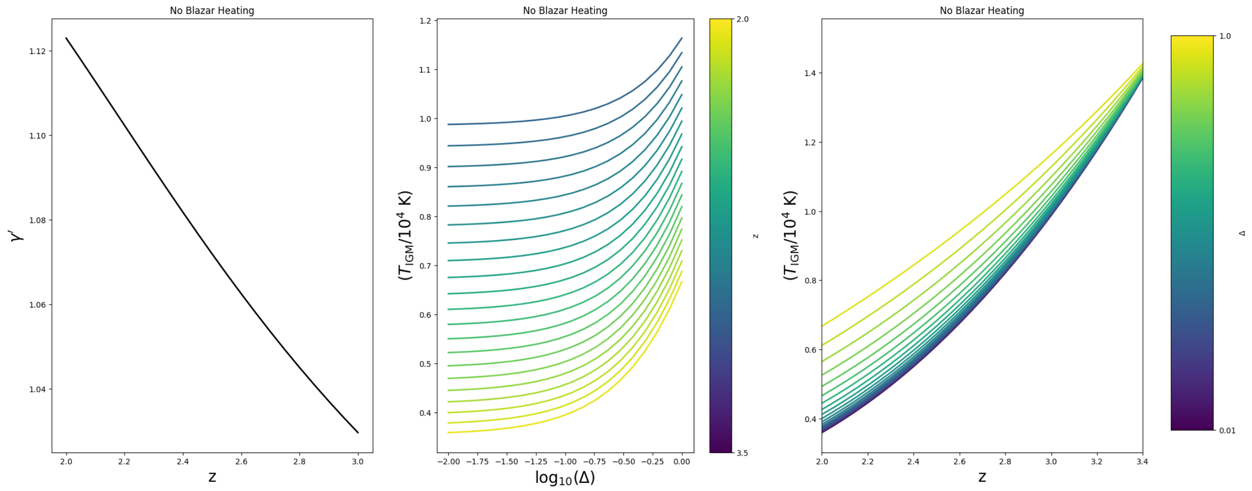

Figure 22: *Left:* Evolution of the index of the temperature-density relation with redshift. *Center:* Temperature-density relation for a number of redshifts without blazar heating. The colours of the $T - \rho$ relation span from blue to yellow with decreasing z $(3 < z < 2)$. *Right:* IGM temperature as a function of redshift z. The colours of the $T - z$ relation span from blue to yellow with increasing Δ.

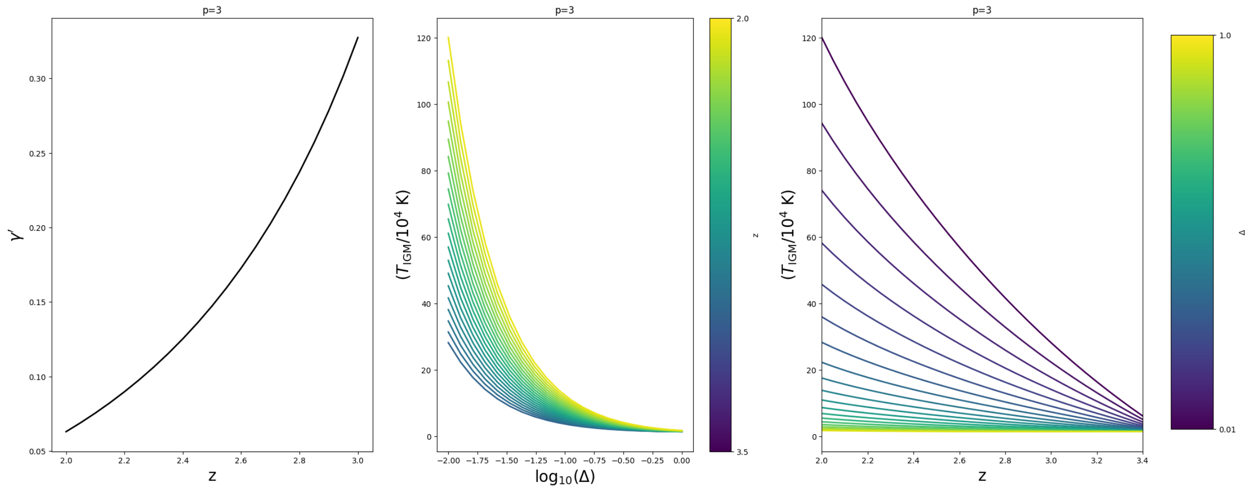

Figure 23: *Left:* Evolution of the index of the temperature-density relation with redshift. *Center:* Temperature-density relation for a number of redshifts. The colours of the $T - \rho$ relation span from blue to yellow with decreasing z $(3 < z < 2)$. $T_{\rm IGM}$ is in units of 10^4 K. *Right:* IGM temperature as a function of redshift z. The colours of the $T - z$ relation span from blue to yellow with increasing Δ. Plots are for $p = 3$.

6.2.3 *Discussion of results and cosmological repercussions*

Even though the methods applied to solve the temperature-density and entropy-density relations were semianalytic, Figs. 23-26 are in very good agreement with simulations performed using smooth-particle

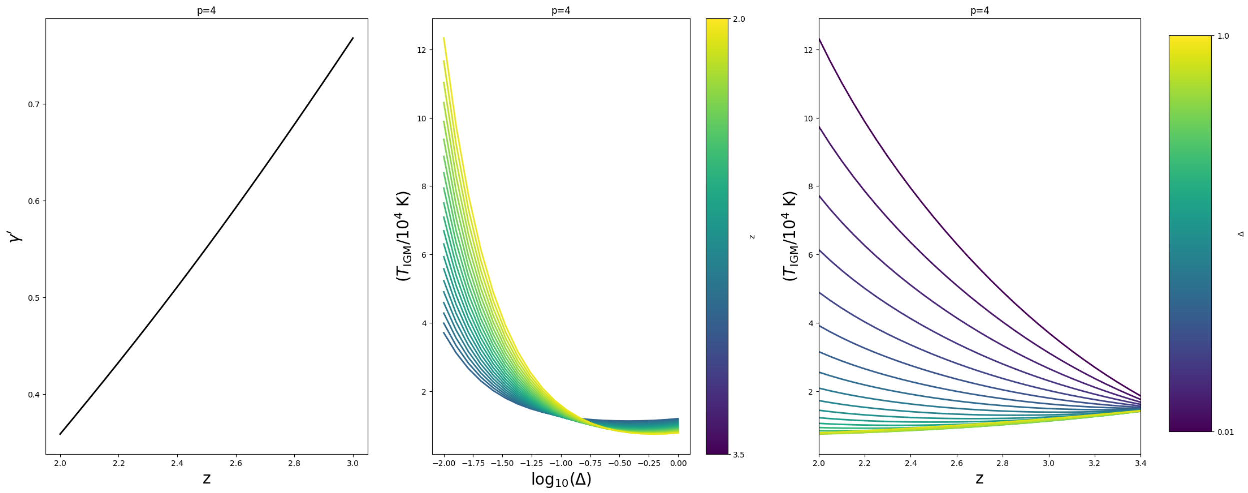

Figure 24: *Left:* Evolution of the index of the temperature-density relation with redshift. *Center:* Temperature-density relation for a number of redshifts. The colours of the $T - \rho$ relation span from blue to yellow with decreasing z ($3 < z < 2$). T_{IGM} is in units of 10^4 K. *Right:* IGM temperature as a function of redshift z. The colours of the $T - z$ relation span from blue to yellow with increasing Δ. Plots are for $p = 4$.

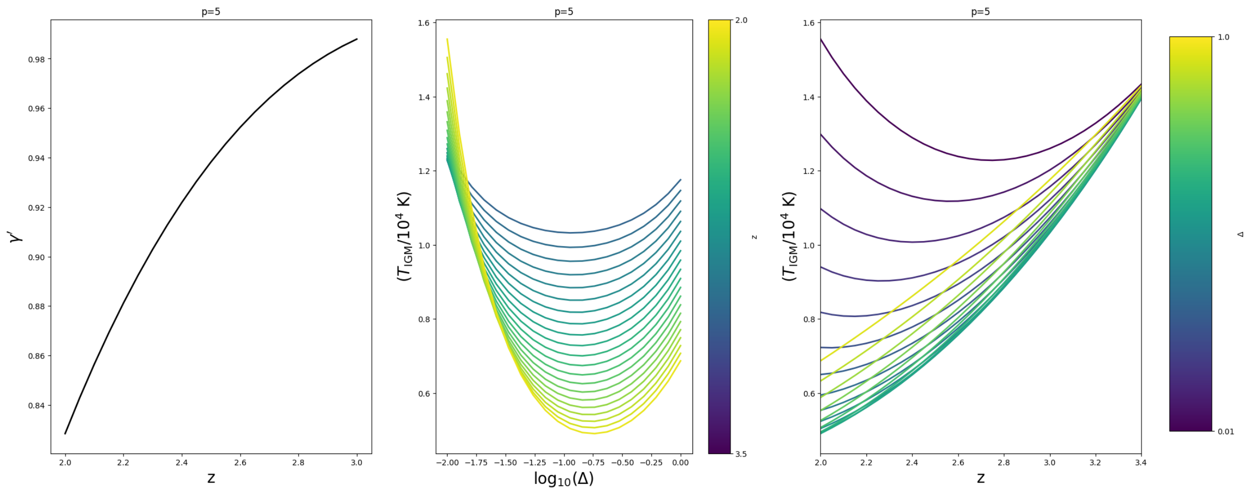

Figure 25: *Left:* Evolution of the index of the temperature-density relation with redshift. *Center:* Temperature-density relation for a number of redshifts. The colours of the $T - \rho$ relation span from blue to yellow with decreasing z ($3 < z < 2$). T_{IGM} is in units of 10^4 K. *Right:* IGM temperature as a function of redshift z. The colours of the $T - z$ relation span from blue to yellow with increasing Δ. Plots are for $p = 5$.

hydrodynamics code GADGET as shown in [129] and Lyman-α fit from [69], and more recently, [134] and [135]. In absence of blazar heating, the temperature of the late universe is expected to decrease after reionization has ended. However, when blazar heating is active,

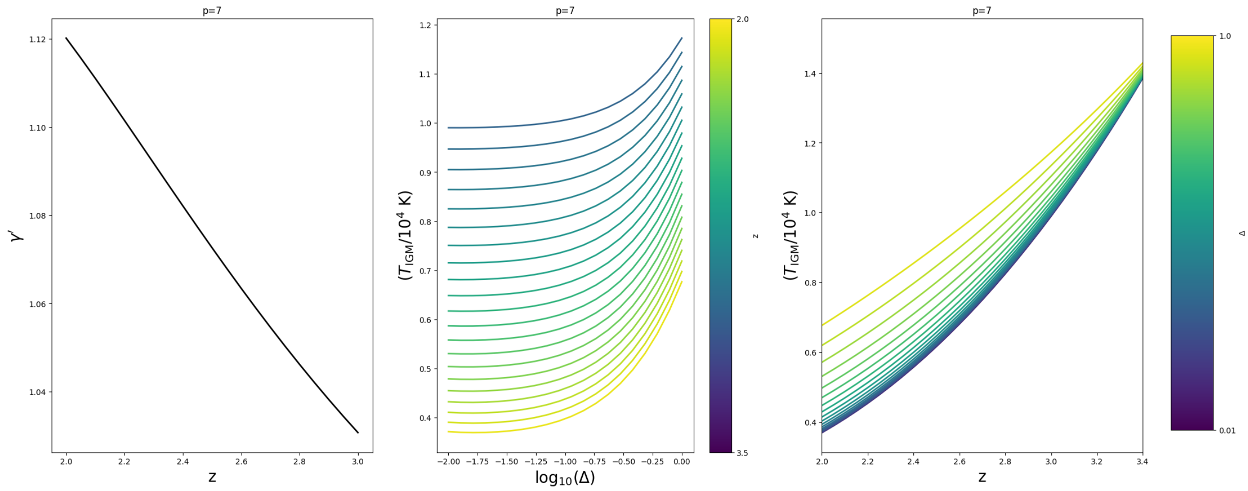

Figure 26: *Left:* Evolution of the index of the temperature-density relation with redshift. *Center:* Temperature-density relation for a number of redshifts. The colours of the $T - \rho$ relation span from blue to yellow with decreasing z ($3 < z < 2$). T_{IGM} is in units of 10^4 K. *Right:* IGM temperature as a function of redshift z. The colours of the $T - z$ relation span from blue to yellow with increasing Δ. Plots are for $p = 7$.

the temperature-density relations and entropy-density relations are inverted. The extent of heating is dependent on the degree of blazar heating assumed, characterised by the parameter p. It is to be noted that for a homogeneous heating model, the impact of the heating is most pronounced at very underdense regions. Thus, the consequences of blazar heating is expected to be severe in cosmological voids. Strong heating can raise the temperature in voids by three orders of magnitude. The numerical solution is obtained with a normalization of IGM temperature at 1.5×10^4 K at $z = 3.5$, which in this work is considered as the end of reionization.

Blazar heating is responsible for elevating the entropy floor at late times. For any sources leading to significant heating at earlier times, such as reionization, the first groups and galaxies have not formed and thus would be impacted for even a small degree of heating. However, in order for the blazar heating to impact the formation of late-forming groups and clusters, the heating rate needs to be very high. This does not exclude local effects such as shock heating. There have also been some discussion in the literature whether blazar heating can impact the bimodality of clusters in cool-core and non-cool-core [132].

The major impact of late-time blazar heating is on the formation histories of the late-forming dwarfs. The star formation histories for dwarf galaxies can be understood from their metallicity [136]. Observed dwarfs typically contain metal-poor stars, an indicator of star formation occurring at earlier times [137]. There are no specific cosmological reasons as to why dwarfs cannot form stars at late times. Instead it is sufficient to argue that dwarfs with younger stellar populations cannot form at late times, and the observed metallicity histories and dwarf luminosities [138] are then consistent with late-time blazar heating. In order to understand how this compares with the predictions of dark matter models that suppresses structure at small scales, in particular, those of warm dark matter or ultralight axions, I look into the Jeans masses of these halos and evaluate the explicit impact of blazar heating in the next part of this thesis.

7 CRITICAL HALO MASS AND IMPLICATIONS FOR DWARF GALAXIES

Despite its success in explaining the large-scale structure of the universe, observational discrepancies appear in the small scale. In warm dark matter-dominated cosmologies, structure formation is suppressed below the free-streaming scale, which determines the scale below which bound objects cannot form. Similarly, ultralight axions, also known as wave dark matter (WDM), have been proposed by [139] motivated by the apparent lack of consistencies in the predictions of cold dark matter (CDM) cosmology. Ultralight axions (WDM; $m_a \sim 10^{-22}$eV) with astrophysical-scale coherence length result in a number of interesting consequences in the small scale, in which structure formation is suppressed owing to its phenomenological similarity with warm dark matter ($m_X \sim \sqrt{m_a M_{Pl}}$, where m_X is the mass of warm dark matter and M_{Pl} is Planck mass).

7.1 SMALL-SCALE ANOMALIES

Below I outline some of the major problems with the application of cosmology in the small scale.

7.1.1 *Cusp/core problem*

In dwarf galaxies, density profiles are observed to be spherical cores as opposed to CDM-based simulations, which predicts much steeper profiles shaped like cusps. This issue, commonly known as the cusp vs. core problem, can extend beyond the small scale and in some cases observations report cored profiles in clusters [140] [141]. Even though dwarfs are dominated by dark matter, including baryonic feedback mechanisms in the simulation seems to flatten the profile; however, there are controversies regarding the role of dissipative effect of baryonic matter which may make the density profile even steeper [142]. Feedbacks from supernovae can cause an outflow of baryons that flatten the cusp but is not a reliable factor in faint galaxies where star formation is rare and infrequent [143], [144]. Warm dark matter, which is severely constrained by Lyman-α forest observations when thermal [145] [146], was initially thought to be useful in solving the cusp/core problem but the discrepancies persist [147].

7.1.2 *Missing satellites problem*

The number of observed satellites of Milky Way is several orders of magnitude smaller than the number predicted by CDM-based simulations. Dwarf galaxies with limited stellar matter and gas, are often faint due to limited star formation [148] [149] [150]. This can be due to baryonic processes such as photoionization and supernova feedback. However, sky survey experiments such as the Sloan Digital Sky Survey have detected a number of faint galaxies in the recent past [151]. This makes the understanding of this discrepancy more complicated.

7.1.3 *Too-big-to-fail problem*

According to hierarchical structure formation, the brightest satellites of Milky Way are supposed to be hosted by halos with largest velocity dispersion, which are also the largest subhalos in the Milky Way. The prediction from CDM-based simulations are of extremely massive halos with central densities so large that they cannot host the brightest observed satellites. This issue in the small-scale is known as the "too-big-to-fail" problem [152]. The massive central region of the halo indicates that the "too-big-to-fail" problem may have a common resolution with the cusp/core anomaly. Violent processes such as ram pressure and tidal stripping, or baryonic feedback from stars and supernovae are likely to play a role in smoothing the central density cusps and shaping the core in dwarf spheroidals, according to simulations. Better approximation of the density map of Milky Way sized halos can ease the situation as statistical variation in modeling of the halo mass function may have significantly altered the density profiles. The "too-big-to-fail" problem has been reported in the Local Group [153] and in the field [154] to date.

In order to understand how blazar heating affects structure in the late universe, we take a brief detour to the formalism of how inhomogeneities grow in linear regime, the concept of gravitational or Jeans instability, and pressure from baryonic gas undergoing infall into the regions where gravitational collapse has taken place.

7.2 LINEAR GROWTH OF PERTURBATION

Starting from an initial condition set in the early universe of a smooth background, small deviations from the cosmic background density originating from primordial non-Gaussianities and small velocity perturbations induced by the Hubble expansion can grow due to associated gravitational perturbations. The gravitational wells created by density perturbations start accreting matter and grow in mass. Such growth can continue unchecked in absence of a pressure force and can eventually contract and collapse to form a gravitationally bound object. In this manner, matter accreted onto the gravitational wells virialize to form stable large-scale structures such as galaxies, clusters etc. Similarly, underdense regions in the universe have matter streaming out of them over the course of the age of the universe, creating voids [155].

This early linear stage of evolution after the decoupling of matter and radiation is understood and chalked out well. Nevertheless, nonlinear features in the growth of perturbations start appearing in small-scale perturbations. This is a feature of the hierarchical structure formation [156], in which the smaller structures first go nonlinear and form cosmic objects, since the amplitudes of primordial density fluctuations are higher on smaller scales than those on larger ones. The linear theory remains very useful in understanding the evolution of the large-scale structures of the observable universe and I provide a brief overview of it as follows.

A departure from smoothness can be described in terms of the overdensity or density perturbation:

$$\delta(\mathbf{x}, t) = \frac{\rho(\mathbf{x}, t) - \overline{\rho}(t)}{\overline{\rho}(t)} \tag{214}$$

where $\rho(\mathbf{x}, t)$ describes the physical density at a given point and $\overline{\rho}(t)$ is the mean cosmic density at a given time. The Newtonian linear perturbation theory is applicable in the weak-gravity approximation to length scales smaller than the Hubble length [157], described as $c/H(t)$ and can be broken down into the following the continuity equation, Euler equation, and Poisson equation for a perfect (Newtonian) self-gravitating fluid:

$$\frac{\partial \rho}{\partial t} + \nabla \cdot (\rho \mathbf{v}) = 0 \tag{215}$$

$$\frac{\partial v}{\partial t} + (\mathbf{v} \cdot \nabla)\mathbf{v} = -\frac{1}{\rho}\nabla p - \nabla \phi \tag{216}$$

$$\nabla^2 \phi = 4\pi G \rho \tag{217}$$

Introducing small perturbations in the density ρ, velocity $\mathbf{v}$, pressure P, and gravitational potential Φ as,

$$\rho = \overline{\rho} + \delta\rho, \tag{218}$$

$$\mathbf{v} = \overline{\mathbf{v}} + \delta\mathbf{v}, \tag{219}$$

$$P = \overline{P} + \delta P, \tag{220}$$

$$\Phi = \overline{\Phi} + \delta\Phi, \tag{221}$$

describing the velocity field as a combination of the Hubble flow and peculiar velocity $\mathbf{u}$ as perturbation,

$$\mathbf{v} = H\mathbf{x} + a(t)\mathbf{u} \equiv H\mathbf{x} + \delta\mathbf{v}, \tag{222}$$

where comoving coordinates $\mathbf{r}$ is related to the physical coordinates $\mathbf{x}$ via the scale factor,

$$\mathbf{x} = a(t)\mathbf{r} \tag{223}$$

relating the pressure perturbation to the density perturbation through sound speed c_s by assuming perturbations are adiabatic in nature,

$$\delta p = c_s^2 \delta\rho, \tag{224}$$

and Fourier decomposing the overdensities

$$\delta(\mathbf{r}, t) = \sum_k \delta_k \exp(i\mathbf{k} \cdot \mathbf{r}), \tag{225}$$

such that $\mathbf{k}$ is the comoving wave number and $\mathbf{k}_{phys}$ is the physical wavenumber, one can arrive at the time evolution of the density perturbations as

$$\ddot{\delta}_k + 2H\dot{\delta}_k = \left(4\pi G\overline{\rho}(t) - \frac{k^2 c_s^2}{a^2}\right)\delta_k. \tag{226}$$

It can be readily seen from the RHS of Eq. 226, that in absence of the Hubble drag, gravity enables the perturbations to grow, while pressure prevents it [158]. Thus, perturbations either grow or end up oscillating as sound waves depending on whether the comoving wavenumber is smaller or larger than the Jeans wavenumber, i.e., $k < k_J$ implying sound wave oscillation and $k > k_J$ implying gravitational collapse where

$$k_J(a) \equiv \frac{a}{c_s(a)}\sqrt{4\pi G\bar{\rho}(a)} \tag{227}$$

which sets the corresponding Jeans length-scale $\lambda_J = 2\pi a/k_J$ and Jeans mass

$$M_J = \frac{4}{3}\pi\bar{\rho}\lambda_J^3, \tag{228}$$

where the scale factor $a \equiv 1/(1+z)$ and G is the Newton's constant of gravitation. The sound speed can be estimated as

$$c_S(a) = \left(\frac{\gamma_{gas} P}{\bar{\rho}}\right)^{1/2} = \left(\frac{\gamma_{gas} k_B T(a)}{m}\right)^{1/2} \tag{229}$$

with $T(a)$ as the time (or redshift z, or scale factor a)-dependent gas temperature, P as gas pressure, m is the mass, and k_B as Boltzmann's constant. The index of the equation of state γ_{gas} can be simplified as 5/3 for H & He. Thus

$$c_s(a) \equiv \sqrt{\frac{5kT(a)}{3\mu m_p}} \tag{230}$$

where mean molecular weight $\mu = 0.533$ such that $m = \mu m_p$, with m_p as proton mass for standard IGM conditions.

From the generic form of the Friedmann equation, Hubble rate $H = \dot{a}/a$, can be expressed in terms of the energy components of the universe as

$$\frac{H^2(a)}{H_0^2} = E^2(a) = a^{-3}\Omega_m + a^{-2}(1 - \Omega_m - \Omega_\Lambda) + \Omega_\Lambda \tag{231}$$

where subscript "0" refers to the present epoch. The average density $\bar{\rho}(a)$ is defined as

$$\bar{\rho}(a) \equiv \Omega_m(a)\rho_{cr}(a) \tag{232}$$

and the critical density evolves as

$$\rho_{cr}(a) = 3H^2(a)/(8\pi G). \tag{233}$$

In an Einstein-deSitter universe, which characterise the late-time evolution, the solution to Eq. 226 is of the form,

$$\delta_k(t) = D_+ t^{2/3} + D_- t^{-1}, \tag{234}$$

with a growing term driven by coefficient D_+ and a decaying term D_-. Equation 234 indicates that the decaying term is suppressed at late times, and the evolution of the density perturbation is governed by the growth term. However, this pictures changes at very late times, since closer to present day, Ω_Λ cannot be ignored, and the overdensity evolves in a flat dark-matter dominated universe as:

$$\delta \propto D_+(\text{const}) + D_- \exp\left(-2Ht\right), \tag{235}$$

which indicates a shutdown of growth on linear length scales [156]. However, dynamical evolution of already formed nonlinear structures, and inter-structure interaction, e.g., formation of galaxies, mergers and infall, continue to take place [157].

7.3 FILTERING SCALE AND FILTERING MASS

Returning to linear scales, which constitutes the premise of this discussion, the evolution of the mixture of baryonic and dark matter perturbations, respectively, $\delta_b(k,t)$ and $\delta_X(k,z)$, can be expressed in terms of linear theory as follow [122], [159]:

$$\begin{aligned} \frac{d^2\delta_X}{dt^2} + 2H\frac{d\delta_X}{dt} &= 4\pi G\bar{\rho}\left(f_X\delta_X + f_b\delta_b\right) \\ \frac{d^2\delta_b}{dt^2} + 2H\frac{d\delta_b}{dt} &= 4\pi G\bar{\rho}\left(f_X\delta_X + f_b\delta_b\right) - \frac{c_S^2}{a^2}k^2\delta_b \end{aligned} \tag{236}$$

While the baryonic perturbations experience both thermal and gravitational pressure, in terms of gravity, the dark matter component dominates at late times. Therefore, it is not inaccurate to set the baryon fraction as zero, $f_b = 0$ and $\delta_X \propto D+$. This leads to a solution of Eq. 236 of the form

$$\delta_X(k,t) = \delta_b(k,t)(1 + \frac{k^2}{k_J^2}) \tag{237}$$

Thus, for large k's, the DM perturbations grow as D_+, and thus the baryon-to-DM perturbation ratio can be expressed as [160],

$$\frac{\delta_b(t,k)}{\delta_X(t,k)} = 1 - \frac{A(t)}{D_+(t)}k^2 \tag{238}$$

with unknown coefficient $A(t)$ that needs to be determined case by case. If we replace δ_b accordingly in Eq. 236, $A(t)$ follows the evolution equation:

$$\frac{d^2A}{dt^2} + 2H\frac{dA}{dt} = \frac{c_S^2}{a^2}D_+(t), \tag{239}$$

the solution to which, with the initial condition of the baryon and DM perturbations being the same, i.e., $A(t=0) = dA/dt(t=0) = 0$, is

$$A(t) = \int_0^t dt' c_S^2\left(t'\right) D_+\left(t'\right) \int_{t'}^t \frac{dt''}{a^2\left(t''\right)}, \tag{240}$$

If a filtering scale k_F is introduced [159] such that

$$A(t) \equiv \frac{D_+(t)}{k_F^2(t)} \tag{241}$$

and

$$\frac{\delta_b(t,k)}{\delta_X(t,k)} = 1 - \frac{k^2}{k_F^2}, \tag{242}$$

the general expression for it reads

$$\frac{1}{k_F^2(t)} = \frac{1}{D_+(t)} \int_0^t dt' a^2\left(t'\right) \frac{\ddot{D}_+\left(t'\right) + 2H\left(t'\right)\dot{D}_+\left(t'\right)}{k_J^2\left(t'\right)} \int_{t'}^t \frac{dt''}{a^2\left(t''\right)}. \tag{243}$$

Let us note that in the high-k regime, a more accurate description of the relation between the baryonic and DM perturbations can be understood readily from Eq. 242 as [161]:

$$\delta_b = \delta_X \exp\left[-k^2/k_F^2\right]) \tag{244}$$

For blazar heating, using Eq. 236 and Eq. 227, noting that the evolution of D_+ occurs according to:

$$\ddot{D}_+(t) + 2H(t)\dot{D}_+(t) = 4\pi G\bar{\rho} D_+(t), \tag{245}$$

and transforming the integration variable from t to a, Eq. 243 can be cast as

$$\frac{1}{k_F^2(a)} = \frac{A_0}{D_+(a)} \int_0^a da' K\left(a'\right) \frac{D_+\left(a'\right)}{a'^3 E\left(a'\right)} \int_{a'}^a \frac{da''}{a''^3 E\left(a''\right)}, \tag{246}$$

with

$$A_0 = \frac{5}{3}\left(\frac{3\Omega_m}{8\pi G H_0}\right)^{2/3}. \tag{247}$$

The corresponding filtering mass is then defined as:

$$M_F(a) \equiv \frac{4\pi}{3}\bar{\rho}(a)\left(\frac{2\pi a}{k_F(a)}\right)^3 \tag{248}$$

7.3.1 *High-redshift approximation*

For relatively high redshifts after reionization, i.e., $z > 2$, in an Einstein-deSitter universe, i.e., in which we can ignore Ω_Λ, is a good approximation for matter-dominated models. Thus Eq. 246 can be cast in the simpler form [122]:

$$\frac{1}{k_F^2(a)} = \frac{3}{a}\int_{a_{min}}^{a} da' \frac{1}{k_J^2(a')}\left[1-\left(\frac{a'}{a}\right)^{1/2}\right] \tag{249}$$

The Jeans mass and filtering mass are related to the inverse Jeans and filtering scale as $M_{J,F} \propto 1/k_{J,F}^3$. After reionization, the filtering mass is smaller than the Jeans mass. This is because the filtering scale $1/k_F$ corresponds to a Jeans scale at an earlier time and thus is always smaller than $1/k_J$. In order to see this, one can apply median value theorem and rewrite Eq. 246 as:

$$\begin{aligned}\frac{1}{k_F^2(t)} =& \frac{1}{k_J^2(t_*)}\left[\frac{1}{D_+(t)}\int_0^t dt' a^2(t')\right.\\ &\left.\left(\ddot{D}_+(t') + 2H(t')\dot{D}_+(t')\right)\int_{t'}^{t}\frac{dt''}{a^2(t'')}\right]\end{aligned} \tag{250}$$

and note that when t_* is integrated from 0 to t, we get

$$k_F(t) = k_J(t_*) \tag{251}$$

for an earlier time $t_* < t$ [159].

7.3.2 *Baryonic effects and modification in structure formation*

In this section, we explore how the elevated entropy floor affect the baryonic envelope around a blazar beam and importantly, how this can impact the local DM linear power spectrum through modification of the filtering scale. The physics can be understood in terms of dynamical friction owing to gas outflows that smoothen overdensities in the dark matter substructure. The mechanism is similar in effect to other types of baryonic feedback processes which flattens cuspy dark matter halos to cores and suppresses subhalo formation. The impact of blazar heating can be explored in the clearest manner after recombination has taken place at $z = 3$ [162].

When the IGM is heated due to blazar-beam-induced energy loss through plasma instability, they are displaced. Such outflows tend to weaken the gravitational pull, leading to cold dark matter moving outwards, leading to a dip in local density around the blazars. Such suppression of power in small scales can lead to a reduction of the size of subhalos contained within a host halo, a canonical prediction of the hierarchical structure formation in a ΛCDM universe [163].

However, this treatment cannot effectively capture nonlinear effects, and modes associated with baryons undergo Silk damping [164], thus we will confine the discussion to linear theory.

From heating of the IGM plasma through instabilities induced by propagating energetic blazar beams, Jeans wave mode k_J and the filtering wave mode k_F are computed using the temperature-density relation, and are demonstrated together along with the corresponding Jeans and filtering mass together for comparison during redshifts $3 < z < 2$ in Figs. 27-30 using eqs. 250 and **??**.

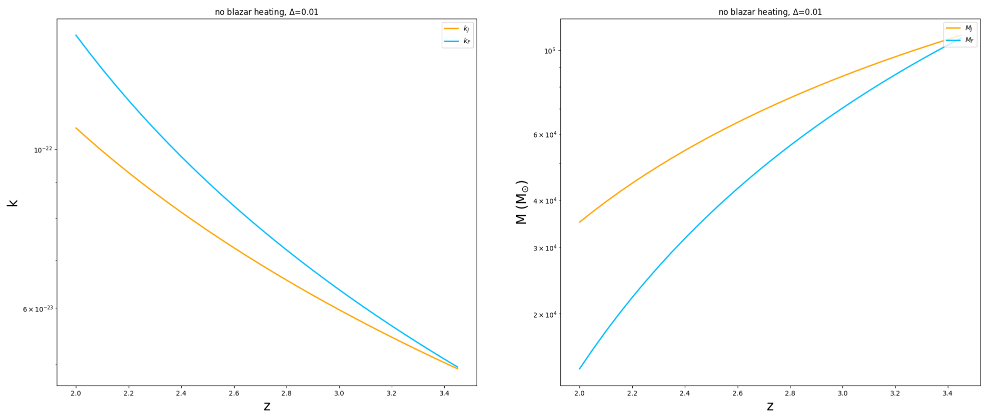

Figure 27: *left:* Jeans (orange) and filtering (blue) wave mode in units of h/Mpc, *right:* Jeans (orange) and filtering (blue) masses in units of solar mass $M_\odot$, for $\Delta = 10^{-2}$ without blazar heating.

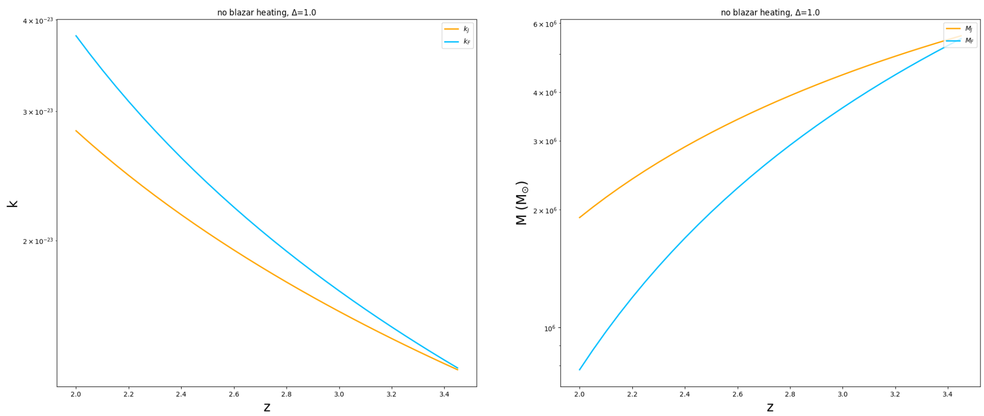

Figure 28: *left:* Jeans (orange) and filtering (blue) wave mode in units of h/Mpc, *right:* Jeans (orange) and filtering (blue) masses in units of solar mass $M_\odot$, at mean density $\Delta = 1$ without blazar heating.

For the purpose of this calculation, we only consider underdense regions since blazar heating is applicable in the low-density regions. For overdensities $\Delta \geqslant 1$, the impact of blazar heating is not as significant. The main consequences of the heating of the IGM, as seen from the contrast between the "no blazar heating" and intermediate heating characterised by $p = 4$ case, is a modification to the filtering

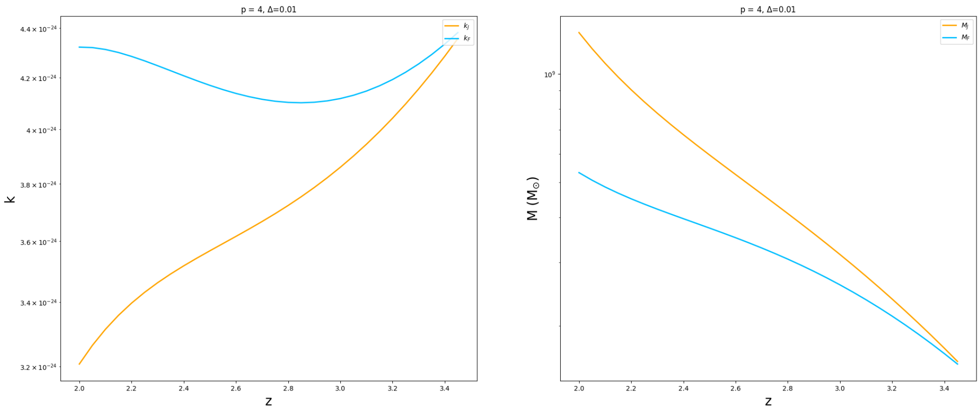

Figure 29: *left:* Jeans (orange) and filtering (blue) wave mode in units of h/Mpc, *right:* Jeans (orange) and filtering (blue) masses in units of solar mass $M_{\odot}$, for $\Delta = 10^{-2}$ and heating degree $p = 4$.

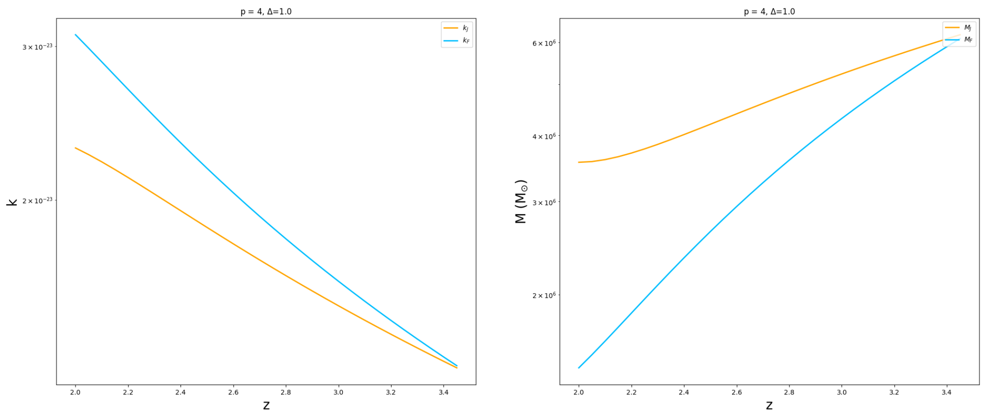

Figure 30: *left:* Jeans (orange) and filtering (blue) wave mode in units of h/Mpc, *right:* Jeans (orange) and filtering (blue) masses in units of solar mass $M_{\odot}$, at mean density $\Delta = 1$ for heating degree $p = 4$.

scale and filtering mass at late times. As can be seen from Figs. 27-30, consistent with our findings in 6, the modification of the Jeans and filtering mass owing to blazar heating is most pronounced at late times, since the activity of blazars are distinguishable during the period after reionization [165].

We note that the baryonic overdensities trace the underlying dark matter oversdensities through Eq. 244 and that the filtering and Jeans scale show the scale below which gravitational collapse cannot take place. In a blazar-heated late universe, the Jeans and filtering masses are clearly raised, via the elevated entropy floor. This acts as a cutoff scale for galaxy formation, and implies that new bound objects can no longer form below this scale, assuming that baryonic matter is embedded in dark matter-dominated halos, and the blazar heating leaves its imprint on the structure formation at late times.

With the above analysis, we see that heating of the IGM through energy loss from pair beams via plasma instabilities alter the local thermal history of the late universe. Blazar heating is local, and is most effective in underdense regions. Thus, one of the major consequence of blazar heating is the suppression of structure at late times through a purely astrophysical phenomenon. The filtering scale represents a scale below which structures cannot form due to gravitational pressure. This is in contrast with dark matter models with candidates such as wave dark matter and warm dark matter that can suppress the formation of structure through introducing oscillation below a certain scale, thus preventing the collapse of matter, or having an intrinsic free-streaming scale below which structures are washed out, based on the properties of the dark matter candidate in consideration.

7.3.3 *Comparison with WDM*

The axion field ϕ begins oscillating when the damping term driven by the Hubble parameter H is smaller than the mass term driven by axion mass m_a, and thus applying WKB approximation, one can see that, unlike cold dark matter, WDM has a scale-dependent non-zero sound speed [139], [166]:

$$c_s^2 = \frac{\frac{k^2}{4m_a^2 a^2}}{1 + \frac{k^2}{4m_a^2 a^2}} \tag{252}$$

which, in high and low k reduces respectively to

$$c_a^2 = \begin{cases} \frac{k^2}{4m_a^2 a^2} & \text{if } k \ll 2m_a a \\ 1 & \text{if } k \gg 2m_a a \end{cases} \tag{253}$$

The sound speed leads to an additional term in the evolution of the WDM overdensity

$$\delta'' + H\delta' + c_s^2 k^2 \delta - 3H\Phi' + k^2\Psi - 3\Phi'' = 0, \tag{254}$$

which introduces an axionic Jeans scale,

$$k_J = (16\pi G\bar{\rho})^{1/4} m_a^{1/2}, \tag{255}$$

above which structures formed behave as cold dark matter. In terms of the key parameters, with $\bar{\rho} = \rho_0 a^{-3}$,

$$k_J = 66.5a^{1/4} \left(\frac{\Omega_a h^2}{0.12}\right)^{1/4} \left(\frac{m_a}{10^{-22}\text{eV}}\right)^{1/2} \text{Mpc}^{-1} \tag{256}$$

Noting that WDM of very small masses are excluded via recent Lyman-α analyses [167], [168], we turn our attention to medium-mass WDM, 10^{-20} eV $< m_a < 10^{-12}$ eV. The corresponding characteristic mass scale is defined as

$$M_{\text{char}} = \frac{4}{3}\pi \left(\frac{\lambda_{char}}{2}\right)^3 \bar{\rho} \tag{257}$$

with $\lambda_{\text{char}}/2 = \pi/k$, which scales with the axion mass as $M_{\text{char}} \propto m_a^{-\chi}$ where $\chi \approx 1.35$ [83]. Therefore, for an WDM mass of $m_a \sim 10^{-16}$ eV, the corresponding characteristic mass is $M_{\text{char}} \approx 10^2 h^{-1} M_\odot$, and for an WDM mass of $m_a \sim 10^{-18}$ eV, the characteristic mass is $M_{\text{char}} \approx 10^4 h^{-1} M_\odot$, which are several orders of magnitude smaller than that in observed dwarf galaxies, and also much smaller than that allowed even in weak blazar heating scenarios corresponding to a kinetic oblique rate.

In WDM cosmology, late-forming dwarf galaxies could host relatively young stars, which is at odds with the star formation histories explored through metallicity measurements of dwarf galaxies [136], indicating that the stellar matter hosted in such objects are fairly old [137]. Thus, this strongly disfavours an WDM-dominated cosmology at late times and we conclude that formation of dwarf galaxies are suppressed at late times, indicating a consensus with findings that can alleviate the small-scale crisis.

At late times this incompatibility with a thermal history altered by blazar heating translates to a cutoff in the size of gravitationally bound structures that contains baryons. We note that the suppression of structure is strong for underdense regions. Therefore, while in a blazar-heated universe where WDM is all of dark matter, extremely small and nearly hypothetical dark objects such as minihalos, miniclusters, and axion stars can still exist, there is a restriction on the formation of objects hosting stellar matter at late times, according to observations of dwarf galaxies. With subsequent Lyman-α analysis it may be possible to exclude certain mass ranges of WDM for various degrees of blazar heating.

7.4 FUTURE DIRECTIONS

7.4.1 *Lyman alpha observations*

Most of the gas in the late universe is hydrogen. When electrons in a hydrogen atom undergoes transition from the first excited state to the ground state, photons are emitted in the Lyman-α band. Out of these photons, the ones with short wavelengths (1216 Å) can travel to us from the high-redshift universe, proving to be one of the best probes of galaxy formation and cosmic reionization through the behaviour of the hydrogen emission lines intergalactic medium at various redshifts [169]. The flux power spectrum detectable using Lyman-α observation depends on flux fluctuations, i.e., fluctuation in the transmitted flux from a source [170]. Such flux overdensity, which traces the underlying matter distribution, can be defined similarly in terms of flux F and mean flux $\langle F \rangle$ as [171],

$$\delta_F \equiv \frac{F - \langle F \rangle}{\langle F \rangle} \tag{258}$$

which depends on the optical depth owing to Ly-α absorption

$$F = e^{-\tau}. \tag{259}$$

With fitting parameter $A \propto \Omega_b^2 \Gamma_{UV}^{-1} T_0^{-0.7}$, one can write

$$F \simeq e^{-A(\rho/\bar{\rho})^{\beta}}, \tag{260}$$

and $\beta = 2.7 - 0.7\gamma'$, where γ' refers to the index in the temperature-density relation described previously. The mean flux is dependent on redshift and is tuned by the ionizing UV background from reionization Γ_{UV}^{-1} such that [172]:

$$\bar{F}(z) \simeq \begin{cases} \exp\left[-0.0032(1+z)^{3.37\pm0.2}\right] & 1.5 \leqslant z \leqslant 4 \\ 0.97 - 0.025z \pm (0.003 + 0.005z) & 0z < 1.5 \end{cases} \tag{261}$$

In order to weigh in the role of various degrees of blazar heating on structure formation against observations, in a future work, generating mock Lyman-α flux power spectrum and comparing it with Lyman-α survey data will be explored.

7.4.2 *Patchy blazar heating*

In this work, we have studied the impact of heating of the IGM by blazars via plasma instabilities leading to loss of kinetic energy in pair beams originating from them, and showed how it affects the thermal history of the universe at late times. However, the broadening of the Lyman-α lines is not pronounced at $z = 2.4$ [173] and this indicates that observed gas could be cooler than predicted by a bulk volumetric global heating by the blazars.

Since blazars are AGNs forming in high-density regions, the heating around such objects is much stronger than relatively underdense regions. Recent observations indicate that temperatures in underdense regions could be higher than predicted [174], [175], a feature that is difficult to explain invoking late HeII reionization. Thus a more sophisticated approach would be to implement a "patchy heating" recipe by implementing local heating fluctuations around a mean heating rate $\dot{Q}$ such that the total heating rate is expressed as [176]:

$$\dot{Q}(\mathbf{x}, z) = \bar{\dot{Q}}(\mathbf{x}, z)\,[1 + \delta_H(\mathbf{x}, z)] \tag{262}$$

with the heating fluctuation depending on a window function $\tilde{W}_H$

$$\tilde{\delta}_H(k, z) = \tilde{W}_H(k, z)\tilde{\delta}(k, z) \tag{263}$$

which can be described as [177]:

$$\begin{aligned}\tilde{W}_H(\hat{k}, z) = &\frac{1}{N}\int_{E_{min}}^{E_{max}} \frac{dE}{D_{pp}(E, z)} \int_z^{\infty} dz' \frac{\bar{\hat{\mathcal{E}}}_{E'}\,(z')\, e^{-\tau}}{(1+z')\,H\,(z')} \\ &\times \frac{D\,(z')}{D(z)}\left[\left(b\,(z') + \frac{f}{3}\right) j_0(\hat{k}\hat{r}) - \frac{2f}{3} j_2(\hat{k}\hat{r})\right]\end{aligned} \tag{264}$$

with D_{pp} is the pair production lengthscale. j_0 and j_2 are spherical Bessel functions of the zeroth and second kind. E represents the energy of the photon received from the blazar, E' is the initial energy of the photon, $\hat{\mathcal{E}}_E$ stands for the comoving blazar spectral luminosity density, and τ is the optical depth.

Here,

$$N = \int_{E_{min}}^{E_{max}} \frac{dE}{D_{pp}(E, z)} \int_z^{\infty} dz' \frac{\bar{\mathcal{E}}_{E'}\,(z')\, e^{-\tau}}{(1+z')\,H\,(z')} \tag{265}$$

and

$$f \equiv d\log\delta / d\log a. \tag{266}$$

The Eulerian bias b can be implemented with respect to the underlying DM halo bias, either using a quasar bias

$$b_{quasar}\,(z) = 10^{0.27z - 0.04} \tag{267}$$

or galaxy bias

$$b_{galaxy}\,(z) = 10^{0.174z}, \tag{268}$$

as reviewed in [178]. The heating fluctuations capture the underlying matter distribution on the large scales. Due to coordinate-dependence of the window function, it is only possible to explore this scenario with the aid of a cosmological simulation which I will return to in future work.

7.4.3 *Outlook*

In this work, I present the first semianalytic results parameterising various degrees of blazar heating and how they affect late time structure formation via an elevated entropy floor. The Jeans mass and filtering mass of halos are computed using the entropy-density relations, which have similar slopes across the parameter values signifying the extent of heating. Based on the analysis by [173], the column density distribution and the Ly-α linewidth do not show thermal broadening at $z = 2.4$. While at first glance, it may seem that the homogeneous heating models are not consistent with this observation, the right redshift evolution of blazars needs to be taken into account. In implementing the patchy heating model based on blazar clustering, it is worthwhile to note the distinction between galaxy bias and quasar bias and apply appropriate corrections to the blazar luminosity distribution across redshift, which can steadily diminish at higher redshift, unlike quasars [179], up until $z \sim 3.5$, which is set as the end of reionization for the purpose of this work. It is also worth noting that the analysis by [173] is sensitive to overdense regions with $\Delta \geqslant 1$. A direct comparison with Lyman-α temperature measurements at mean density is performed and limits on axion mass is drawn in my subsequent investigation [180]. Combining the power spectra based on the dark matter models that predict a suppression of structure at small scales with a cosmological simulation implementing various degrees of blazar heating in a patchy heating scenario could be useful in understanding the consistency of the models with altered late time cosmologies, which will be explored in a future work.

8 AXION DETECTION USING AN LC CIRCUIT

This chapter includes a summary of the article titled "WISPLC: the search for dark matter using an LC circuit" [1], outlining the detection prospects of axion dark matter, in particular ALPs as dark matter using LC circuit. In particular, the concept and schemes for WISPLC, a state-of-the-art tabletop axion detector which can probe axions in the mass range $10^{-12} - 10^{-6}$eV operating on broadband and tuned modes, is introduced and the sensitivity of the experiment is presented.

8.1 THEORETICAL PREMISE

In presence of axions, the inhomogeneous Maxwell's equation can be written as,

$$\nabla \cdot \mathbf{E} = g\mathbf{B} \cdot \nabla a + \rho_{el} \tag{269}$$

and

$$\nabla \times \mathbf{B} - \frac{\partial \mathbf{E}}{\partial t} = g_{a\gamma\gamma}\left(\mathbf{E} \times \nabla a - \mathbf{B}\frac{\partial a}{\partial t} \right) + \mathbf{j}_{el},, \tag{270}$$

where $\mathbf{E}$ and $\mathbf{B}$ respectively represent the electric and magnetic field, and ρ_{el} and $\mathbf{j}_{el}$ are the corresponding electromagnetic charge and current densities. Equation 270 contains the time derivative of the axion field, which depends on the average local axion density as $\langle \rho_a \rangle = \frac{1}{2}\dot{a}^2$.

The characteristic lengthscale of an neV-scale axion is $\sim \mathcal{O}(10^5\text{m})$. This is significantly larger than the physical dimension of the experiment. Therefore, for the purpose of the laboratory experiment, we can consider axions as a coherent oscillating scalar field. This allows us to ignore any spatial variation and assume homogeneity:

$$a(t) = a_0 \cos(m_a t) = \frac{\sqrt{2\rho_{DM}}}{m_a} \cos(m_a t),. \tag{271}$$

Here a_0 is the field amplitude, $\rho_{DM} \approx 0.3$ GeV/cm^3 is the local dark matter density, where we assume that $\langle \rho_a \rangle = \rho_{DM}$. Combining Eq. 270 and Eq. 271, we note that an axion-sourced current density $\mathbf{j}_a$ is induced by the external magnetic field. The density oscillates at the Compton frequency of axions $\nu_a = m_a c^2/h$, where h is Planck's constant and c is the speed of light. The induced axion current can be derived as:

$$\mathbf{j}_a(t) = -g_{a\gamma\gamma}\,\mathbf{B}\,\frac{\partial a}{\partial t} = g_{a\gamma\gamma}\sqrt{2\rho_{DM}}\sin(m_a t)\,\mathbf{B} \tag{272}$$

The current then generates an oscillating perpendicular toroidal magnetic field $\mathbf{B}_a$ satisfying

$$\nabla \times \mathbf{B}_a = \mathbf{j}_a. \tag{273}$$

This magnetic field B_a can then be amplified with the aid of an LC circuit and then the amplified field can be captured using a superconducting device, such as a SQUID magnetometer. In particular, $\vec{B}_a$ induces an alternating EMF according to Faraday's law. The EMF generates an alternating current. The tunable LC circuit amplifies it and converts it into a magnetic field through an input coil. The alternating current can then be measured by the SQUID magnetometer via inductive coupling to the input coil. This is the premise of detecting ALPs with WISPLC.

8.2 DETECTION PRINCIPLE

For the purpose of understanding how the shape of the pick up loop alters what the axion "sees", we define an effective magnetic volume incorporating the pick up loop geometry into a geometric factor.

$$\mathcal{G}_V = \frac{1}{\left|\vec{B}_{max}\right| V_{magnet}} \int_{loop} dS \int_{magnet} \frac{\vec{B}(\vec{r}) \times (\vec{r} - r')}{|\vec{r} - r'|^3} \cdot \hat{n} dV \tag{274}$$

such that

$$V_B = \mathcal{G}_V V_{magnet}\,. \tag{275}$$

This way, the magnetic flux through the pickup loop can be expressed as

$$\Phi_a(t) = g_{\alpha\gamma\gamma}\sqrt{2\rho_{DM}}\,C\sin(m_a t)\,, \tag{276}$$

where we define the form factor C as

$$C = \left|\vec{B}_{max}\right| V_B. \tag{277}$$

This provides a useful measure for comparison among various experiments in terms of the parameters related to the magnetic such as its volume V_B and the maximum field strength that can be achieved, B_{max}.

8.2.1 *Detection schemes*

For the detection of ALPs as dark matter using an LC circuit, two operating modes could be taken advantage of. For a broadband search, the magnetic flux generated owing to the axion current is transferred to the magnetometer through inductive coupling. In this mode, the flux through the pickup loop is related to the magnetic flux in the SQUID via induction:

$$\Phi_{\text{SQUID}}(t) = M_i L_{\text{sys}}^{-1} \Phi_a(t). \tag{278}$$

It is also possible to enhance the signal by a certain quality factor Q in a restricted bandwidth $\Delta\omega = \omega/Q$, where the supercurrent oscillates with a frequency of $\omega = 1/\sqrt{LC}$. This is known as the resonant approach, in which the expression for the flux through the SQUID is modified by a quality factor Q such that

$$\Phi_{\text{SQUID}}(t) = Q M_i L_{\text{sys}}^{-1} \Phi_a(t). \tag{279}$$

Here, we note that M_i stands for the mutual inductance and L_{sys} is the total inductance of the readout circuit,

$$L \simeq L_m + L_c + L_d, \tag{280}$$

where L_m, L_c, and L_d are respectively the inductances of the following elements: the pickup loop L_m, coaxial cable L_c, and the coil facing the magnetometer L_d.

8.3 WISPLC

The Weakly Interacting Slender Particle detection with LC circuit (WISPLC) experiment is a haloscope proposed to detect the induced magnetic field with a superconducting loop after it has been amplified with a LC resonant circuit. It can then be measured with a Superconducting Quantum Interference Device (SQUIDs) magnetometer. The experiment aims to detect the magnetic field generated by the induced axion current in presence of an external magnetic field as discussed in the previous section, in order to detect ultralight axions and ALPs in the local galactic halo. In addition to the basic broadband functionality operating over the entire detector bandwidth, integration of a tunable LC circuit in the readout can be implemented in order to enhance the sensitivity in narrower bandwidths.

8.3.1 *Experimental design*

The WISPLC experiment is built with a large-scale cryogen-free magnet system with warm bore of diameter of 125 mm and a length of 755

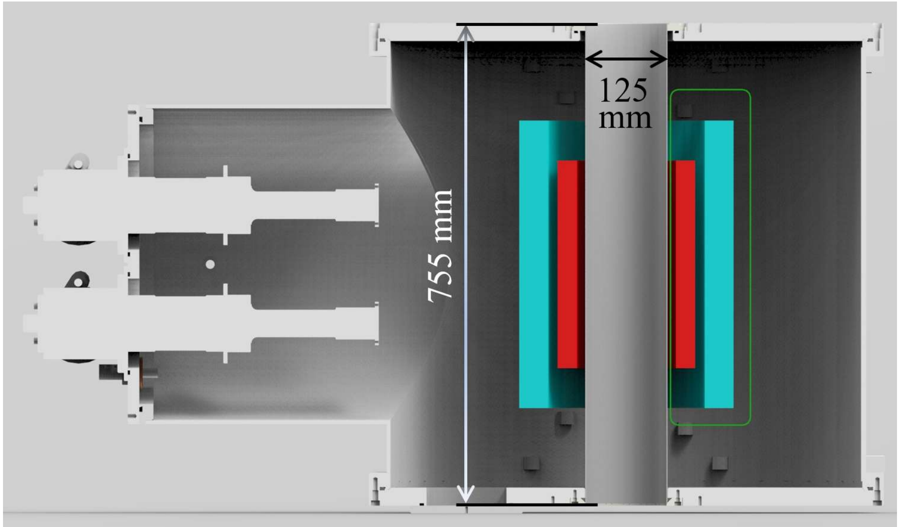

Figure 31: A schematic of the large-scale cryogen-free magnet system with a warm bore in the center is shown where the two concentric solenoidal magnets shown in blue and red can produce a maximum magnetic field of 14 T in the center. Two individually wired superconducting loops installed inside the cryostat enclose the cross-section of the magnets. They are shown in green. The figure is presented as in [1].

mm as. The setpup contains two concentric solenoids, shown in blue and red, wrapped in superconducting wire, responsible for producing magnetic field at the center of the warm bore. Two individually wired superconducting loops placed as enclosure of the magnet cross-section, are shown in green. The schematic is displayed in Fig. 31. The maximum magnetic field strength that could be reached is 14 T. We show a simple experimental scheme in Fig. 32.

8.3.2 *Experimental parameters*

Using numerical 2D finite element method, the experimental parameters for WISPLC are determined as follow: $|\vec{B}_{\max}| = 14$ T, $V_{\text{magnet}} = 0.024$ m^3, $\mathcal{G}_V = 0.074$. By comparing the form factors in Table 1, one can see the advantage of WISPLC over other experiments in its C factor being 1000 times larger than those of the contemporary experiments that employ LC-circuit based axion haloscopes, in particular ABRACADABRA (ABRA.) [117, 181–183] and SHAFT [116].

For the broadband scheme, bandwidth is restricted by the detector and readout electronics, and the transfer efficiency

$$\kappa = \Phi_{\text{SQUID}}/\Phi_a \sim 4 \times 10^{-4} \tag{281}$$

For the resonant readout, a variable LC resonant circuit is inserted between the pickup loop and SQUID. Consequently, the supercon-

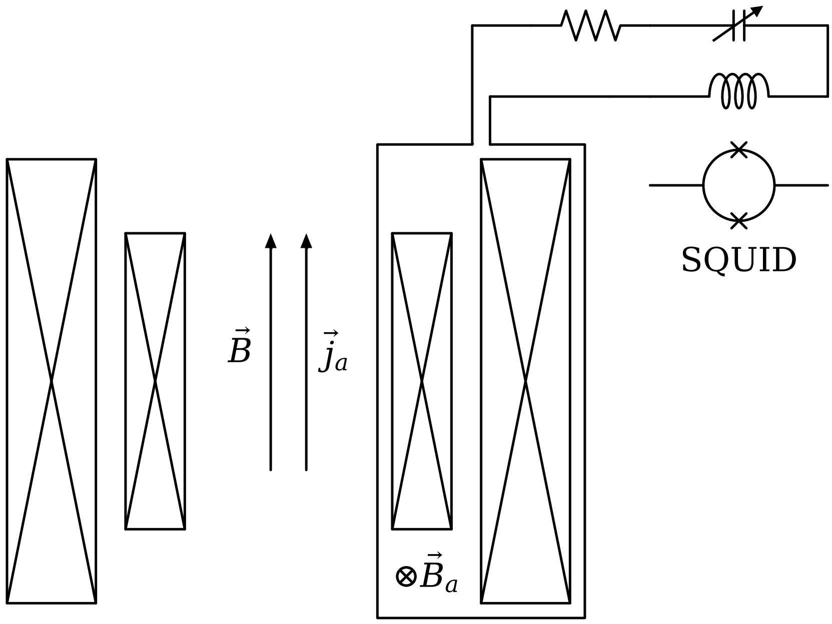

Figure 32: Schematics of the proposed experimental setup involving four rectangles with crossings displaying the windings of the two solenoid magnets. The figure is presented as in [1].

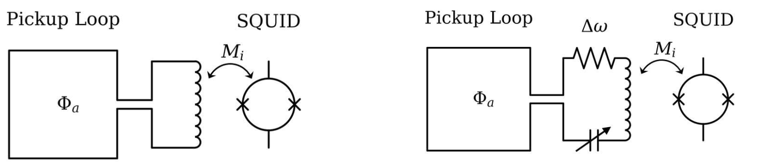

(a) Readout scheme for broadband detection

(b) Readout scheme with resonant circuit

Figure 33: Two different operating modes shown as readout schemes for broadband and resonant detection. The figure is presented as in [1].

Table 1: Comparison of experimental parameters between WISPLC, ABRA. and SHAFT, $C = |\vec{B}_{max}| V_{magnet}\, \mathcal{G}_V$.

	$\lvert\vec{B}_{max}\rvert$ (T)	$\mathcal{G}_V$	V_{magnet} (m^3)	C/C_{SHAFT}
SHAFT[1]	1.5	0.108[2]	9.5×10^{-5}	1
ABRA.[3]	1	0.027	8.9×10^{-4}	1.55
WISPLC	14	0.074	2.4×10^{-2}	1.60×10^3

ducting current is enhanced by the quality factor Q of the resonant circuit. For WISPLC, a benchmark quality factor of 10^4 is chosen.

We expect the axion signal to exhibit a a line profile with a bandwidth $\Delta\nu_a$ centered at the Compton frequency $\nu_a = \omega_a/2\pi = m_a c^2/h$ where $\Delta\nu_a = \nu_a \sigma_v^2$. The width of the line signal is determined by the inverse of the so-called axion coherence time $\tau_a \sim 1/m_a\sigma_v^2$. The dark matter velocity dispersion in the Milky Way is considered to be $\sigma_v = v/c \sim \mathcal{O}(10^{-3})$ [184].

8.4 SENSITIVITY OF THE EXPERIMENT

For neV axions, the coherence time is estimated as $\tau_a \sim 0.66\,\mathrm{s}$.

The total flux noise of a SQUID can be understood as

$$S_\Phi = S_{\Phi,SQUID} + S_{V,amp}/V_\Phi^2 + S_{I,amp} M_{dyn}^2. \tag{282}$$

Here $S_{V,amp}$ and $S_{I,amp}$ represent the current and voltage noise from amplifier, and V_Φ and M_{dyn} stand for the transfer coefficient and current sensitivity of the front end SQUID, respectively. The corresponding white noise floor is expressed in terms of the flux quanta Φ_0

$$S_\Phi^{1/2} \approx 0.9\ \mu\Phi_0/\sqrt{\mathrm{Hz}}, \tag{283}$$

where $\Phi_0 = h/(2e) \approx 2 \times 10^{-15}$ Wb is the magnetic flux quantum.

The SNR typically scales as $\sqrt{t}$:

$$\mathrm{SNR} = \frac{\Phi_{SQUID}}{S_\Phi^{1/2}} t^{1/2}, \quad t\tau_a \tag{284}$$

However, for an observation time greater than the axion coherence time τ_a, treating the axion signal as bandwidth-limited, Dicke's radiometer equation is then adopted and the corresponding expression for SNR is modified:

$$\mathrm{SNR} = \frac{\Phi_{\mathrm{SQUID}}}{S_{\Phi}^{1/2}} (t\tau_a)^{1/4}, \quad t > \tau_a \tag{285}$$

Here we present the estimated sensitivity for a 2σ detection in terms of an axion-photon coupling of

$$\begin{aligned} g_{a\gamma\gamma,2\sigma} \geqslant 8 \times 10^{-13}\,\mathrm{GeV}^{-1} \left(\frac{m_a}{10^{-9}\,\mathrm{eV}}\right)^{1/4} \left(\frac{\sigma_\nu}{10^{-3}}\right)^{1/2} \\ \left(\frac{\rho_{\mathrm{DM}}}{0.3\,\mathrm{GeV/cm^3}}\right)^{-1/2} \left(\frac{\kappa}{4 \times 10^{-4}}\, \frac{C}{0.025\,\mathrm{m^3T}}\right)^{-1} \\ \left(\frac{t}{100\ \mathrm{days}}\right)^{-1/4} \left(\frac{S_\Phi^{1/2}}{0.9\,\mu\Phi_0/\sqrt{\mathrm{Hz}}}\right) \end{aligned} \tag{286}$$

Scanning between 10^{-11} eV and 2.5×10^{-8} eV is planned for resonant detection. With a 1-min interval for the tuning of the LC circuit, the integration time can be set as $t_{\mathrm{Res}} \approx 1$ min for each frequency scan. We show the total enhancement on the SNR compared to the broadband detection for $m_a \geqslant 10^{-11}$ eV as:

$$Q_{\mathrm{Res}} \approx Q \left(\frac{t_{\mathrm{Res}}}{t_{\mathrm{BB}}}\right)^{1/4} \approx 515 \tag{287}$$

The 2σ exclusion limit is shown in Figure 34 for all resonant bands, owing to an improved flux transfer efficiency similar to the light-shaded blue area.

8.5 DISCUSSION AND SUMMARY

The sensitivity for the detection of axions with mass and coupling in the blue area at 2σ with WISPLC after an integration time of $t_{\mathrm{BB}} = 100$ days is demonstrated in Fig. 34. For comparison are shown two newly proposed frameworks that extend the QCD axion landscape, photophilic axions [185] and trapped misalignment [186]), which are shown in dark grey lines and light-shaded grey area, respectively. The sensitivity can be improved with a scaled coupling of $\kappa = 2 \times 10^{-3}$, which is shown in light-shaded blue which reaches the parameter space for the dark matter models mentioned above. The light-shaded orange area shows the enhanced sensitivity owing to the resonant scheme operating from 10^{-11} eV to 2.5×10^{-8} eV. This shows an enhancement in sensitivity corresponding to nearly three orders of magnitude in axion-photon coupling. At present, the experiment is fully funded, is in assembly, and will start taking data in a few months.

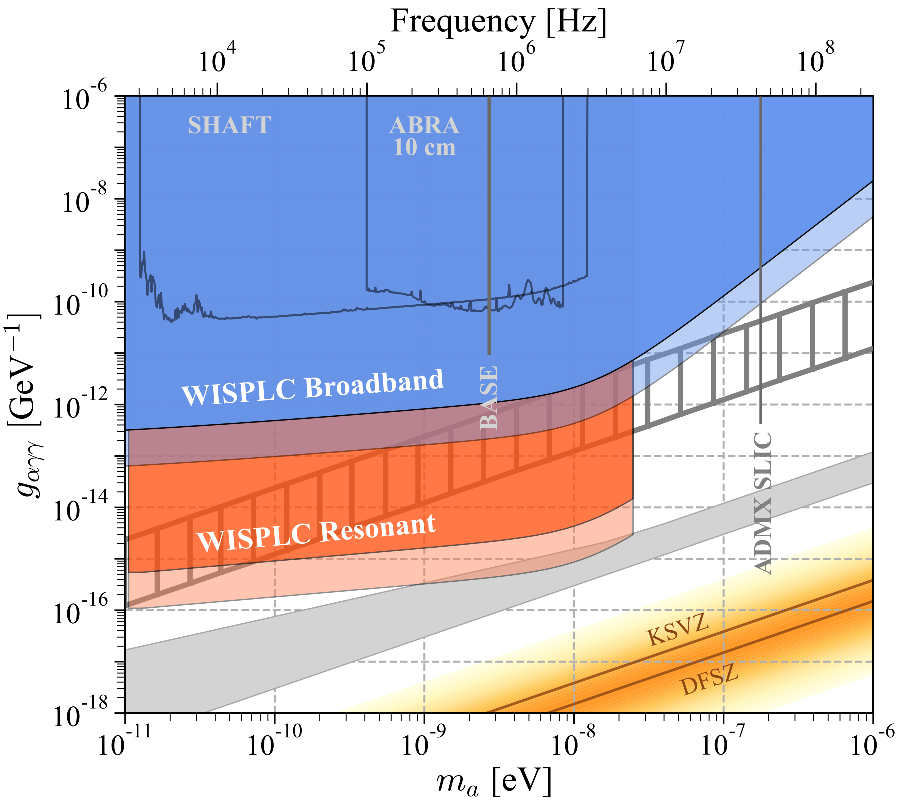

Figure 34: Projected 2σ exclusion limit in the parameter space for broadband, in blue, and resonant, in orange, detection schemes. The light-shaded blue and orange areas represent the sensitivity with an improved read-out. The total measurement time is 100 days for both schemes. In the resonant scheme, a frequency scan 1 minute of integration time is planned with bandwidth ω/Q, which covers the mass range $10^{-12} - 10^{-8}$eV. The favoured parameter space of the trapped misalignment axion model [186] and the photophilic axion model [185] are respectively displayed in light-shaded grey area and dark grey lines. The figure is presented as in [1].

9 OUTLOOK

In this thesis, I described how plasma instabilities are manifested in the laboratory and in astrophysical pair beams. In addition, we have seen how the energetic broadening of pair beams due to diffusion in momentum space affect their evolution in the laboratory. For the first time, the beam evolution is described in a compact advective-diffusive form of the Fokker-Planck equation for probability distribution functions describing the pair beams, such as a 2D Gaussian distribution.

For astrophysical pair beams, it can be concluded that energetic broadening of the spectrum is not observable in terms of time delay observations. In addition, for canonical predictions of electrostatic unstable modes, the spectra of astrophysical pair beams is not significantly modified. Only in specific unstable modes with $\propto \gamma$ or larger growth-rate scalings, instabilities could compete with ICS in altering the observed cascade spectra. A realistic laboratory astrophysics experiment could be the ideal testbed for these predictions, since uncertainties such as strong magnetic deflections [32] or diffusive effects of weak tangled magnetic field [31] can quench the instabilities in the astrophysical scenario. It can also be useful in studying the effect of inhomogeneities in the plasma in the development and sustenance of the instabilities in addition to nonlinear effects.

Next, I looked into how the energy losses associated with plasma instabilities can drain energy from the astrophysical pair beams into the IGM, altering the thermal history at late times. In addition to the explicit calculations of temperature-density relations for such blazar beam-induced heating, temperature evolution with redshifts for various overdensities are derived. The important insight from this computation is that blazar heating is most pronounced at underdense regions, where presence of hot gas, as observed by Ly-α observations, cannot be explained by a late HeII reionization. Computation of Jeans and filtering scale through the elevated entropy floor shows that for a homogeneous volumetric heating assumption, dwarf galaxies cannot form below a certain scale at late times, and this is then directly compared to the predictions of ultralight axions.

In the final part of the thesis, I outlined the design and sensitivity of a haloscope built to detect axion-like particles through amplifying the magnetic field from axion-induced current using an LC-circuit, WISPLC [1]. The detector can operate in resonant mode in addition to a broadband mode, which gives it significant sensitivity gain of nearly three orders of magnitude over the broadband scheme. The sensitivity at 2σ for an axion mass range of $10^{-11} - 10^{-6}$eV reaches $g_{a\gamma\gamma} \approx 10^{-15}$GeV^{-1}.

[1] Zhongyue Zhang, Dieter Horns, Oindrila Ghosh, et al. "Search for dark matter with an L C circuit." In: *Physical Review D* 106.2 (2022), p. 023003.

[2] Andrii Neronov and Ievgen Vovk. "Evidence for strong extragalactic magnetic fields from Fermi observations of TeV blazars." In: *Science* 328.5974 (2010), pp. 73–75.

[3] M Ackermann, M Ajello, L Baldini, J Ballet, G Barbiellini, D Bastieri, R Bellazzini, E Bissaldi, RD Blandford, ED Bloom, et al. "The search for spatial extension in high-latitude sources detected by the Fermi Large Area Telescope." In: *The Astrophysical Journal Supplement Series* 237.2 (2018), p. 32.

[4] Kiyotomo Ichiki, Susumu Inoue, and Keitaro Takahashi. "Probing the nature of the weakest intergalactic magnetic fields with the high-energy emission of gamma-ray bursts." In: *The Astrophysical Journal* 682.1 (2008), p. 127.

[5] Robert J Gould and Gérard P Schréder. "Opacity of the universe to high-energy photons." In: *Physical Review* 155.5 (1967), p. 1408.

[6] MH Salamon and FW Stecker. "Absorption of high-energy gamma rays by interactions with extragalactic starlight photons at high redshifts and the high-energy gamma-ray background." In: *The Astrophysical Journal* 493.2 (1998), p. 547.

[7] A Neronov and DV Semikoz. "Sensitivity of γ-ray telescopes for detection of magnetic fields in the intergalactic medium." In: *Physical Review D* 80.12 (2009), p. 123012.

[8] Takuro Narumoto and Tomonori Totani. "Gamma-ray luminosity function of blazars and the cosmic gamma-ray background: evidence for the luminosity-dependent density evolution." In: *The Astrophysical Journal* 643.1 (2006), p. 81.

[9] Tonia M Venters. "Contribution to the extragalactic gamma-ray background from the cascades of very high energy gamma rays from blazars." In: *The Astrophysical Journal* 710.2 (2010), p. 1530.

[10] Ryuichi Takahashi, Masanori Sato, Takahiro Nishimichi, Atsushi Taruya, and Masamune Oguri. "Revising the halofit model for the nonlinear matter power spectrum." In: *The Astrophysical Journal* 761.2 (2012), p. 152.

[11] A. Taylor, Ievgen Vovk, and A. Neronov. "Extragalactic magnetic fields constraints from simultaneous GeV-TeV observations of blazars." In: *Astronomy Astrophysics - ASTRON ASTROPHYS* 529 (May 2011). DOI: 10.1051/0004-6361/201116441.

[12] Charles D Dermer, Massimo Cavadini, Soebur Razzaque, Justin D Finke, James Chiang, and Benoit Lott. "Time delay of cascade radiation for TeV blazars and the measurement of the intergalactic magnetic field." In: *The Astrophysical journal letters* 733.2 (2011), p. L21.

[13] Sangjin Lee, Angela V Olinto, and Guenter Sigl. "Extragalactic magnetic field and the highest energy cosmic rays." In: *The Astrophysical Journal* 455.1 (1995), p. L21.

[14] Antoine Bret, Laurent Gremillet, and Mark Eric Dieckmann. "Multidimensional electron beam-plasma instabilities in the relativistic regime." In: *Physics of Plasmas* 17.12 (2010), p. 120501.

[15] Avery E Broderick, Philip Chang, and Christoph Pfrommer. "The cosmological impact of luminous TeV blazars. I. Implications of plasma instabilities for the intergalactic magnetic field and extragalactic gamma-ray background." In: *The Astrophysical Journal* 752.1 (2012), p. 22.

[16] Rudolf A Treumann and Wolfgang Baumjohann. *Advanced space plasma physics*. Vol. 30. Imperial College Press London, 1997.

[17] Ya B Fainberg, VD Shapiro, and VI Shevchenko. "Nonlinear Waves in Uncompensated Electron Beams." In: *SOVIET PHYSICS JETP* 34.1 (1972).

[18] A Bret, M-C Firpo, and C Deutsch. "Electromagnetic instabilities for relativistic beam-plasma interaction in whole k space: Nonrelativistic beam and plasma temperature effects." In: *Physical Review E* 72.1 (2005), p. 016403.

[19] Antoine Bret, Laurent Gremillet, and Didier Benisti. "Exact relativistic kinetic theory of the full unstable spectrum of an electron-beam–plasma system with Maxwell-Jüttner distribution functions." In: *Physical Review E* 81.3 (2010), p. 036402.

[20] BN Brejzman and VV Mirnov. "About the instability connected with the anisotropy of the distribution function of ultrarelativistic electrons in the earth's radiation belts." In: *Geomagn. Aehron* 10 (1970), pp. 34–37.

[21] Francesco Miniati and Andrii Elyiv. "Relaxation of blazar-induced pair beams in cosmic voids." In: *The Astrophysical Journal* 770.1 (2013), p. 54.

[22] BN Brejzman and DD Ryutov. "Powerful relativistic electron beams in a plasma and in a vacuum (theory)." In: *Nuclear Fusion* 14.6 (1974), p. 873.

[23] AA Galeev, RZ Sagdeev, Yu S Sigov, VD Shapiro, and VI Shevchenko. "Nonlinear theory of the modulation instability of plasma waves." In: *Sov. J. Plasma Phys.(Engl. Transl.);(United States)* 1.1 (1975).

[24] R Schlickeiser, R Vainio, M Böttcher, I Lerche, M Pohl, and C Schuster. "Conversion of relativistic pair energy into radiation in the jets of active galactic nuclei." In: *Astronomy & Astrophysics* 393.1 (2002), pp. 69–87.

[25] Reinhard Schlickeiser, Steffen Krakau, and Markus Supsar. "Plasma effects on fast pair beams. II. Reactive versus kinetic instability of parallel electrostatic waves." In: *The Astrophysical Journal* 777.1 (2013), p. 49.

[26] Erich S Weibel. "Spontaneously growing transverse waves in a plasma due to an anisotropic velocity distribution." In: *Physical Review Letters* 2.3 (1959), p. 83.

[27] Mikhail V Medvedev and Abraham Loeb. "Generation of magnetic fields in the relativistic shock of gamma-ray burst sources." In: *The Astrophysical Journal* 526.2 (1999), p. 697.

[28] Burton D Fried. *On the mechanism for instability of transverse plasma waves*. Tech. rep. TRW SPACE TECHNOLOGY LABS LOS ANGELES CALIF, 1959.

[29] SA Kaplan and VN Tsytovich. "Radio Emission from Beams of Fast Particles under Cosmic Conditions." In: *Soviet Astronomy* 11 (1968), p. 956.

[30] G Qin and A Shalchi. "Pitch-angle diffusion coefficients of charged particles from computer simulations." In: *The Astrophysical Journal* 707.1 (2009), p. 61.

[31] Mahmoud Alawashra and Martin Pohl. "Suppression of the TeV Pair-beam–Plasma Instability by a Tangled Weak Intergalactic Magnetic Field." In: *The Astrophysical Journal* 929.1 (2022), p. 67.

[32] Lorenzo Sironi and Dimitrios Giannios. "Relativistic pair beams from tev blazars: a source of reprocessed gev emission rather than intergalactic heating." In: *The Astrophysical Journal* 787.1 (2014), p. 49.

[33] Marvin Beck, Oindrila Ghosh, Florian Grüner, Martin Pohl, Carl B Schroeder, Günter Sigl, Ryan D Stark, and Benno Zeitler. "Evolution of Relativistic Pair Beams: Implications for Laboratory and TeV Astrophysics." In: *arXiv preprint arXiv:2306.16839* (2023).

[34] FA Aharonian. "TeV blazars and cosmic infrared background radiation." In: *Arxiv preprint astro-ph/0112314* (2001).

[35] Avery E. Broderick, Christoph Pfrommer, Ewald Puchwein, and Philip Chang. "IMPLICATIONS OF PLASMA BEAM INSTABILITIES FOR THE STATISTICS OF THE FERMI HARD GAMMA-RAY BLAZARS AND THE ORIGIN OF THE EXTRAGALACTIC GAMMA-RAY BACKGROUND." In: *The Astrophysical Journal* 790.2 (2014).

[36] Markus Supsar and Reinhard Schlickeiser. "Plasma effects on fast pair beams. III. Oblique electrostatic growth rates for perpendicular Maxwellian pair beams." In: *The Astrophysical Journal* 783.2 (2014), p. 96.

[37] Kempf, A., Kilian, P., and Spanier, F. "Energy loss in intergalactic pair beams: Particle-in-cell simulation." In: *A&A* 585 (2016), A132. DOI: 10.1051/0004-6361/201527521. URL: https://doi.org/10.1051/0004-6361/201527521.

[38] Iman Rafighi, Sergei Vafin, M Pohl, and J Niemiec. "Plasma effects on relativistic pair beams from TeV blazars: PIC simulations and analytical predictions." In: *Astronomy & Astrophysics* 607 (2017), A112.

[39] Sergei Vafin, I Rafighi, M Pohl, and Jacek Niemiec. "The electrostatic instability for realistic pair distributions in blazar/EBL cascades." In: *The Astrophysical Journal* 857.1 (2018), p. 43.

[40] S. Vafin, P. J. Deka, M. Pohl, and A. Bohdan. "Revisit of Nonlinear Landau Damping for Electrostatic Instability Driven by Blazar-induced Pair Beams." In: *The Astrophysical Journal* 873.1 (2019), p. 10.

[41] Rafael Alves Batista, Andrey Saveliev, and Elisabete de Gouveia Dal Pino. "The Impact of Plasma Instabilities on the Spectra of TeV Blazars." In: *Monthly Notices of the Royal Astronomical Society* 489 (Sept. 2019).

[42] Mohamad Shalaby, Avery E. Broderick, Philip Chang, Christoph Pfrommer, Ewald Puchwein, and Astrid Lamberts. "The growth of the longitudinal beam–plasma instability in the presence of an inhomogeneous background." In: *Journal of Plasma Physics* 86.2 (2020), p. 535860201.

[43] Martin Lemoine and Guy Pelletier. "On electromagnetic instabilities at ultra-relativistic shock waves." In: *Monthly Notices of the Royal Astronomical Society* 402.1 (2010), pp. 321–334.

[44] Avery E Broderick, Paul Tiede, Mohamad Shalaby, Christoph Pfrommer, Ewald Puchwein, Philip Chang, and Astrid Lamberts. "BOW TIES IN THE SKY. I. THE ANGULAR STRUCTURE OF INVERSE COMPTON GAMMA-RAY HALOS IN THE FERMI SKY." In: *The Astrophysical Journal* 832.2 (2016), p. 109.

[45] Carlos Blanco, Oindrila Ghosh, Sunniva Jacobsen, and Tim Linden. "Where are the Cascades from Blazar Jets? An Emerging Tension in the

\

gamma $-raysky$." In: *arXiv preprint arXiv:2303.01524* (2023).

[46] Roy Perry and Yuri Lyubarsky. "The role of resonant plasma instabilities in the evolution of blazar-induced pair beams." In: *Monthly Notices of the Royal Astronomical Society* 503.2 (2021), pp. 2215–2228.

[47] Mahmoud Alawashra and Martin Pohl. "Suppression of the TeV Pair-beam-Plasma Instability by a Tangled Weak Intergalactic Magnetic Field." In: 929.1, 67 (Apr. 2022), p. 67. DOI: 10.3847/1538-4357/ac5a4b. arXiv: 2203.01022 [astro-ph.HE].

[48] Philip Chang, Avery E Broderick, and Christoph Pfrommer. "The cosmological impact of luminous TeV blazars. II. Rewriting the thermal history of the intergalactic medium." In: *The Astrophysical Journal* 752.1 (2012), p. 23.

[49] C. Pfrommer, A. E. Brodericki, V. Springel, P. Chang, and E. Puchwein. "The physics and cosmology of TeV blazars in a nutshell." In: *48th Rencontres de Moriond on Very High Energy Phenomena in the Universe*. 2013, pp. 351–358.

[50] A Bret, L Gremillet, D Bénisti, and E Lefebvre. "Exact relativistic kinetic theory of an electron-beam–plasma system: Hierarchy of the competing modes in the system-parameter space." In: *Physical review letters* 100.20 (2008), p. 205008.

[51] A. Bret, L. Gremillet, and M. E. Dieckmann. "Multidimensional electron beam-plasma instabilities in the relativistic regime." In: *Physics of Plasmas* 17.12 (2010), p. 120501. DOI: 10.1063/1.3514586. eprint: https://doi.org/10.1063/1.3514586. URL: https://doi.org/10.1063/1.3514586.

[52] Robert Buschauer and Gregory Benford. "Temperature stabilization of instabilities in force-free magnetospheres." In: *Monthly Notices of the Royal Astronomical Society* 179.2 (1977), pp. 99–103.

[53] BN Breizman and DD Ryutov. "Quasilinear relaxation of an ultrarelativistic electron beam in a plasma." In: *SOVIET PHYSICS JETP* 33.1 (1971).

[54] Gianluca Sarri et al. "Generation of neutral and high-density electron–positron pair plasmas in the laboratory." In: *Nature communications* 6 (Apr. 2015), p. 6747. DOI: 10.1038/ncomms7747.

[55] Jonathan Warwick et al. "Experimental Observation of a Current-Driven Instability in a Neutral Electron-Positron Beam." In: *Physical Review Letters* 119 (May 2017). DOI: 10.1103/PhysRevLett.119.185002.

[56] Tanja M Kneiske, T Bretz, K Mannheim, and DH Hartmann. "Implications of cosmological gamma-ray absorption-II. Modification of gamma-ray spectra." In: *Astronomy & Astrophysics* 413.3 (2004), pp. 807–815.

[57] Tanja M Kneiske, Karl Mannheim, and Dieter H Hartmann. "Implications of cosmological gamma-ray absorption-I. Evolution of the metagalactic radiation field." In: *Astronomy & Astrophysics* 386.1 (2002), pp. 1–11.

[58] F W Stecker, O C De Jager, and MH Salamon. "TeV gamma rays from 3C 279-A possible probe of origin and intergalactic infrared radiation fields." In: *The Astrophysical Journal* 390 (1992), pp. L49–L52.

[59] R Plaga. "Detecting intergalactic magnetic fields using time delays in pulses of γ-rays." In: *Nature* 374.6521 (1995), pp. 430–432.

[60] Keitaro Takahashi, Kiyotomo Ichiki, Hiroshi Ohno, and Hidekazu Hanayama. "Magnetic field generation from cosmological perturbations." In: *Physical review letters* 95.12 (2005), p. 121301.

[61] Kohta Murase, Katsuaki Asano, and Shigehiro Nagataki. "Effects of cosmic infrared background on high energy delayed gamma-rays from gamma-ray bursts." In: *arXiv preprint astro-ph/0703759* (2007).

[62] George R Blumenthal and Robert J Gould. "Bremsstrahlung, synchrotron radiation, and compton scattering of high-energy electrons traversing dilute gases." In: *Reviews of Modern Physics* 42.2 (1970), p. 237.

[63] Soebur Razzaque, Peter Mészáros, and Bing Zhang. "GeV and higher energy photon interactions in gamma-ray burst fireballs and surroundings." In: *The Astrophysical Journal* 613.2 (2004), p. 1072.

[64] CHARLES Alcock and STEPHEN Hatchett. "The effects of small-angle scattering on a pulse of radiation with an application of X-ray bursts and interstellar dust." In: *The Astrophysical Journal* 222 (1978), pp. 456–470.

[65] Peter AR Ade, N Aghanim, M Arnaud, Mark Ashdown, J Aumont, C Baccigalupi, AJ Banday, RB Barreiro, JG Bartlett, N Bartolo, et al. "Planck 2015 results-xiii. cosmological parameters." In: *Astronomy & Astrophysics* 594 (2016), A13.

[66] Gianfranco Bertone, Dan Hooper, and Joseph Silk. "Particle dark matter: Evidence, candidates and constraints." In: *Physics reports* 405.5-6 (2005), pp. 279–390.

[67] Marc Oncins. "Constraints on PBH as dark matter from observations: a review." In: *arXiv preprint arXiv:2205.14722* (2022).

[68] Paul Bode, Jeremiah P Ostriker, and Neil Turok. "Halo formation in warm dark matter models." In: *The Astrophysical Journal* 556.1 (2001), p. 93.

[69] Matteo Viel, Julien Lesgourgues, Martin G Haehnelt, Sabino Matarrese, and Antonio Riotto. "Constraining warm dark matter candidates including sterile neutrinos and light gravitinos with WMAP and the Lyman-α forest." In: *Physical Review D* 71.6 (2005), p. 063534.

[70] Pierre Colin, Vladimir Avila-Reese, and Octavio Valenzuela. "Substructure and halo density profiles in a Warm Dark Matter scenario." In: *Arxiv preprint astro-ph/0009317* (2000).

[71] Scott Tremaine and James E Gunn. "Dynamical role of light neutral leptons in cosmology." In: *Physical Review Letters* 42.6 (1979), p. 407.

[72] Roberto D Peccei and Helen R Quinn. "CP Conservation in the Presence of Instantons." In: *Physical Review Letters* 38.ITP-568-STANFORD (1977), pp. 1440–1443.

[73] Steven Weinberg. "A new light boson?" In: *Physical Review Letters* 40.4 (1978), p. 223.

[74] Frank Wilczek. "Problem of Strong P and T Invariance in the Presence of Instantons." In: *Physical Review Letters* 40.5 (1978), p. 279.

[75] Roberto D Peccei and Helen R Quinn. "CP Conservation in the Presence of Instantons." In: *Phys. Rev. Lett* 38.1440-1443 (1977), p. 328.

[76] Steven Weinberg. "A new light boson?" In: *Physical Review Letters* 40.4 (1978), p. 223.

[77] Frank Wilczek. "Problem of Strong P and T Invariance in the Presence of Instantons." In: *Physical Review Letters* 40.5 (1978), p. 279.

[78] Jihn E Kim. "Weak-interaction singlet and strong CP invariance." In: *Physical Review Letters* 43.2 (1979), p. 103.

[79] Mikhail A Shifman, AI Vainshtein, and Valentin I Zakharov. "Can confinement ensure natural CP invariance of strong interactions?" In: *Nuclear Physics B* 166.3 (1980), pp. 493–506.

[80] Michael Dine, Willy Fischler, and Mark Srednicki. "A simple solution to the strong CP problem with a harmless axion." In: *Physics Letters B* 104.3 (1981), pp. 199–202.

[81] A. R. Zhitnitsky. "On Possible Suppression of the Axion Hadron Interactions. (In Russian)." In: *Soviet Journal of Nuclear Physics* 31 (1980), p. 260.

[82] Lam Hui, Jeremiah P Ostriker, Scott Tremaine, and Edward Witten. "Ultralight scalars as cosmological dark matter." In: *Physical Review D* 95.4 (2017), p. 043541.

[83] David JE Marsh and Pedro G Ferreira. "Ultralight scalar fields and the growth of structure in the Universe." In: *Physical Review D* 82.10 (2010), p. 103528.

[84] Hsi-Yu Schive, Tzihong Chiueh, and Tom Broadhurst. "Cosmic structure as the quantum interference of a coherent dark wave." In: *Nature Physics* 10.7 (2014), pp. 496–499.

[85] David JE Marsh. "Axions and ALPs: a very short introduction." In: *arXiv preprint arXiv:1712.03018* (2017).

[86] Maria Archidiacono, Steen Hannestad, Alessandro Mirizzi, Georg Raffelt, and Yvonne YY Wong. "Axion hot dark matter bounds after Planck." In: *Journal of Cosmology and Astroparticle Physics* 2013.10 (2013), p. 020.

[87] Eleonora Di Valentino, Stefano Gariazzo, Elena Giusarma, and Olga Mena. "Robustness of cosmological axion mass limits." In: *Physical Review D* 91.12 (2015), p. 123505.

[88] Steen Hannestad, Alessandro Mirizzi, and Georg Raffelt. "A new cosmological mass limit on thermal relic axions." In: *Journal of Cosmology and Astroparticle Physics* 2005.07 (2005), p. 002.

[89] Joseph P Conlon and MC Marsh. "The cosmophenomenology of axionic dark radiation." In: *Journal of High Energy Physics* 2013.10 (2013), pp. 1–25.

[90] Joseph P Conlon and MC David Marsh. "Excess astrophysical photons from a 0.1–1 keV cosmic axion background." In: *Physical review letters* 111.15 (2013), p. 151301.

[91] Joshua A Frieman, Christopher T Hill, Albert Stebbins, and Ioav Waga. "Cosmology with ultralight pseudo Nambu-Goldstone bosons." In: *Physical Review Letters* 75.11 (1995), p. 2077.

[92] Katherine Freese, Joshua A Frieman, and Angela V Olinto. "Natural inflation with pseudo Nambu-Goldstone bosons." In: *Physical Review Letters* 65.26 (1990), p. 3233.

[93] Andrei Khmelnitsky and Valery Rubakov. "Pulsar timing signal from ultralight scalar dark matter." In: *Journal of Cosmology and Astroparticle Physics* 2014.02 (2014), p. 019.

[94] Asimina Arvanitaki, Masha Baryakhtar, and Xinlu Huang. "Discovering the QCD axion with black holes and gravitational waves." In: *Physical Review D* 91.8 (2015), p. 084011.

[95] Asimina Arvanitaki, Masha Baryakhtar, Savas Dimopoulos, Sergei Dubovsky, and Robert Lasenby. "Black hole mergers and the QCD axion at advanced LIGO." In: *Physical Review D* 95.4 (2017), p. 043001.

[96] Richard Brito, Shrobana Ghosh, Enrico Barausse, Emanuele Berti, Vitor Cardoso, Irina Dvorkin, Antoine Klein, and Paolo Pani. "Gravitational wave searches for ultralight bosons with LIGO and LISA." In: *Physical Review D* 96.6 (2017), p. 064050.

[97] Peter W Graham, Igor G Irastorza, Steven K Lamoreaux, Axel Lindner, and Karl A van Bibber. "Experimental searches for the axion and axion-like particles." In: *Annual Review of Nuclear and Particle Science* 65 (2015), pp. 485–514.

[98] Georg G Raffelt. "Astrophysical methods to constrain axions and other novel particle phenomena." In: *Physics reports* 198.1-2 (1990), pp. 1–113.

[99] Georg G Raffelt. "Astrophysical axion bounds." In: *Axions*. Springer, 2008, pp. 51–71.

[100] Oscar Straniero, Adrian Ayala, Maurizio Giannotti, Alessandro Mirizzi, and Inma Dominguez. "Axion-photon coupling: astrophysical constraints." In: *11th Patras Workshop on Axions, WIMPs and WISPs*. PUBDB-2017-00134. Verlag Deutsches Elektronen-Synchrotron. 2015.

[101] Javier Redondo and Andreas Ringwald. "Light shining through walls." In: *Contemporary Physics* 52.3 (2011), pp. 211–236.

[102] Klaus Ehret, Maik Frede, Samvel Ghazaryan, Matthias Hildebrandt, Ernst-Axel Knabbe, Dietmar Kracht, Axel Lindner, Jenny List, Tobias Meier, Niels Meyer, et al. "New ALPS results on hidden-sector lightweights." In: *Physics Letters B* 689.4-5 (2010), pp. 149–155.

[103] Pierluca Carenza, Ramkishor Sharma, MC Marsh, Axel Brandenburg, and Eike Müller. "Magnetohydrodynamics predicts heavy-tailed distributions of axion-photon conversion." In: *arXiv preprint arXiv:2208.04333* (2022).

[104] Joseph P Conlon, Francesca Day, Nicholas Jennings, Sven Krippendorf, and Markus Rummel. "Constraints on axion-like particles from non-observation of spectral modulations for X-ray point sources." In: *Journal of Cosmology and Astroparticle Physics* 2017.07 (2017), p. 005.

[105] Alessandro Mirizzi, Javier Redondo, and Günter Sigl. "Constraining resonant photon-axion conversions in the Early Universe." In: *Journal of Cosmology and Astroparticle Physics* 2009.08 (2009), p. 001.

[106] Hiroyuki Tashiro, Joseph Silk, and David JE Marsh. "Constraints on primordial magnetic fields from CMB distortions in the axiverse." In: *Physical Review D* 88.12 (2013), p. 125024.

[107] John Ellis, Graciela B Gelmini, Jorge L Lopez, Dimitri V Nanopoulos, and Subir Sarkar. "Astrophysical constraints on massive unstable neutral relic particles." In: *Nuclear Physics B* 373.2 (1992), pp. 399–437.

[108] Eduard Masso and Ramon Toldra. "New constraints on a light spinless particle coupled to photons." In: *Physical Review D* 55.12 (1997), p. 7967.

[109] Katharine Kelley and PJ Quinn. "Searching for Axion Dark Matter using Radio Telescopes." In: *arXiv preprint arXiv:1710.10376* (2017).

[110] Pierre Sikivie. "Experimental tests of the" invisible" axion." In: *Physical Review Letters* 51.16 (1983), p. 1415.

[111] Stephen J Asztalos, G Carosi, C Hagmann, D Kinion, K Van Bibber, M Hotz, LJ Rosenberg, G Rybka, J Hoskins, J Hwang, et al. "SQUID-based microwave cavity search for dark-matter axions." In: *Physical review letters* 104.4 (2010), p. 041301.

[112] P Sikivie, N Sullivan, and Dylan B Tanner. "Proposal for Axion Dark Matter Detection Using an L C Circuit." In: *Physical review letters* 112.13 (2014), p. 131301.

[113] B Majorovits et al. "MADMAX: A new road to axion dark matter detection." In: *Journal of Physics: Conference Series*. Vol. 1342. 1. IOP Publishing. 2020, p. 012098.

[114] Allen Caldwell, Gia Dvali, Béla Majorovits, Alexander Millar, Georg Raffelt, Javier Redondo, Olaf Reimann, Frank Simon, Frank Steffen, MADMAX Working Group, et al. "Dielectric haloscopes: a new way to detect axion dark matter." In: *Physical review letters* 118.9 (2017), p. 091801.

[115] Dmitry Budker, Peter W Graham, Micah Ledbetter, Surjeet Rajendran, and Alexander O Sushkov. "Proposal for a cosmic axion spin precession experiment (CASPEr)." In: *Physical Review X* 4.2 (2014), p. 021030.

[116] Alexander V. Gramolin, Deniz Aybas, Dorian Johnson, Janos Adam, and Alexander O. Sushkov. "Search for axion-like dark matter with ferromagnets." In: *Nature Physics* 17.1 (2021), pp. 79–84. ISSN: 1745-2481. DOI: 10.1038/s41567-020-1006-6. URL: https://doi.org/10.1038/s41567-020-1006-6.

[117] Yonatan Kahn, Benjamin R. Safdi, and Jesse Thaler. "Broadband and Resonant Approaches to Axion Dark Matter Detection." In: *Phys. Rev. Lett.* 117.14 (2016), p. 141801. DOI: 10.1103/PhysRevLett.117.141801. arXiv: 1602.01086 [hep-ph].

[118] M Arik, A Ljubičić, I Shilon, H Bräuninger, R Hartmann, Anastasios Liolios, J Galán, E Da Riva, K Königsmann, S Gninenko, et al. "Search for Solar Axions by the CERN Axion Solar Telescope with He 3 Buffer Gas." In: *Physical Review Letters* 112.IKEEXREF-274521 (2014).

[119] JK Vogel, FT Avignone, G Cantatore, JM Carmona, S Caspi, SA Cetin, FE Christensen, A Dael, T Dafni, M Davenport, et al. "IAXO-the international axion observatory." In: *arXiv preprint arXiv:1302.3273* (2013).

[120] K Desch, B Döbrich, I Irastorza, J Jaeckel, A Lindner, B Majorovits, and A Ringwald. *A European Strategy Towards Finding Axions and Other WISPs*. 2018.

[121] Renée Hlozek, Daniel Grin, David JE Marsh, and Pedro G Ferreira. "A search for ultralight axions using precision cosmological data." In: *Physical Review D* 91.10 (2015), p. 103512.

[122] Lam Hui and Nickolay Y Gnedin. "Equation of state of the photoionized intergalactic medium." In: *Monthly Notices of the Royal Astronomical Society* 292.1 (1997), pp. 27–42.

[123] Aous A Abdo, Markus Ackermann, Marco Ajello, WB Atwood, Magnus Axelsson, Luca Baldini, Jean Ballet, Guido Barbiellini, Denis Bastieri, Milan Battelino, et al. "Measurement of the cosmic ray e++ e- spectrum from 20 GeV to 1 TeV with the Fermi Large Area Telescope." In: *Physical Review Letters* 102.18 (2009), p. 181101.

[124] Matthew McQuinn. "The evolution of the intergalactic medium." In: *Annual Review of Astronomy and Astrophysics* 54 (2016), pp. 313–362.

[125] Francesco Haardt and Piero Madau. "Radiative transfer in a clumpy universe. IV. New synthesis models of the cosmic UV/x-ray background." In: *The Astrophysical Journal* 746.2 (2012), p. 125.

[126] Matthew McQuinn and Phoebe R Upton Sanderbeck. "On the intergalactic temperature–density relation." In: *Monthly Notices of the Royal Astronomical Society* 456.1 (2016), pp. 47–54.

[127] T Padmanabhan and Kandaswamy Subramanian. "Aspects of Zeldovich approximation." In: (1993).

[128] Philip F Hopkins, Gordon T Richards, and Lars Hernquist. "An observational determination of the bolometric quasar luminosity function." In: *The Astrophysical Journal* 654.2 (2007), p. 731.

[129] Ewald Puchwein, Christoph Pfrommer, Volker Springel, Avery E Broderick, and Philip Chang. "The Lyman α forest in a blazar-heated Universe." In: *Monthly Notices of the Royal Astronomical Society* 423.1 (2012), pp. 149–164.

[130] Volker Springel, Rüdiger Pakmor, Oliver Zier, and Martin Reinecke. "Simulating cosmic structure formation with the GADGET-4 code." In: *Monthly Notices of the Royal Astronomical Society* 506.2 (2021), pp. 2871–2949.

[131] C Pfrommer, AE Broderick, P Chang, E Puchwein, and V Springel. "The physics and cosmology of TeV blazars in a nutshell." In: *arXiv preprint arXiv:1308.6284* (2013).

[132] Christoph Pfrommer, Philip Chang, and Avery E Broderick. "The cosmological impact of luminous TeV blazars. III. Implications for galaxy clusters and the formation of dwarf galaxies." In: *The Astrophysical Journal* 752.1 (2012), p. 24.

[133] Matteo Viel, James S Bolton, and Martin G Haehnelt. "Cosmological and astrophysical constraints from the Lyman α forest flux probability distribution function." In: *Monthly Notices of the Royal Astronomical Society: Letters* 399.1 (2009), pp. L39–L43.

[134] Michael Walther, Jose Oñorbe, Joseph F Hennawi, and Zarija Lukić. "New constraints on IGM thermal evolution from the Lyα forest power spectrum." In: *The Astrophysical Journal* 872.1 (2019), p. 13.

[135] Hector Hiss, Michael Walther, Joseph F Hennawi, José Oñorbe, John M O'Meara, Alberto Rorai, and Zarija Lukić. "A new measurement of the temperature–density relation of the IGM from Voigt profile fitting." In: *The Astrophysical Journal* 865.1 (2018), p. 42.

[136] SC Madden, A Rémy-Ruyer, M Galametz, D Cormier, V Lebouteiller, F Galliano, S Hony, GJ Bendo, MWL Smith, M Pohlen, et al. "An overview of the dwarf galaxy survey." In: *Publications of the Astronomical Society of the Pacific* 125.928 (2013), p. 600.

[137] J Sánchez Almeida, Bruce G Elmegreen, C Muñoz-Tuñón, DM Elmegreen, E Pérez-Montero, R Amorín, Y Ascasibar, P Papaderos, JM Vílchez, et al. "Localized starbursts in dwarf galaxies produced by the impact of low-metallicity cosmic gas clouds." In: *The Astrophysical Journal Letters* 810.2 (2015), p. L15.

[138] Kristen BW McQuinn, Danielle A Berg, Evan D Skillman, Elizabeth AK Adams, John M Cannon, Andrew E Dolphin, John J Salzer, Riccardo Giovanelli, Martha P Haynes, Alec S Hirschauer, et al. "The Leoncino Dwarf Galaxy: Exploring the Low-metallicity End of the Luminosity–Metallicity and Mass–Metallicity Relations." In: *The Astrophysical Journal* 891.2 (2020), p. 181.

[139] Wayne Hu, Rennan Barkana, and Andrei Gruzinov. "Fuzzy cold dark matter: the wave properties of ultralight particles." In: *Physical Review Letters* 85.6 (2000), p. 1158.

[140] David J Sand, Tommaso Treu, Graham P Smith, and Richard S Ellis. "The dark matter distribution in the central regions of galaxy clusters: implications for cold dark matter." In: *The Astrophysical Journal* 604.1 (2004), p. 88.

[141] Andrew B Newman, Tommaso Treu, Richard S Ellis, David J Sand, Johan Richard, Philip J Marshall, Peter Capak, and Satoshi Miyazaki. "The distribution of dark matter over three decades in radius in the lensing cluster abell 611." In: *The Astrophysical Journal* 706.2 (2009), p. 1078.

[142] George R Blumenthal, SM Faber, Ricardo Flores, and Joel R Primack. "Contraction of dark matter galactic halos due to baryonic infall." In: *The Astrophysical Journal* 301 (1986), pp. 27–34.

[143] Fabio Governato, C Brook, L Mayer, A Brooks, G Rhee, J Wadsley, P Jonsson, B Willman, G Stinson, T Quinn, et al. "Bulgeless dwarf galaxies and dark matter cores from supernova-driven outflows." In: *nature* 463.7278 (2010), pp. 203–206.

[144] F Governato, A Zolotov, A Pontzen, C Christensen, Se-Heon Oh, AM Brooks, T Quinn, S Shen, and J Wadsley. "Cuspy no more: how outflows affect the central dark matter and baryon distribution in Λ cold dark matter galaxies." In: *Monthly Notices of the Royal Astronomical Society* 422.2 (2012), pp. 1231–1240.

[145] Matteo Viel, George D Becker, James S Bolton, and Martin G Haehnelt. "Warm dark matter as a solution to the small scale crisis: New constraints from high redshift Lyman-α forest data." In: *Physical Review D* 88.4 (2013), p. 043502.

[146] Aurel Schneider, Donnino Anderhalden, Andrea V Macciò, and Juerg Diemand. "Warm dark matter does not do better than cold dark matter in solving small-scale inconsistencies." In: *Monthly Notices of the Royal Astronomical Society: Letters* 441.1 (2014), pp. L6–L10.

[147] Andrea V Maccio, Sinziana Paduroiu, Donnino Anderhalden, Aurel Schneider, and Ben Moore. "Cores in warm dark matter haloes: a Catch 22 problem." In: *Monthly Notices of the Royal Astronomical Society* 424.2 (2012), pp. 1105–1112.

[148] Anatoly Klypin, Andrey V Kravtsov, Octavio Valenzuela, and Francisco Prada. "Where are the missing galactic satellites?" In: *The Astrophysical Journal* 522.1 (1999), p. 82.

[149] Ben Moore, Sebastiano Ghigna, Fabio Governato, George Lake, Thomas Quinn, Joachim Stadel, and Paolo Tozzi. "Dark matter substructure within galactic halos." In: *The Astrophysical Journal* 524.1 (1999), p. L19.

[150] G Kauffmann, Simon DM White, and B Guiderdoni. "The formation and evolution of galaxies within merging dark matter haloes." In: *Monthly Notices of the Royal Astronomical Society* 264.1 (1993), pp. 201–218.

[151] Xiang-Xiang Xue, Hans-Walter Rix, Brian Yanny, Timothy C Beers, Eric F Bell, Gang Zhao, James S Bullock, Kathryn V Johnston, Heather Morrison, Constance Rockosi, et al. "Quantifying Kinematic Substructure in the Milky Way's Stellar Halo." In: *The Astrophysical Journal* 738.1 (2011), p. 79.

[152] Michael Boylan-Kolchin, James S Bullock, and Manoj Kaplinghat. "Too big to fail? The puzzling darkness of massive Milky Way subhaloes." In: *Monthly Notices of the Royal Astronomical Society: Letters* 415.1 (2011), pp. L40–L44.

[153] Shea Garrison-Kimmel, Michael Boylan-Kolchin, James S Bullock, and Evan N Kirby. "Too big to fail in the local group." In: *Monthly Notices of the Royal Astronomical Society* 444.1 (2014), pp. 222–236.

[154] Emmanouil Papastergis, Riccardo Giovanelli, Martha P Haynes, and Francesco Shankar. "Is there a "too big to fail" problem in the field?" In: *Astronomy & Astrophysics* 574 (2015), A113.

[155] PJE Peebles. "The void phenomenon." In: *The Astrophysical Journal* 557.2 (2001), p. 495.

[156] Thanu Padmanabhan. *Structure formation in the universe*. Cambridge university press, 1993.

[157] Phillip James Edwin Peebles. *The large-scale structure of the universe*. Vol. 98. Princeton university press, 2020.

[158] James Binney and Scott Tremaine. *Galactic dynamics*. Vol. 13. Princeton university press, 2011.

[159] Nickolay Y Gnedin and Lam Hui. "Probing the Universe with the Lyman-alpha Forest: I. Hydrodynamics of the Low Density IGM." In: *arXiv preprint astro-ph/9706219* (1997).

[160] Nickolay Y Gnedin. "Cosmological reionization by stellar sources." In: *The Astrophysical Journal* 535.2 (2000), p. 530.

[161] Nickolay Y Gnedin. "Effect of reionization on structure formation in the universe." In: *The Astrophysical Journal* 542.2 (2000), p. 535.

[162] Rennan Barkana and Abraham Loeb. "The physics and early history of the intergalactic medium." In: *Reports on Progress in Physics* 70.4 (2007), p. 627.

[163] Andrew Pontzen and Fabio Governato. "Cold dark matter heats up." In: *Nature* 506.7487 (2014), pp. 171–178.

[164] Sergei Bashinsky and Edmund Bertschinger. "Dynamics of cosmological perturbations in position space." In: *Physical Review D* 65.12 (2002), p. 123008.

[165] Lam Hui and Zoltan Haiman. "The thermal memory of reionization history." In: *The Astrophysical Journal* 596.1 (2003), p. 9.

[166] Jai-chan Hwang and Hyerim Noh. "Axion as a cold dark matter candidate." In: *Physics Letters B* 680.1 (2009), pp. 1–3.

[167] Keir K Rogers and Hiranya V Peiris. "Strong bound on canonical ultralight axion dark matter from the lyman-alpha forest." In: *Physical Review Letters* 126.7 (2021), p. 071302.

[168] Jordan Flitter and Ely D Kovetz. "Closing the window on fuzzy dark matter with the 21-cm signal." In: *Physical Review D* 106.6 (2022), p. 063504.

[169] Bruce Partridge and PJE Peebles. "Are young galaxies visible?" In: (1967).

[170] Masami Ouchi, Yoshiaki Ono, and Takatoshi Shibuya. "Observations of the Lyman-

$\backslash$

alpha Universe." In: *arXiv preprint arXiv:2012.07960* (2020).

[171] Hu Zhan, Romeel Davé, Daniel Eisenstein, and Neal Katz. "Lyα flux power spectrum and its covariance." In: *Monthly Notices of the Royal Astronomical Society* 363.4 (2005), pp. 1145–1154.

[172] Emanuele Sobacchi and Andrei Mesinger. "How does radiative feedback from an ultraviolet background impact reionization?" In: *Monthly Notices of the Royal Astronomical Society* 432.4 (2013), pp. 3340–3348.

[173] Gwen C Rudie, Charles C Steidel, Alice E Shapley, and Max Pettini. "The Column Density Distribution and Continuum Opacity of the Intergalactic and Circumgalactic Medium at Redshift< z>= 2.4." In: *The Astrophysical Journal* 769.2 (2013), p. 146.

[174] JS Bolton, Matteo Viel, T-S Kim, MG Haehnelt, and RF Carswell. "Possible evidence for an inverted temperature–density relation in the intergalactic medium from the flux distribution of the Lyα forest." In: *Monthly Notices of the Royal Astronomical Society* 386.2 (2008), pp. 1131–1144.

[175] Elisa Boera, Michael T Murphy, George D Becker, and James S Bolton. "The thermal history of the intergalactic medium down to redshift z= 1.5: a new curvature measurement." In: *Monthly Notices of the Royal Astronomical Society* 441.3 (2014), pp. 1916–1933.

[176] Astrid Lamberts, Ewald Puchwein, Christoph Pfrommer, Philip Chang, Mohamad Shalaby, Avery Broderick, Paul Tiede, and Gwen Rudie. "Constraining blazar heating with the 2 z 3 Lyman-α forest." In: *Monthly Notices of the Royal Astronomical Society* 512.2 (2022), pp. 3045–3059.

[177] Astrid Lamberts, Philip Chang, Christoph Pfrommer, Ewald Puchwein, Avery E Broderick, and Mohamad Shalaby. "Patchy Blazar Heating: Diversifying the Thermal History of the Intergalactic Medium." In: *The Astrophysical Journal* 811.1 (2015), p. 19.

[178] Asantha Cooray and Ravi Sheth. "Halo models of large scale structure." In: *Physics reports* 372.1 (2002), pp. 1–129.

[179] Charles C Steidel, Dawn K Erb, Alice E Shapley, Max Pettini, Naveen Reddy, Milan Bogosavljević, Gwen C Rudie, and Olivera Rakic. "The structure and kinematics of the circumgalactic medium from far-ultraviolet spectra of z 2–3 galaxies." In: *The Astrophysical Journal* 717.1 (2010), p. 289.

[180] Oindrila Ghosh and Sankalan Bhattacharyya. "Light Dark Matter in a Blazar-heated Universe." In: *arXiv preprint arXiv:2309.05421* (2023).

[181] Jonathan L Ouellet, Chiara P Salemi, Joshua W Foster, Reyco Henning, Zachary Bogorad, Janet M Conrad, Joseph A Formaggio, Yonatan Kahn, Joe Minervini, Alexey Radovinsky, et al. "Design and implementation of the ABRACADABRA-10 cm axion dark matter search." In: *Physical Review D* 99.5 (2019), p. 052012.

[182] Jonathan L Ouellet, Chiara P Salemi, Joshua W Foster, Reyco Henning, Zachary Bogorad, Janet M Conrad, Joseph A Formaggio, Yonatan Kahn, Joe Minervini, Alexey Radovinsky, et al. "First Results from ABRACADABRA-10 cm: A Search for Sub-μ eV Axion Dark Matter." In: *Physical Review Letters* 122.12 (2019), p. 121802.

[183] Chiara P. Salemi et al. "Search for Low-Mass Axion Dark Matter with ABRACADABRA-10 cm." In: *Phys. Rev. Lett.* 127 (8 2021), p. 081801. DOI: 10.1103/PhysRevLett.127.081801. URL: https://link.aps.org/doi/10.1103/PhysRevLett.127.081801.

[184] Le Hoang Nguyen, Andrei Lobanov, and Dieter Horns. "First results from the WISPDMX radio frequency cavity searches for hidden photon dark matter." In: *Journal of Cosmology and Astroparticle Physics* 2019.10 (2019), 014–014. ISSN: 1475-7516. DOI: 10.1088/1475-7516/2019/10/014. URL: http://dx.doi.org/10.1088/1475-7516/2019/10/014.